NBSIR 86-3061

ELECTROMECHANICAL PROPERTIES OF SUPERCONDUCTORS FOR HIGH-ENERGY PHYSICS APPLICATIONS

J. W. Ekin
L. F. Goodrich
J. Moreland
E. S. Pittman
A. F. Clark

National Bureau of Standards
U.S. Department of Commerce
Boulder, Colorado 80303

December 1986

NBSIR 86-3061

ELECTROMECHANICAL PROPERTIES OF SUPERCONDUCTORS FOR HIGH-ENERGY PHYSICS APPLICATIONS

J. W. Ekin
L. F. Goodrich
J. Moreland
E. S. Pittman
A. F. Clark

Electromagnetic Technology Division
Center for Electronics and Electrical Engineering
National Engineering Laboratory
National Bureau of Standards
Boulder, Colorado 80303

December 1986

Prepared for
Division of High-Energy Physics
U.S. Department of Energy
Washington, DC 20545
(DOE Interagency Agreement #DE-AI05-85ER40240)

U.S. DEPARTMENT OF COMMERCE, Malcolm Baldrige, Secretary

NATIONAL BUREAU OF STANDARDS, Ernest Ambler, Director

CONTENTS

ELECTROMECHANICAL PROPERTIES OF SUPERCONDUCTORS FOR HIGH-ENERGY PHYSICS APPLICATIONS

J. W. Ekin, L. F. Goodrich, J. Moreland, E. S. Pittman, and A. F. Clark

Electromagnetic Technology Division
National Bureau of Standards
Boulder, Colorado 80303

This report covers the first year of a 33-month project to establish a systematic base of experimental data on electromechanical effects in superconducting wire and cables for high-energy-physics magnet applications. The research is focused in four general research areas: electromechanical relationships in NbTi, studies of NbTi strands extracted from cables, sausaging effects in NbTi, and studies of the NbTi energy gap.

Key Words: cables; electromechanical properties; high-energy physics; magnets; NbTi; stress effect; superconductors

I. REPORT SUMMARY

This report covers the first year of a project to establish a systematic base of experimental data on electromechanical effects in superconducting wire and cables for high-energy-physics magnet applications. The overall objective is to identify the main factors affecting critical-current degradation in superconducting materials. These factors arise from mechanical processing during conductor fabrication and Lorentz-force loading during operation in a magnet. A further objective is to develop strategies leading to the most tolerant strain damage limits in these conductors and, therefore, the least overall performance degradation in magnet applications.

The research is focused on three general areas:

1) Electromechanical relationships in NbTi starting strand materials.

2) Studies of NbTi strands extracted from coreless cables (Rutherford-type).

3) Other properties of NbTi superconductors.
   a) Sausaging effects on V-I characteristics of NbTi.
   b) SET junction studies of NbTi energy gap.

Program highlights in each of these areas for the first year include the following:

1) A new apparatus to measure the effect of transverse compressive stress on NbTi conductors has been constructed, modified, and successfully tested. Preliminary results indicate that the critical-current degradation in NbTi from transverse compressive stress is comparable to that from axial tension; also the effect is highly reversible indicating that the major effects will be exhibited only when the conductor is under operational load stresses.

2) An initial series of tests were done on superconductor strands extracted from partially keystoned Rutherford cables fabricated at Lawrence Berkeley Lab. The tests have shown that the principal source of critical-current degradation occurs at the narrow keystone edge, not at strand crossover points along the flat region of the cable.

3) Further reduction of data from the first study of filament irregularity (sausaging) in NbTi was made, yielding an approximate relationship between the shape of the E-I characteristic and the distribution of filament diameters in the composite. A new technique for measuring the depth profile of the energy gap in filaments extracted from commercial NbTi conductors was developed and demonstrated.

II. ELECTROMECHANICAL RELATIONSHIPS IN NbTi STARTING STRAND MATERIALS

by J. W. Ekin

A. SUMMARY

A series of experiments has been started to measure intrinsic stress relationships in NbTi strand materials. The results will form a data base for designing and setting stress limits in the fabrication of NbTi Rutherford cable conductors. The data are also expected to be useful in determining the optimum combinations of conductor compaction and Lorentz-force pressure in magnet design.

As part of the initial phase of this program, a new apparatus for measuring the effect of transverse compressive stress on the critical current of NbTi has been constructed, modified, and successfully tested. This and other mechanical test apparatus at NBS have been used in this initial study to test the same NbTi starting strand material to investigate the relative electrical effects of various types of stress. The results are preliminary, but several conclusions can be made now:

1) The magnitude of critical-current degradation in NbTi from transverse compression applied at 4 K is comparable in terms of stress in the NbTi filaments.

2) Much more stress can be developed in NbTi filaments from axial tension than from transverse compression, because the soft copper matrix limits the buildup of transverse compression to low levels. At such levels the I_c degradation is only about 4% at 8 T, for example. Thus, in many practical cases, axial tensile stress (from tension or bending strain) is the more important source of critical-current degradation. For example, the I_c degradation is 24% at 7 T when the NbTi filaments are strained 2.7%.

3) The I_c degradation from both types of stress is about 98% reversible, indicating that the effects of stress in NbTi will be seen only when the conductor is under stress.

4) The data indicate that a primary origin of the critical-current degradation in NbTi is a stress induced reversible decrease in the upper critical field. This is true for degradation due to both transverse-compression and axial-tension degradation. It is shown by the large relative increase in the critical-current degradation from both types of stress as the magnetic field approaches the upper critical field.

As a result of these preliminary findings, there are several practical consequences for cable fabrication:

1) In Rutherford cables, not much transverse stress is generated in the NbTi filaments along the cable faces because of yielding

of the soft copper matrix material surrounding the filaments. Much more stress can be developed in the NbTi filaments from axial tension at the cable edges where they are bent around the cable. This may explain the relatively small degradation measured along conductor strands extracted from the face of Rutherford cables compared to the edge region, reported in Sec. III of this NBSIR.

2) The potentially large effect of axial tension indicates that tension on the cable strands should be set at the minimum level needed for cable integrity.

3) Stress annealing the conductor may improve the critical current under some circumstances.

Additional measurements will be needed to determine whether the effect is predominantly a very low temperature (4-K) stress phenomenon or also arises from stress applied at higher temperatures. The consistency of the effects among different NbTi superconductors needs to be tested and further bend testing is needed to relate this to the axial tension results.

B. OVERVIEW OF EXPERIMENTAL PROGRAM

Six types of mechanical tests are planned, most of them at two temperatures, 295 K and 4 K. A matrix of experimental tests is shown in Table 1. Experiments 1 and 2 are transverse compression tests, wherein critical current is measured either during or after stress is applied perpendicular to the sample axis. The first test involves compression applied by flat anvils, the second test by anvil heads which have been machined to match the cross section of the conductor (semi-hydrostatic test). The third experiment measures the dependence of axial tension on the conductor critical current. The last three experiments involve the effect of bending strain on the critical current: hairpin geometry with field perpendicular to the entire length of conductor, hairpin geometry with field parallel to the hairpin legs, and a long-coil bending-strain test.

The overall plan is to perform this matrix of tests on the same starting strand material in order to make comparisons of the relative degradation effects of each type of mechanical loading in a consistent manner. Once the most important types of mechanical stress have been indentified, these stress tests will be performed on a variety of different NbTi materials.

Thus far, preliminary test results on one sample have been obtained for the effects of transverse compressive stress applied at 4 K, axial tensile stress at 4 K, and severe hairpin bending strain applied at 295 K in two magnetic field orientations. These are marked as "one sample" in Table 1. These were the highest priority tests and preliminary results are presented below.

Table 1. Experiment Test Matrix for Electromechanical Relationships in NbTi

	4 K	295 K
1) $\sigma_{\text{transverse uniaxial}}$ $(H_\perp)$	One sample	Next
2) $\sigma_{\text{transverse semi-hydrostatic}}$ $(H_\perp)$	Next	
3) σ_{axial}, $\varepsilon_{\text{axial}}$ $(H_\perp)$	One sample	Next
4) $\varepsilon_{\text{bend, hair pin}}$ $(H_\perp)$	Next	One sample
5) $\varepsilon_{\text{bend, hair pin}}$ (H_{11} to hair pin legs)		One sample
6) $\varepsilon_{\text{bend, long length}}$ $(H_\perp)$		Next

The next priority tests are marked "Next" in Table 1. In the case of the room-temperature transverse compression and axial tension tests, only a few points at high stress levels will be measured initially since these tests are very time consuming and expensive. The reason they are time consuming is that load has to be applied at room temperature and maintained constant during cooldown, requiring a separate experimental run for each data point. This can be accomplished in spite of differential thermal contraction between the various components of the test apparatus by using a servo-hydraulic feedback system described below.

C. TRANSVERSE COMPRESSION TESTS

The effect of axial tension on the critical current of practical multifilamentary NbTi superconductors was first studied about ten years ago.[1] Relatively few electromechanical studies have been made on NbTi superconductors since then, and these have been mostly axial stress studies.[2] Less is known about the effects of stress components other than the axial component.[3] In practical superconducting magnets, however, the superconductor is subjected to three dimensional stresses. Typically the transverse component of stress is large and compressive. For example, in solenoidal magnets the transverse component arises from hoop stress which compresses the magnet winding radially, and in dipole magnets it arises from Lorentz force compression of the magnet windings at the mid plane.

Apparatus

To obtain data on the intrinsic effects of this component of stress on the critical current of practical superconductors, a transverse-stress apparatus has been designed and built. It simultaneously applies mutually perpendicular components of current, high magnetic field and transverse compressive stress to a single strand superconductor in a 4-K liquid helium bath. The apparatus has the following specifications:

Force limit	4.5 kN (~1000 lb)
Maximum magnetic field	10 T
Maximum sample current (two sets of vapor-cooled current leads for different current ranges)	600/3000 A
Test temperature	4 K
Gauge length of test section	1.27 cm

An overview of the test apparatus is shown in Fig. 1. The cryostat in the right foreground houses a 10-T radial-access

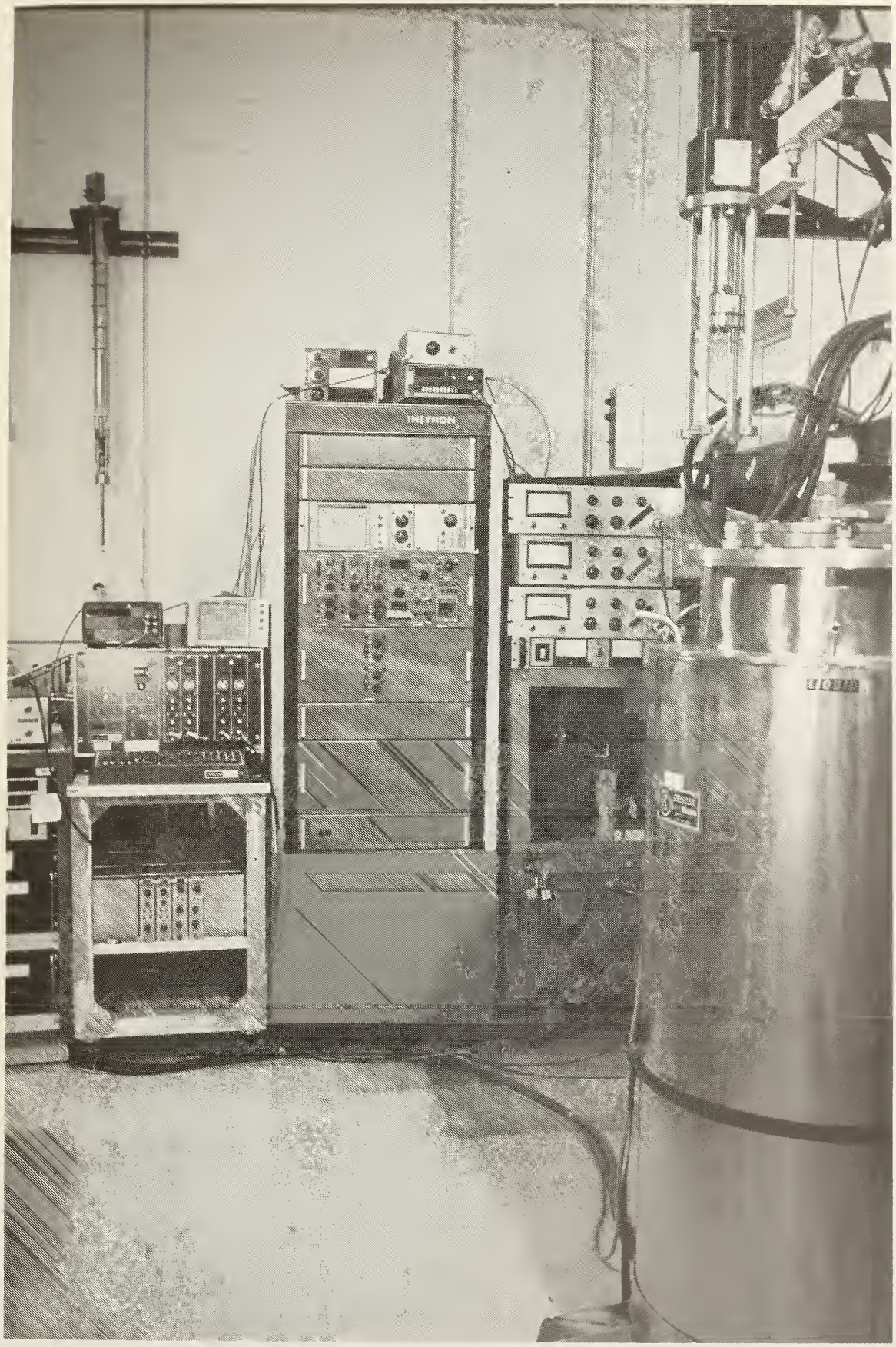

Fig. 1. Transverse compression test system showing 10 T radial access magnet dewar, servohydraulic system, and 900 A battery supply.

magnet. Load is supplied by a servo-hydraulic system; the actuator is positioned above the magnet cryostat and mechanically attached to the sample apparatus after it is inserted into the magnet Dewar. The servohydraulic loading system is powered by an oil pump capable of supplying oil at a pressure of 20 MPa (~3000 psi). It is con-trolled by the comparator circuits shown in the middle of the picture which can operate to control either load, stroke, or sample strain. Operating in load control enables a sample to be loaded at room temperature and load to be maintained constant during cooldown until thermal equilibrium is reached at 4 K. Then the system is switched from load control to stroke control for the actual I_c measurement in both the loaded and unloaded states. For single-strand testing, current is supplied by a 900-A battery supply; for large-conductor and small-cable testing, a 3000-A SCR supply is used.

Figure 2 shows the compression test probe (lying on its side). At right is the head plate and mechanical linkage for connecting the apparaus to the servohydraulic actuator. The force-transfer cyclinder transfers the load to the test section shown at the left of the picture. The top 35 cm of the force-transfer cylinder near the head plate is thinned to increase the thermal resistance to heat flow into the liquid-helium bath.

Figures 3A and 3B show a closeup of the magnet-insert test section and Fig. 4 gives a schematic view of its main components. The sample is prepared in the shape of a flat sided hairpin, or inverted U shape. The ends are soldered to two copper blocks such that the central section of the U passes over a stainless steel anvil head. Compressive load is applied to the central 1.27-cm length of the test section by sandwiching the sample between the upper and lower anvil heads.

The upper anvil head is designed to pivot so that it conforms to the flat surface of the lower anvil head, thereby applying stress uniformly along the sample test section. Also the anvil heads are tapered at the edges where the sample enters and exits the sandwich in order to avoid any stress concentration at the anvil edges. As shown in Fig. 3B, voltage taps are soldered to the sample section within the sandwich region so that the electric field is measured only over the region where stress is uniformly applied to the test specimen.

Magnetic field is applied mutually perpendicular to the direction of the force and the sample current by a radial access magnet. The field is also perpendicular to the hairpin legs so that current transfer is not a problem. (Current transfer voltages can be a problem when the magnet field is aligned parallel to the legs of a hairpin-shaped sample because the increased critical-current density of the filaments for this orientation does not force current to transfer from the surface to the interior filaments).

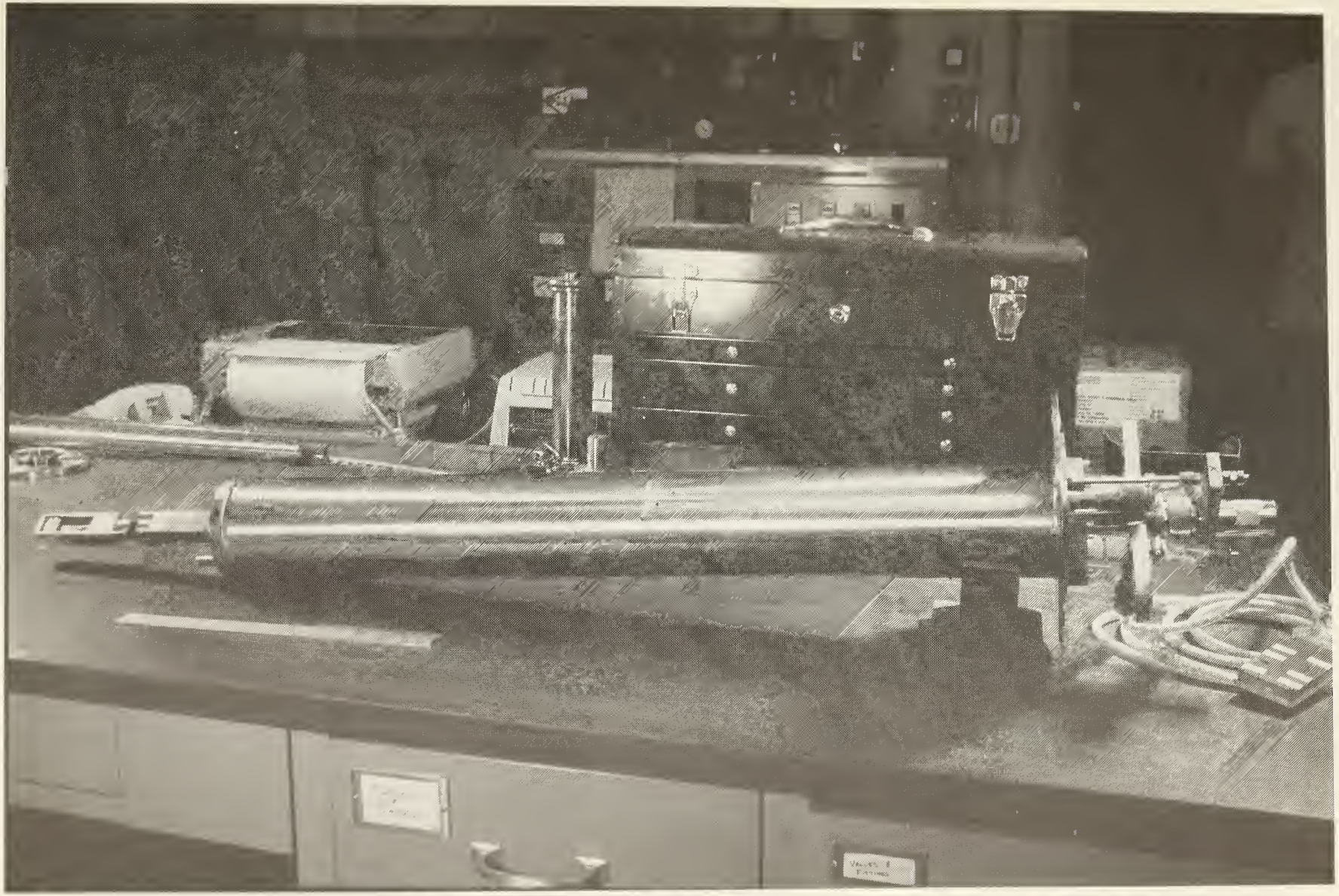

Fig. 2. Compression test probe.

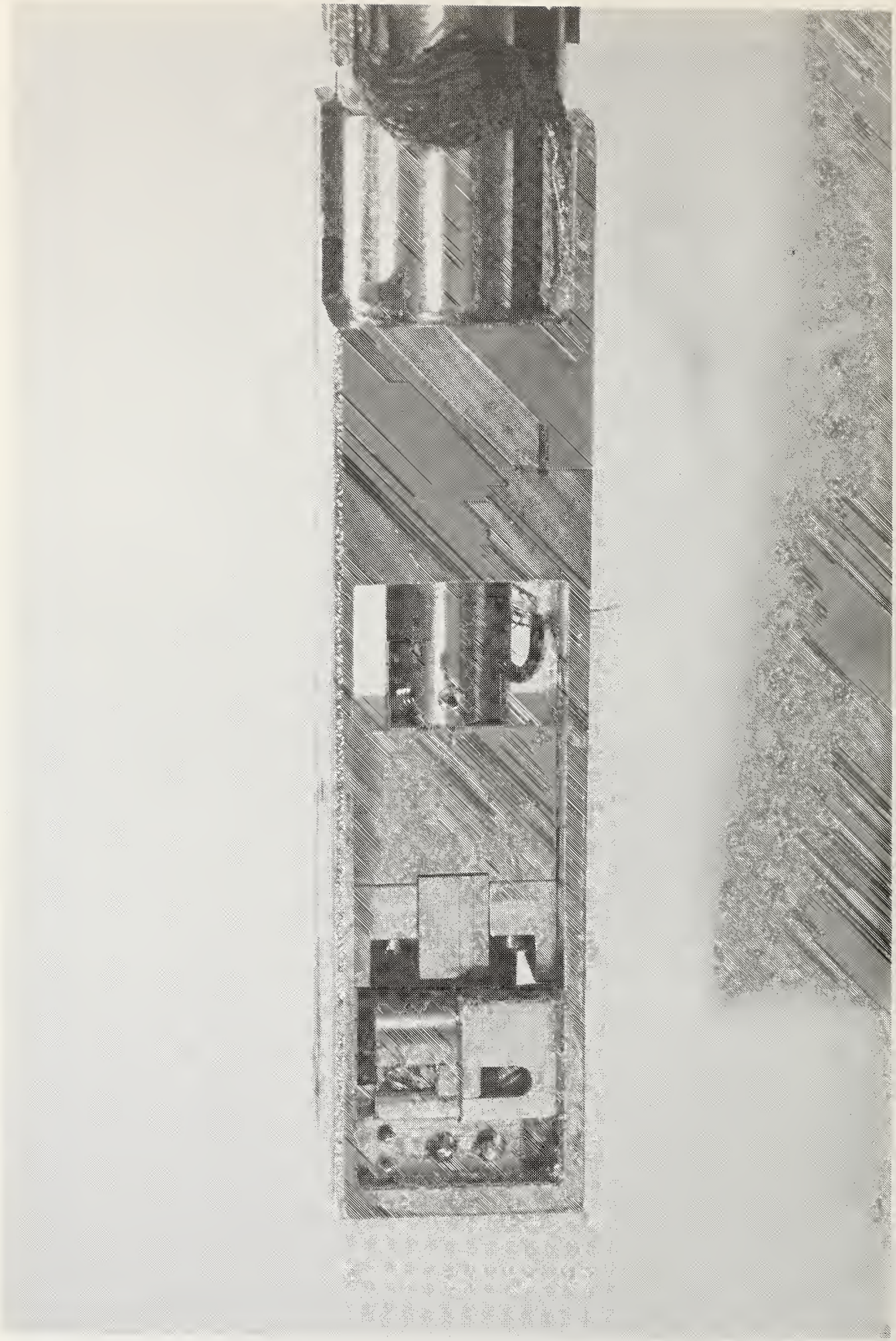

Fig. 3A. Closeup of magnet insert section of transverse-compression test probe: closed anvil heads.

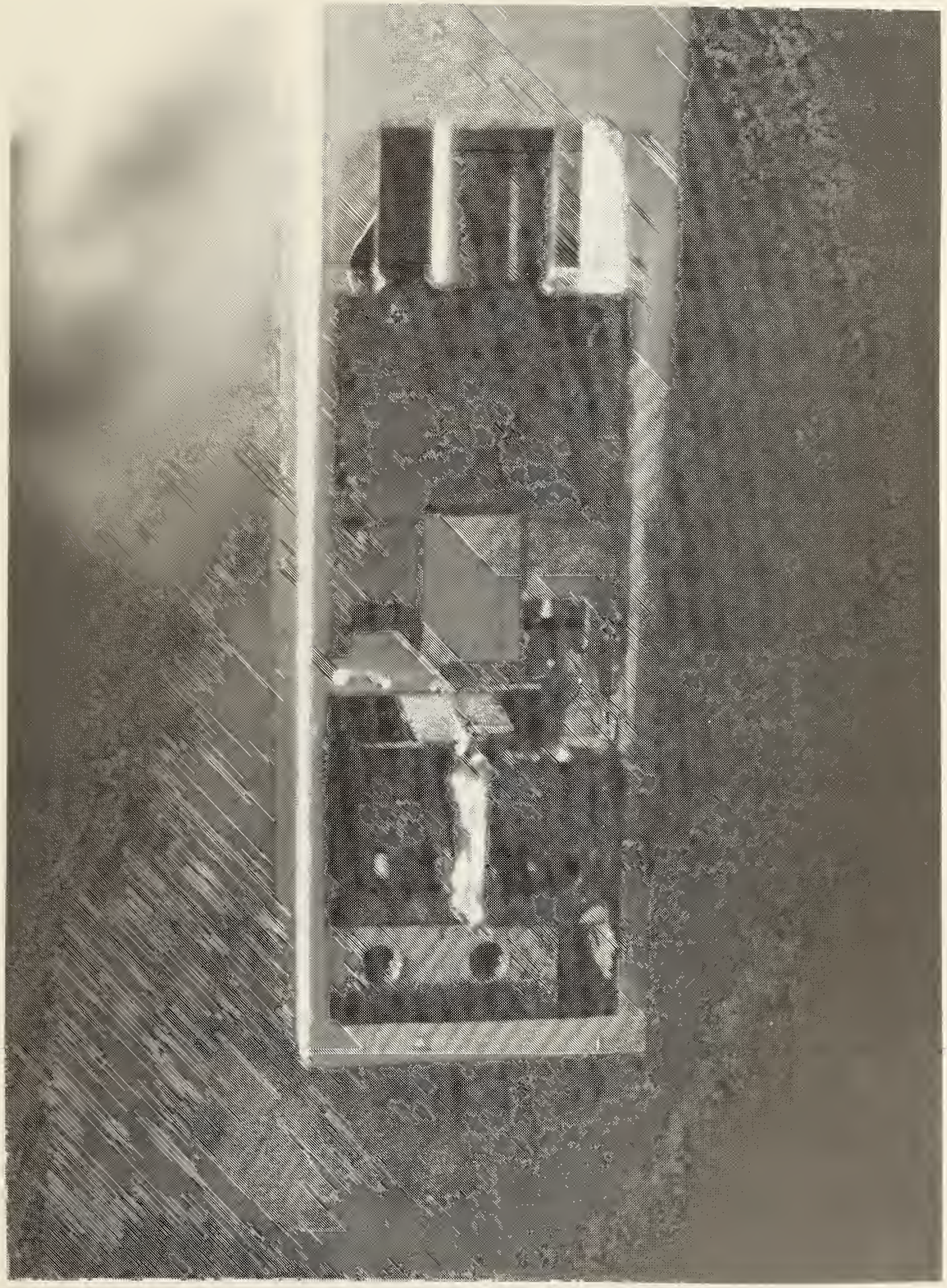

Fig. 3B. Closeup of magnet insert section of transverse-compression test probe: open anvil heads showing voltage tap placement.

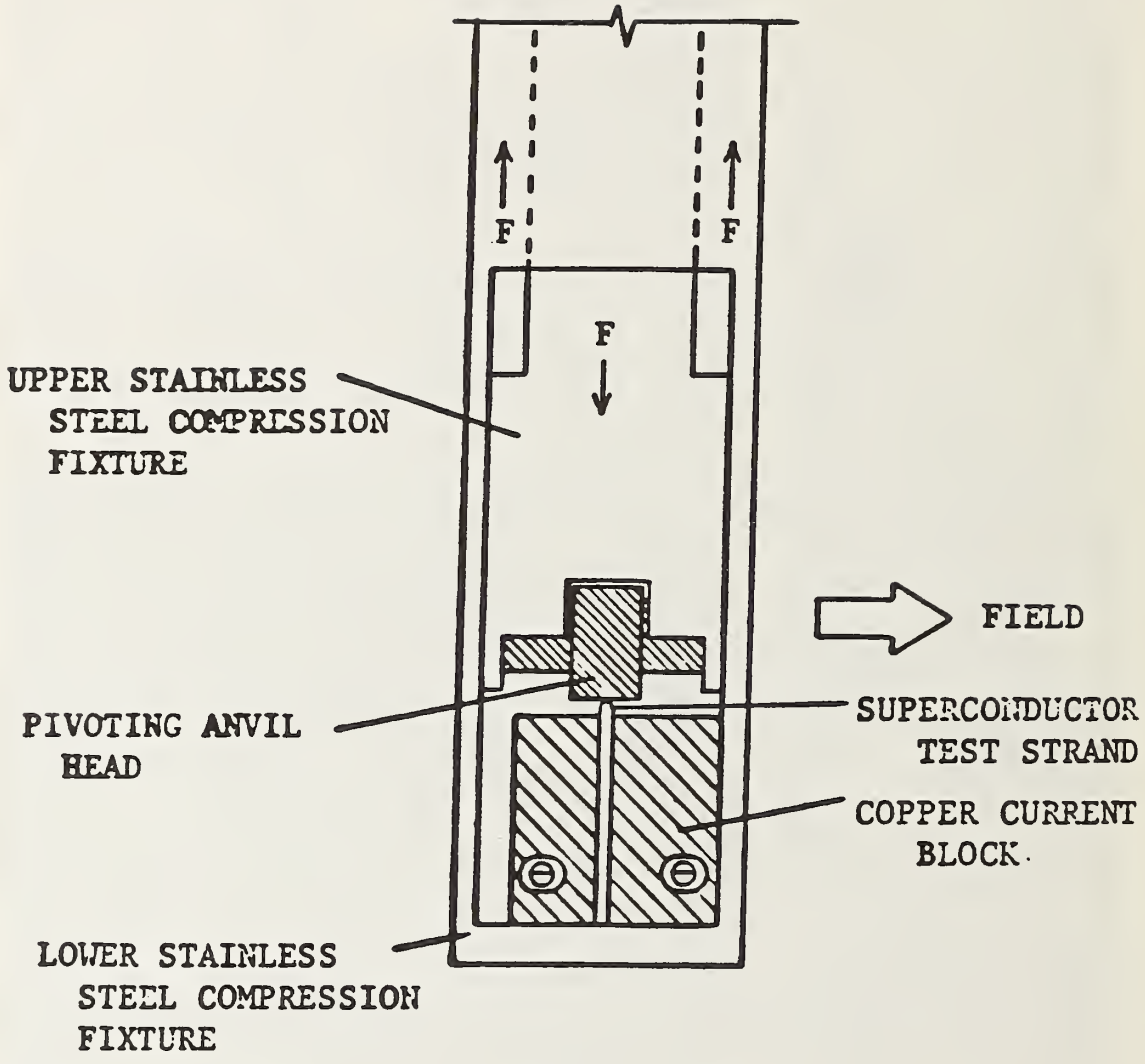

Fig. 4. Schematic view of main components of magnet insert section of transverse-compression test probe.

The first test results were obtained on a NbTi starting strand material that has been used to make many of the 30-strand Rutherford cables in the LBL cable development program (cable Sample B in Sec. III of this report). The NbTi strand characteristics are given in Table 2. It was manufactured using a single stack technique without a diffusion barrier around the filaments.

Results

Figure 5 shows the first measurements of the critical-current degradation effect of transverse stress applied to a multifilamentary NbTi conductor at 4 K. The results are tabulated in Table 3. The ordinate in Fig. 5 is the measured critical current normalized by its starting (zero stress) value. The abscissa is transverse force per unit sample length (top scale). A second abscissa scale is also shown (lower scale) which is an effective overall transverse stress obtained by dividing the applied load by the projected area of the sample along the axis of the applied load. This projected area is simply taken as the length over which compressive load is applied (9.5 mm) multiplied by the starting sample diameter (0.648 mm).

This effective stress is given for comparative purposes only. In the experiment, the anvil heads were flat and the sample round, so this simple method of determining stress does not take into account the small initial contact area, nor the increase in contact area between the anvil heads and the sample as the sample is progressively deformed. However it represents reasonably well the approximate average stress experienced by the NbTi filaments within the composite.

The overall sample strain was quite great because of deformation of the soft copper matrix. It amounted to about 24% at the maximum force-per-sample length (F/L) value of 458 kN/m. This overall sample strain, however, is typically much greater than the actual NbTi filament strain because the copper matrix material yields at a relatively low stress. A picture of the sample deformation after the maximum loading at 4 K (F/L = 458 kN/m) is shown in Fig. 6.

The separation of the voltage taps was relatively small, 8.7 mm. Consequently a relatively high critical-current criterion was used, corresponding to an electric field of 5 μV/cm. The critical-current values at more sensitive criteria are easily calculated however using the measured values of the exponent n given in Table 4 [$I_{c1}/I_{c2} = (E_{c1}/E_{c2})^{1/n}$].

As seen from the results at 8 T in Fig. 5, little degradation ($\leq$ 0.5%) was observed for this sample up to a F/L value of about 100 kN/m (corresponding to an approximate transverse compressive stress, $\sigma_{\perp}$, of about 150 MPa). The degradation effect then increased monotonically to about 4% as

Table 2. Multifilamentary NbTi sample characteristics (billet #5212, spool #3-5).

Strand diameter	0.648 mm
Filament diameter	16 μm
Number of filaments (single stack construction)	648
Copper-to-superconductor volume ratio	1.77
Twist pitch	1.27 cm
Superconductor area	0.1189 mm^2
Total area	0.3295 mm^2

Table 3. Critical current of NbTi Sample #5212 as a function of transverse load per unit length applied at 4 K. Both loaded and unloaded values of the critical current are given at magnetic fields of 7, 5, and 3 T. A 5 μV/cm critical-current criterion was used. The critical current at other criteria may be determined using values of n given in Table 4.

non-Cu area = 1.189E-007 Emax = 0.00% Ec = 5.00uV/cm

Load/unit length (N/m X 10^3)	Ic (Amperes)	Field (Tesla)	Jc (GA/m^2)	JcB (GN/m^3)	Ic/Icm
0	513.250	3.000	4.317	12.950	0.9952
	432.250	4.000	3.635	14.542	0.9965
	364.250	5.000	3.064	15.318	0.9960
	301.100	6.000	2.532	15.194	0.9990
	238.400	7.000	2.005	14.035	1.0465
	174.600	8.000	1.469	11.748	1.0063
	111.200	9.000	0.935	8.417	0.0000
8	363.500	5.000	3.057	15.286	0.9940
14	363.750	5.000	3.059	15.297	0.9947
20	364.000	5.000	3.061	15.307	0.9954
33	364.250	5.000	3.064	15.318	0.9960
51	365.000	5.000	3.070	15.349	0.9981
65	365.250	5.000	3.072	15.360	0.9988
89	365.500	5.000	3.074	15.370	0.9995
	174.600	8.000	1.469	11.748	1.0063
4	174.300	8.000	1.466	11.727	1.0046
116	364.500	5.000	3.066	15.328	0.9967
137	364.250	5.000	3.064	15.318	0.9960
160	365.500	5.000	3.074	15.370	0.9995
	171.200	8.000	1.440	11.519	0.9867
1	173.600	8.000	1.460	11.681	1.0006
179	362.500	5.000	3.049	15.244	0.9913
	171.800	8.000	1.445	11.559	0.9902
1	362.750	5.000	3.051	15.255	0.9919
	173.200	8.000	1.457	11.654	0.9983
201	362.000	5.000	3.045	15.223	0.9899
	171.700	8.000	1.444	11.553	0.9895
1	364.000	5.000	3.061	15.307	0.9954
	173.900	8.000	1.463	11.701	1.0023
237	512.500	3.000	4.310	12.931	0.9937

Table 3 cont'd

non-Cu area = 1.189E-007 Emax = 0.00% Ec = 5.00uV/cm

Load/unit length N/m X 10^3	Ic (Amperes)	Field (Tesla)	Jc (GA/m^2)	JcB (GN/m^3)	Ic/Icm
237	169.900	8.000	1.429	11.431	0.9793
0	513.000	3.000	4.315	12.944	0.9947
	362.750	5.000	3.051	15.255	0.9919
225	513.000	3.000	4.315	12.944	0.9947
1	513.000	3.000	4.315	12.944	0.9947
265	513.000	3.000	4.315	12.944	0.9947
	363.000	5.000	3.053	15.265	0.9926
	169.000	8.000	1.421	11.371	0.9741
0	512.750	3.000	4.312	12.937	0.9942
	362.750	5.000	3.051	15.255	0.9919
	173.100	8.000	1.456	11.646	0.9977
0	512.250	3.000	4.308	12.925	0.9932
	362.250	5.000	3.047	15.234	0.9906
	172.600	8.000	1.452	11.613	0.9948
290	512.500	3.000	4.310	12.931	0.9937
	362.500	5.000	3.049	15.244	0.9913
	169.900	8.000	1.429	11.431	0.9793
2	513.000	3.000	4.315	12.944	0.9947
	362.000	5.000	3.045	15.223	0.9899
	173.200	8.000	1.457	11.654	0.9983
334	362.750	5.000	3.051	15.255	0.9919
	298.300	6.000	2.509	15.053	0.9897
	234.800	7.000	1.975	13.824	1.0307
	169.000	8.000	1.421	11.371	0.9741
1	363.500	5.000	3.057	15.286	0.9940
	299.900	6.000	2.522	15.134	0.9950
	236.600	7.000	1.990	13.929	1.0386
	172.700	8.000	1.453	11.620	0.9954
396	513.500	3.000	4.319	12.956	0.9956
	431.750	4.000	3.631	14.525	0.9954
	363.600	5.000	3.058	15.290	0.9943
	298.800	6.000	2.513	15.078	0.9914
	234.000	7.000	1.968	13.776	1.0272
	167.800	8.000	1.411	11.290	0.9672
1	514.250	3.000	4.325	12.975	0.9971

Table 3 cont'd

non-Cu area = 1.189E-007 Emax = 0.00% Ec = 5.00uV/cm

Load/unit length N/m X 10^3	Ic (Amperes)	Field (Tesla)	Jc (GA/m^2)	JcB (GN/m^3)	Ic/Icm
1	432.250	4.000	3.635	14.542	0.9965
	364.300	5.000	3.064	15.320	0.9962
	300.400	6.000	2.527	15.159	0.9967
	236.900	7.000	1.992	13.947	1.0399
	172.900	8.000	1.454	11.634	0.9965
458	515.250	3.000	4.334	13.001	0.9990
	433.000	4.000	3.642	14.567	0.9983
	364.200	5.000	3.063	15.316	0.9959
	299.300	6.000	2.517	15.103	0.9930
	224.400	7.000	1.887	13.211	0.9851
	168.100	8.000	1.414	11.310	0.9689
1	515.750	3.000	4.338	13.013	1.0000
	433.750	4.000	3.648	14.592	1.0000
	365.700	5.000	3.076	15.379	1.0000
	301.400	6.000	2.535	15.209	1.0000
	227.800	7.000	1.916	13.411	1.0000
	173.500	8.000	1.459	11.674	1.0000

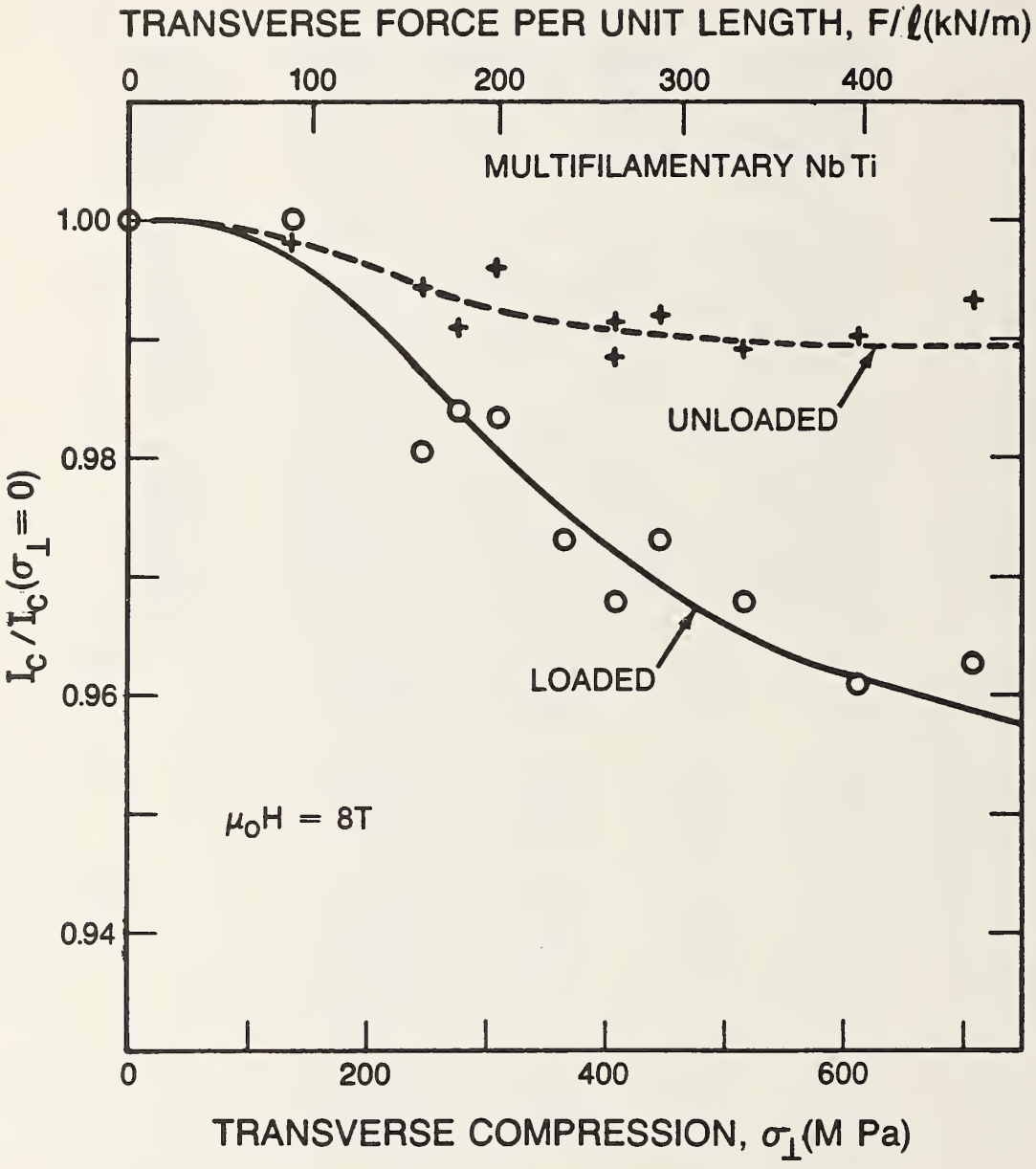

Fig. 5. Effect of transverse compressive force on the critical current of NbTi Sample #5212 at 8 T.

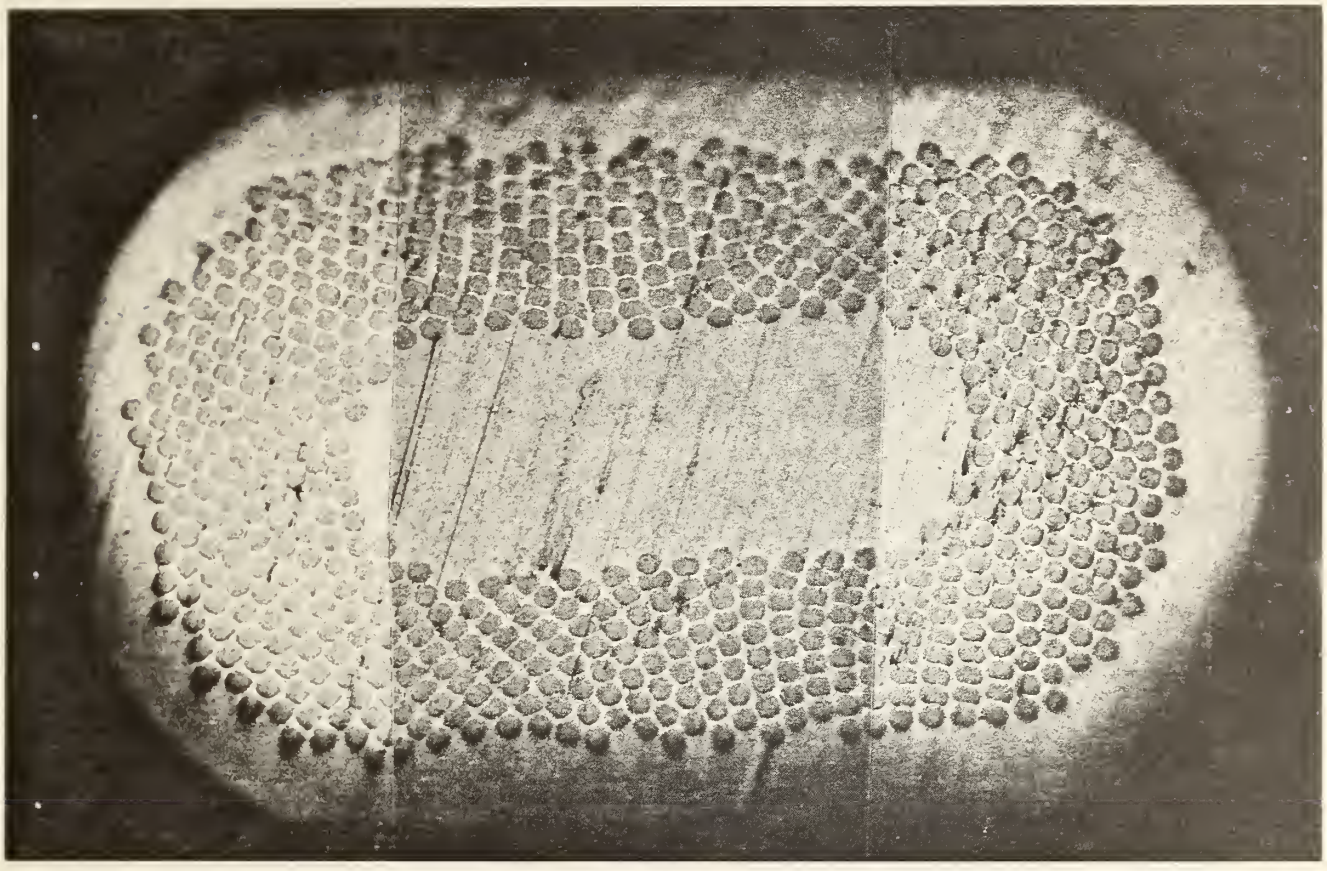

Fig. 6. Cross sectional view of NbTi Sample #5212 after application of 458 kN/mF transverse load at 4 K.

F/L was increased to 460 kN/m ($\sigma_\perp$ = 700 MPa). Because the yield stress of the copper matrix is so low, it is difficult to generate much higher stress without severe sample deformation; see Figure 6. Thus, the maximum critical-current degradation from transverse stress is about 4% at 7 T.

The effect was almost completely reversible. Upon unloading from F/L = 460 kN/m, the critical current recovered to within 0.5% of its original value. This recovery took place even though the sample was permanently deformed by about 25%.

The transverse stress degradation was largest at high magnetic field. This is shown in Figs. 7 and 8, which show that the effect was less than 0.5 % at the maximum F/L value of 460 kN/m at both 5 T and 3 T.

It is also apparent in Figs. 7 and 8 that there was a small (0.5%) enhancement of the critical current at high values of F/L. This is probably an aspect-ratio effect caused by an enhancement of the pinning effectiveness for this field orientation, which resulted from the deformation of the filaments at high stress levels. A listing of these lower-field results is also given in Table 3.

Values of the exponent n for this sample are given as a function of magnetic field in Fig. 9 and Table 4. For this sample, which was fabricated using a single stack technique with relatively large filaments (17 μm), n reached values of over 80 at low magnetic fields. This is relatively high for multifilamentary NbTi superconductors.

D. AXIAL TENSION TESTS

Tests at Magnetic Fields Up to 7 T

To compare the relative magnitudes of the effects of transverse compression with axial tension, another sample of the same starting material (see Table 2) was tested in an axial tensile mode. The experiments were carried out using an apparatus described in Ref. 4. This apparatus utilizes a 7 T radial-access magnet and the same servohydraulic loading system described above. The sample gauge length was 28.4 cm and the voltage-tap separation was 3.3 cm, both of which are longer than in the transverse compression tests. Consequently the critical current could be directly measured at more sensitive electric-field criteria.

Results corresponding to a 5 μV/cm criterion (the same as that used for the transverse compression tests) are given in Fig. 10 as a function of stress and in Fig. 11 as a function of strain. A tabulation of the results is also given in Table 5. Stress was calculated using the total conductor cross sectional area. Stress was calculated using the overall conductor cross

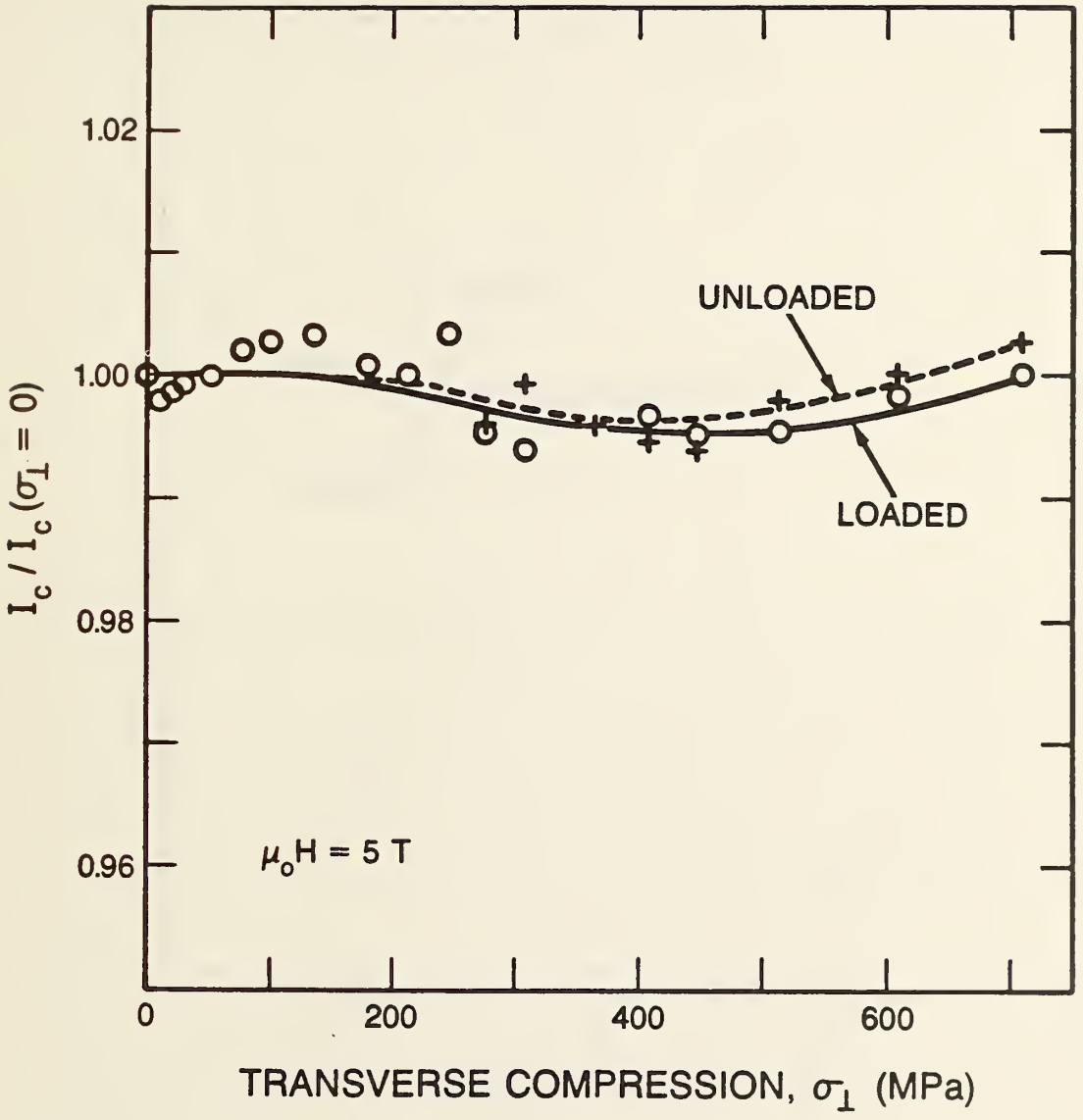

Fig. 7. Effect of transverse compressive force on the critical current of NbTi Sample #5212 at 5 T.

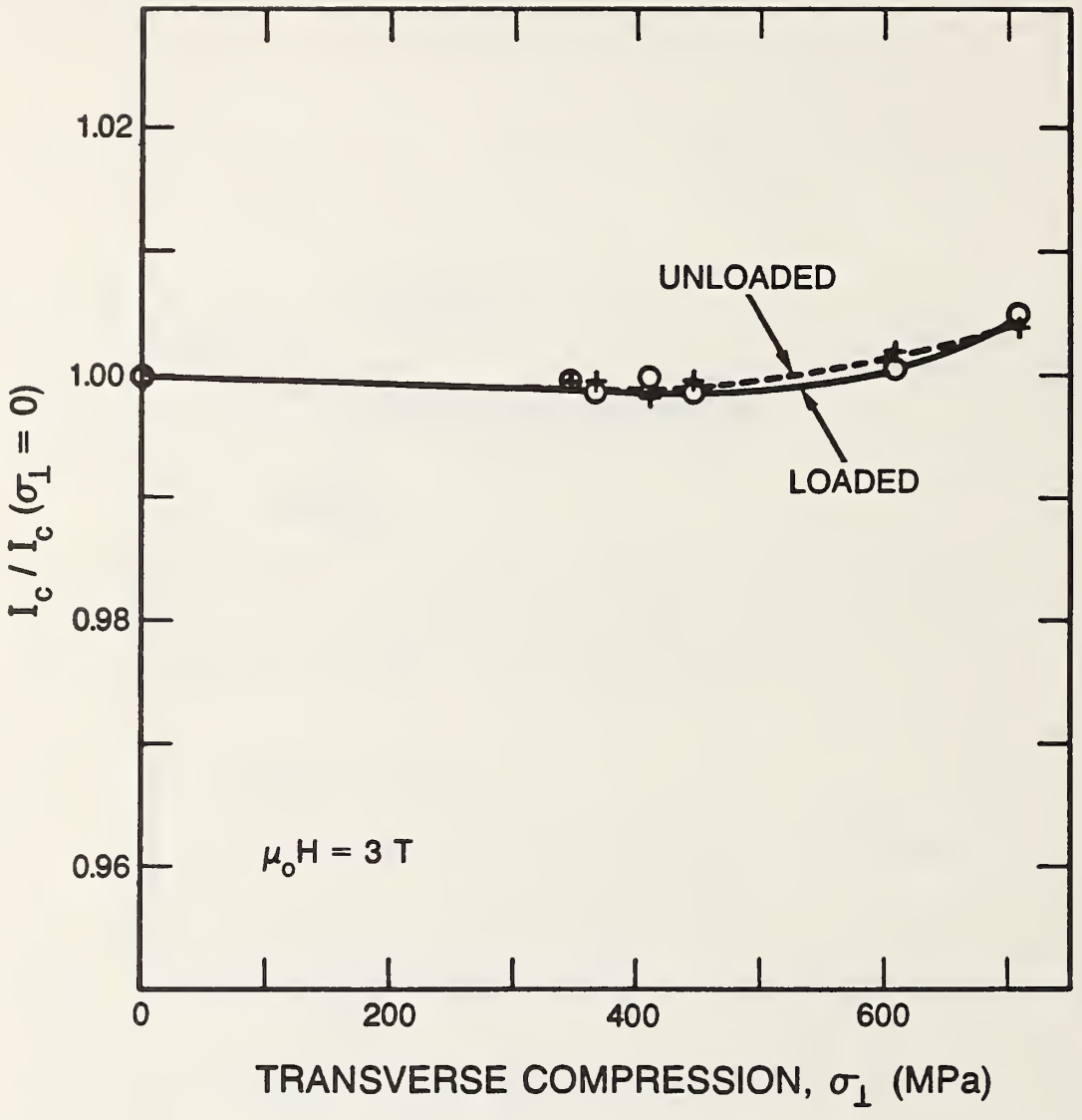

Fig. 8. Effect of transverse compressive force on the critical current of NbTi Sample #5212 at 3 T.

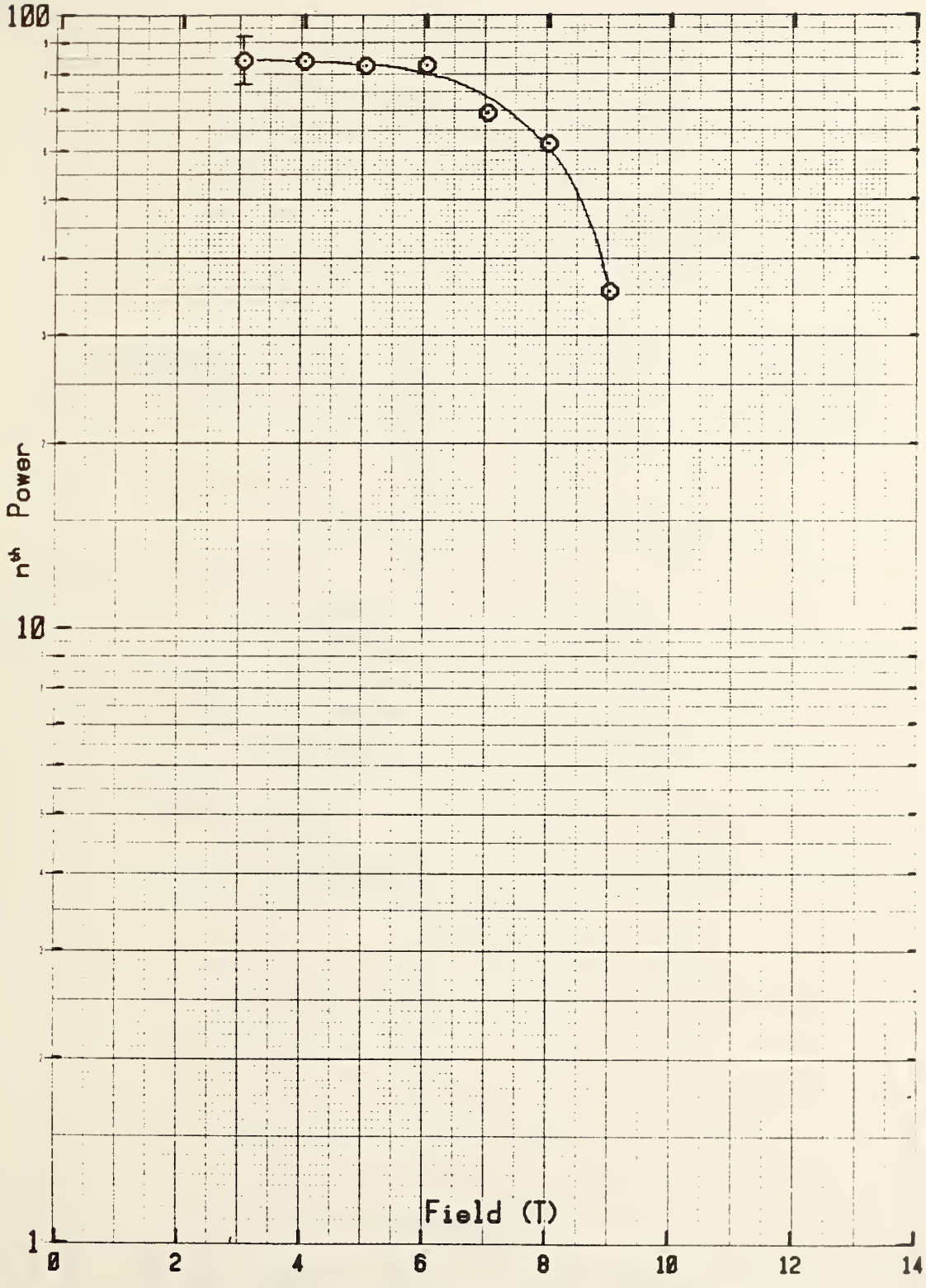

Fig. 9. Magnetic field dependence of the exponent n for NbTi Sample #5212 measured in the short-sample transverse-stress apparatus. The power n is defined by $E_{c1}/E_{c2} = (I_{c1}/I_{c2})^n$.

Table 4. Exponent n for NbTi Sample #5212 as a function of magnetic field measured at zero load in the short-sample transverse-stress apparatus. The power n is defined by $E_{c1}/E_{c2} = (I_{c1}/I_{c2})^n$.

n evaluated at 0.000 strain

Field (T)	nth power
3.000	84.00
4.000	83.79
5.000	82.40
6.000	82.54
7.000	68.97
8.000	61.43
9.000	35.28

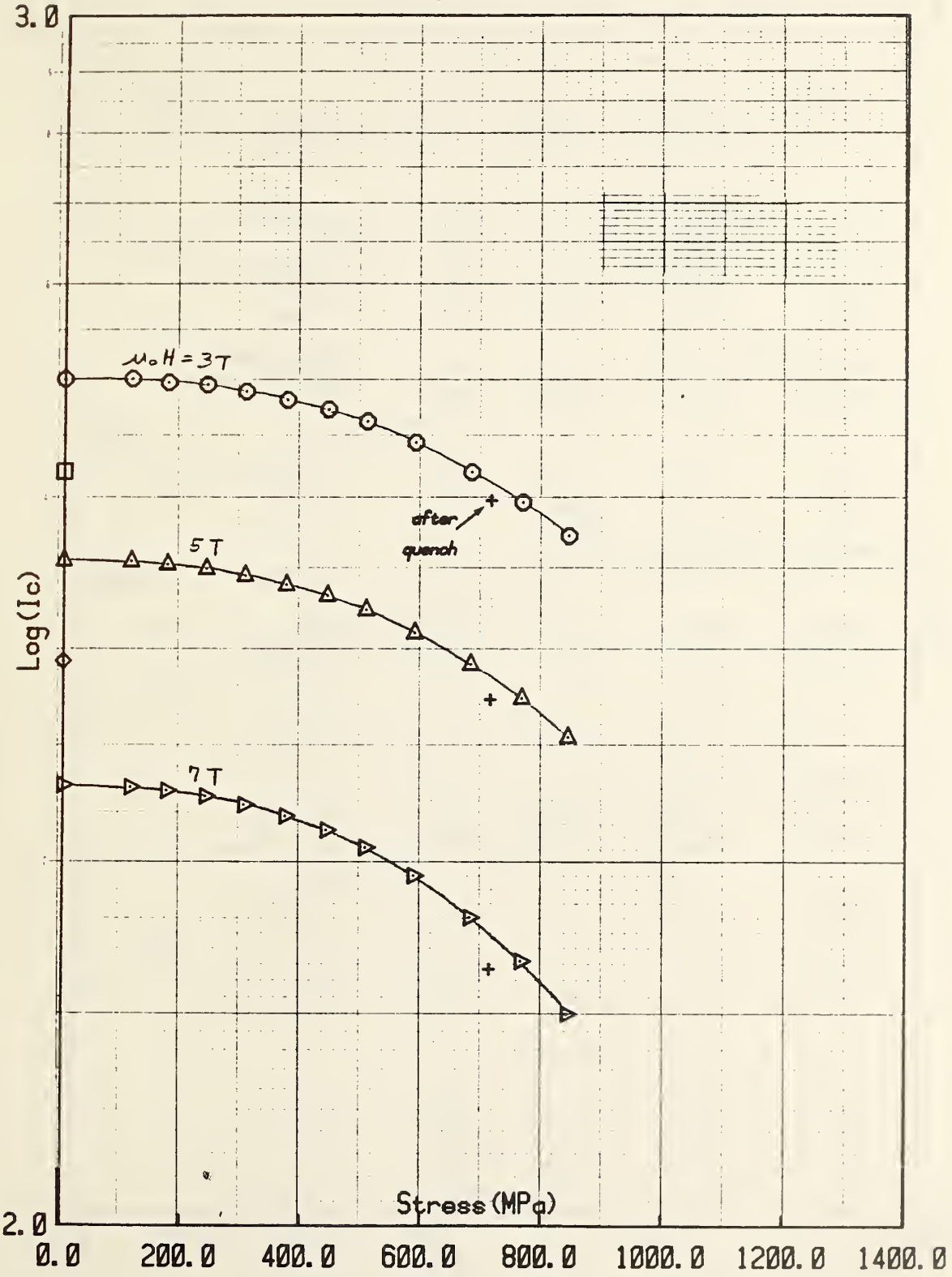

Fig. 10. Effect of axial tensile stress on the critical current of NbTi Sample #5212 at 7, 5, and 3 T.

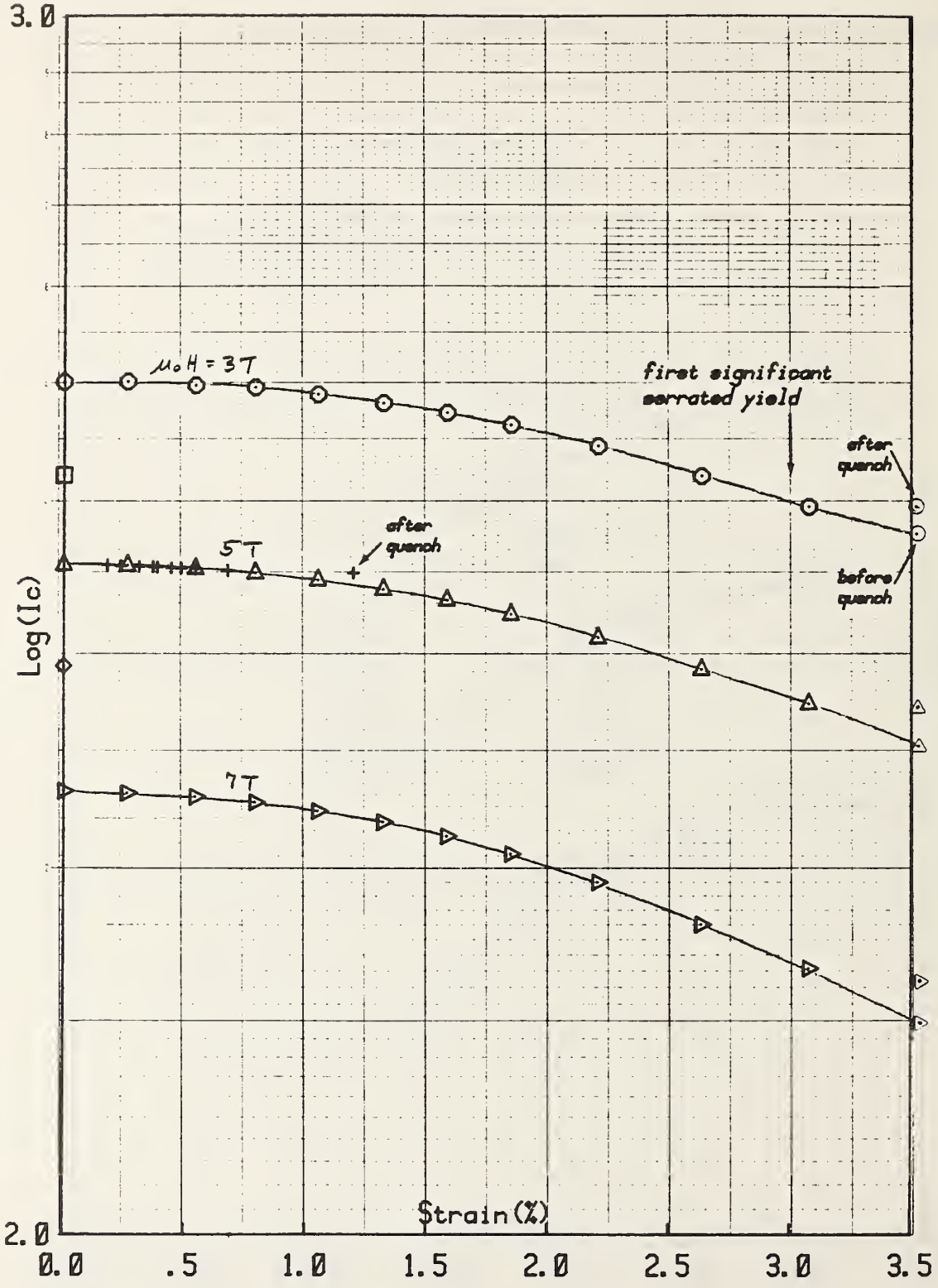

Fig. 11. Effect of axial tensile strain on the critical current of NbTi Sample #5212 at 7, 5, and 3 T.

Table 5. Critical current of NbTi Sample #5212 as a function of axial tensile stress and strain applied at 4 K. Loaded and unloaded values of the critical current are given at magnetic fields of 7, 5, and 3 T. A 5 μV/cm critical current criterion was used. The critical current at other criteria may be determined using values of n given in Table 6.

SC. non-Cu area = 1.189E-007 Emax = 0.00% Ec = 5.00uV/cm Efract = 4.061

E (%)	Stress MPa	Ic (Amperes)	Field (Tesla)	Jc (GA/m^2)	JcB (GN/m^3)	Ic/Icm
0.00		499.310	3.000	4.199	12.598	1.0000
		418.810	4.000	3.522	14.090	1.0000
		353.630	5.000	2.974	14.871	1.0000
		292.230	6.000	2.458	14.747	1.0000
		230.720	7.000	1.941	13.584	1.0000
0.26	73	499.630	3.000	4.202	12.606	1.0006
		353.070	5.000	2.970	14.848	0.9984
		229.900	7.000	1.934	13.535	0.9965
0.55	143	495.940	3.000	4.171	12.513	0.9933
		350.800	5.000	2.950	14.752	0.9920
		228.330	7.000	1.920	13.443	0.9896
0.18		353.450	5.000	2.973	14.864	0.9995
0.79	222	493.810	3.000	4.153	12.460	0.9890
		347.980	5.000	2.927	14.634	0.9840
		225.950	7.000	1.900	13.302	0.9793
0.24		352.630	5.000	2.966	14.829	0.9972
1.05	297	487.380	3.000	4.099	12.297	0.9761
		343.450	5.000	2.889	14.443	0.9712
		222.350	7.000	1.870	13.091	0.9637
0.31		352.200	5.000	2.962	14.811	0.9960
1.32	373	479.630	3.000	4.034	12.102	0.9606
		337.480	5.000	2.838	14.192	0.9543
		217.700	7.000	1.831	12.817	0.9436
0.37		352.080	5.000	2.961	14.806	0.9956
1.58	441	471.000	3.000	3.961	11.884	0.9433
		330.750	5.000	2.782	13.909	0.9353
		211.980	7.000	1.783	12.480	0.9188
0.39		351.780	5.000	2.959	14.793	0.9948
1.85	506	460.440	3.000	3.873	11.618	0.9222
		322.000	5.000	2.708	13.541	0.9106
		205.080	7.000	1.725	12.074	0.8889
0.44		351.250	5.000	2.954	14.771	0.9933
2.21	587	442.440	3.000	3.721	11.163	0.8861

Table 5 cont'd

non-Cu area = 1.189E-007 Emax = 0.00% Ec = 5.00uV/cm Efract = 4.061

E (%)	Stress MPa	Ic (Amperes)	Field (Tesla)	Jc (GA/m^2)	JcB (GN/m^3)	Ic/Icm
2.21	587	308.250	5.000	2.593	12.963	0.8717
		194.400	7.000	1.635	11.445	0.8426
0.49		351.080	5.000	2.953	14.764	0.9928
2.63	680	418.310	3.000	3.518	10.555	0.8378
		290.380	5.000	2.442	12.211	0.8211
		179.600	7.000	1.511	10.574	0.7784
0.55		350.600	5.000	2.949	14.744	0.9914
3.08	765	394.940	3.000	3.322	9.965	0.7910
		272.300	5.000	2.290	11.451	0.7700
		165.350	7.000	1.391	9.735	0.7167
0.68		349.580	5.000	2.940	14.701	0.9886
3.52	842	370.690	3.000	3.118	9.353	0.7424
		252.900	5.000	2.127	10.635	0.7152
		149.530	7.000	1.258	8.803	0.6481
1.20		347.980	5.000	2.927	14.634	0.9840
3.52	713	396.190	3.000	3.332	9.996	0.7935
		271.530	5.000	2.284	11.419	0.7678
		162.830	7.000	1.370	9.587	0.7058

sectional area. The results of Fig. 10 compared with Figs. 5, 7, and 8 show that the effect of axial tensile stress applied at 4 K is significantly greater than the effect of transverse compression at 4 K, in terms of the overall stress on the conductor. For example, the degradation of the critical current at 7 T is about 24% at an average tensile stress of 700 MPa (tensile strain of 2.7%). This compares with an 8 T degradation of about 4% at 700 MPa transverse stress, about one sixth.

However, because the copper matrix has a relatively low yield stress (about 140 MPa), the axial stress in the NbTi filaments is actually higher (about 2.3 times higher) than the overall stress on the conductor. Accounting for this, the degradation from axial tension at 700 MPa in the NbTi filaments corresponds to about 340 MPa overall conductor stress, or a degradation of only about 7% at 8 T. Thus, the two effects (axial and transverse) are nearly comparable in terms of actual NbTi filament stress. The slight difference in critical-current degradation between the two components of stress may arise from texturing of the filaments introduced during fabrication.

Much more stress can be developed in the NbTi filaments from axial tension than from transverse compression because the soft copper matrix limits the buildup of transverse compression. Thus, in many practical cases, axial tensile stress is the more important source of critical-current degradation.

In other respects the two types of stress effects (axial and transverse) are similar. Both stress effects increase with increasing magnetic field. For example, in Table 5 the degradation at an axial stress of 700 MPa (2.7% strain) was 16% at 3 T, increased to 18% at 5 T, and then to 22% at 7 T.

Both types of stress effects are highly reversible also. For example, upon unloading from an applied axial stress of about 700 MPa (strain of 2.7%) the critical current at 5 T recovered to within 1% of its original value. This extreme reversibility persisted up to the fracture point of the sample, which occurred at a strain of 4.06%. Just before the sample fractured, the critical current still recovered to within 1.5% of its original value upon unloading the sample; see Table 5.

A significant serrated yield event (load drop of 10%) took place at a tensile strain of 3.0%. Figures 10 and 11 show that this did not significantly affect the smooth monotonic decrease of the critical current with stress and strain.

However, a quench event took place while the sample was under high stress, 842 MPa (3.5% strain), which significantly affected the degradation. As shown in Fig. 11, the critical current rose significantly after the transient heating that accompanied the thermal runaway and current-supply shutdown. During this quench event the strain in the sample was maintained constant, but the stress decreased about 15% due to annealing.

Table 6. Exponent n for NbTi Sample #5212 as a function of magnetic field measured at zero load in the long sample axial stress apparatus.

n evaluated at 0.000 % strain

Field (T)	nth power
3.000	76.09
4.000	75.78
5.000	75.20
6.000	72.89
7.000	71.92

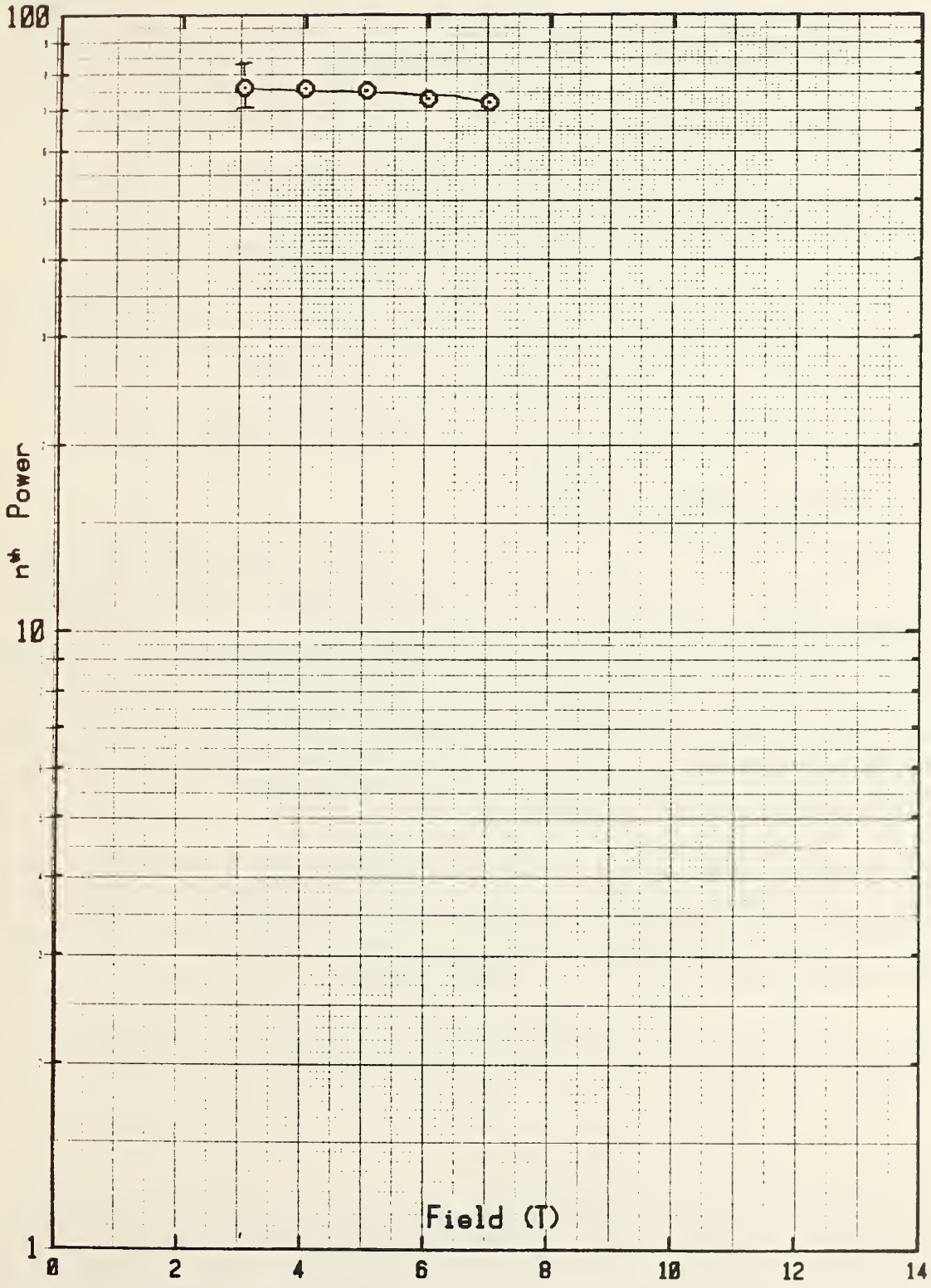

Fig. 12. Magnetic field dependence of the exponent n for NbTi Sample #5212 measured in the long sample axial stress apparatus.

Thus the event indicates that critical-current degradation in NbTi is predominantly stress controlled rather than strain controlled, since strain was constant while both the stress and critical current recovered. The event suggests that strain and deformation alone are not the prime causes of degradation in NbTi, but rather the stress that accompanies deformation is the major cause, at least at 4 K. Thus, stress annealing of the conductor might be a method for improving the critical current.

Values of n determined in the axial stress apparatus are given in Table 6 and plotted in Fig. 12. As seen from the data, n was nearly constant between 3 T and 7 T and had a value of about 75. This is slightly smaller than the value of n determined above using the short-sample transverse stress apparatus. The difference is not great, 83 vs. 75, but it may be significant. Specifically, it may be due to the longer length of the sample measured in the axial stress apparatus, which would include long as well as short filament irregularities along the sample test length. It thus would be more sensitive to degradation of n arising from longer-filament irregularities.

Tests at Magnetic Fields Above 7 T

To measure the effect at magnetic fields approaching the upper critical field, another series of tests were made at fields above 7 T. These were made using a short sample test apparatus (described in Ref. 5) that was designed for use in the Bitter magnets at the National Magnet Laboratory. The results are shown in Fig. 13 and tabulated in Table 7. The overlap in critical current results at 7 T is good if the results are corrected to the same temperature. These measurements were carried out at sea level in boiling helium at an approximate temperature of 4.2 K. The results below 7 T were made about 1600 m above sea level at an approximate temperature of 4 K.

The results show quite clearly that the relative magnitude of the stress effect becomes much larger as the magnetic field approaches the upper critical field. At 2.14% strain, for example, the critical-current degradation is 19% at 8 T, 24% at 9 T, 42% at 10 T, and rises to 60% at 10.5 T.

The dependence of n on magnetic field is given in Fig. 14 and Table 8. Note the rapid decrease in this high-n sample at fields above 7 T.

E. BENDING STRAIN TESTS AT 295 K

To compare these 4 K stress effects with room-temperature bending-strain effects, the same superconductor strand material was subjected to a severe bending strain test. The conductor was bent into a hairpin shape at 295 K and placed transversely to the bore of a 9 T solenoidal magnet. This field orientation was chosen to eliminate current-transfer effects. These would

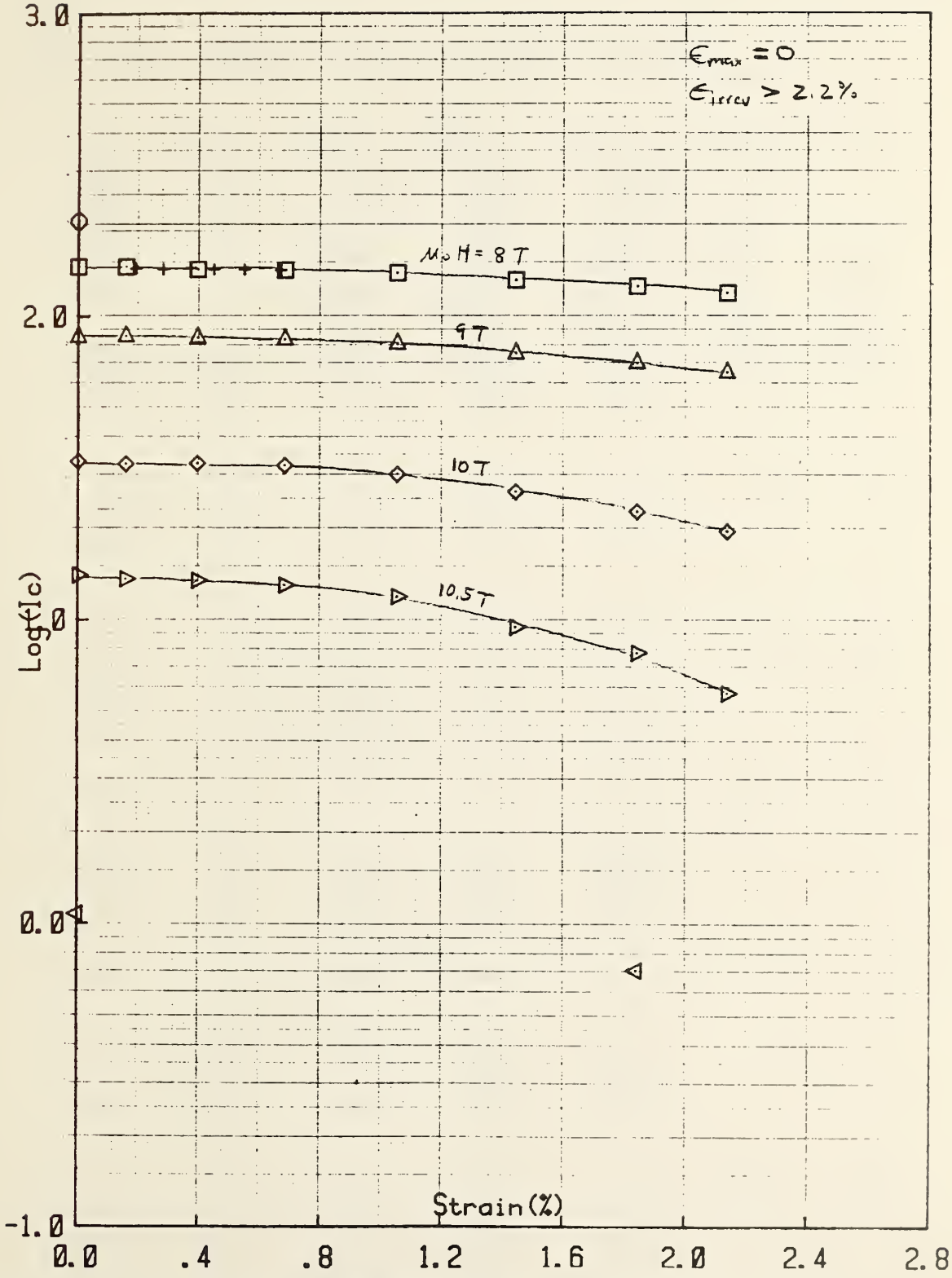

Fig. 13. High field dependence of the axial strain effect on the critical current of NbTi Sample #5212.

Table 7. High-field critical current of NbTi Sample #5212 as a function of axial tensile strain applied at 4 K.

S.C. area = 1.189E-007 Emax = 0.00% Ec = 2.00uV/cm

E (%)	Eo (%)	Ic (Amperes)	Field (Tesla)	Jc (GA/m^2)	JcB (GN/m^3)	Ic/Icm
0.00	0.00	206.070	7.000	1.733	12.132	1.0000
		145.900	8.000	1.227	9.817	1.0000
		86.116	9.000	0.724	6.518	1.0000
		33.235	10.000	0.280	2.795	1.0000
		14.018	10.500	0.118	1.238	1.0000
		1.075	11.000	0.009	0.099	1.0000
0.16	0.16	145.820	8.000	1.226	9.811	0.9995
		85.936	9.000	0.723	6.505	0.9979
		32.856	10.000	0.276	2.763	0.9886
		13.621	10.500	0.115	1.203	0.9717
0.39	0.39	144.100	8.000	1.212	9.695	0.9877
		84.915	9.000	0.714	6.428	0.9861
		32.687	10.000	0.275	2.749	0.9835
		13.429	10.500	0.113	1.186	0.9580
0.19	0.19	143.650	8.000	1.208	9.668	0.9848
0.68	0.68	141.970	8.000	1.194	9.552	0.9731
		83.477	9.000	0.702	6.319	0.9894
		32.017	10.000	0.269	2.693	0.9934
		12.943	10.500	0.109	1.143	0.9233
0.28	0.28	142.870	8.000	1.202	9.613	0.9792
1.05	1.05	138.600	8.000	1.166	9.326	0.9500
		80.909	9.000	0.680	6.124	0.9395
		30.009	10.000	0.252	2.524	0.9029
		11.864	10.500	0.100	1.049	0.8463
0.37	0.37	143.800	8.000	1.209	9.675	0.9858
1.44	1.44	131.220	8.000	1.104	8.829	0.8994
		75.003	9.000	0.631	5.677	0.8710
		26.253	10.000	0.221	2.209	0.7899
		9.398	10.500	0.079	0.830	0.6704
0.45	0.45	142.620	8.000	1.200	9.596	0.9775
1.84	1.84	125.030	8.000	1.052	8.413	0.8570
		69.557	9.000	0.585	5.265	0.8077
		22.557	10.000	0.190	1.897	0.6787
		7.732	10.500	0.065	0.683	0.5516
0.55	0.55	142.560	8.000	1.199	9.592	0.9771

Table 7 cont'd

SC area = 1.189E-007 Emax = 0.00% Ec = 2.00uV/cm

E (%)	Eo (%)	Ic (Amperes)	Field (Tesla)	Jc (GA/m^2)	JcB (GN/m^3)	Ic/Icm
2.14	2.14	118.430	8.000	0.996	7.968	0.8117
		64.679	9.000	0.544	4.896	0.7558
		19.369	10.000	0.163	1.629	0.5828
		5.684	10.500	0.048	0.502	0.4055
0.67	0.67	141.630	8.000	1.191	9.530	0.9707

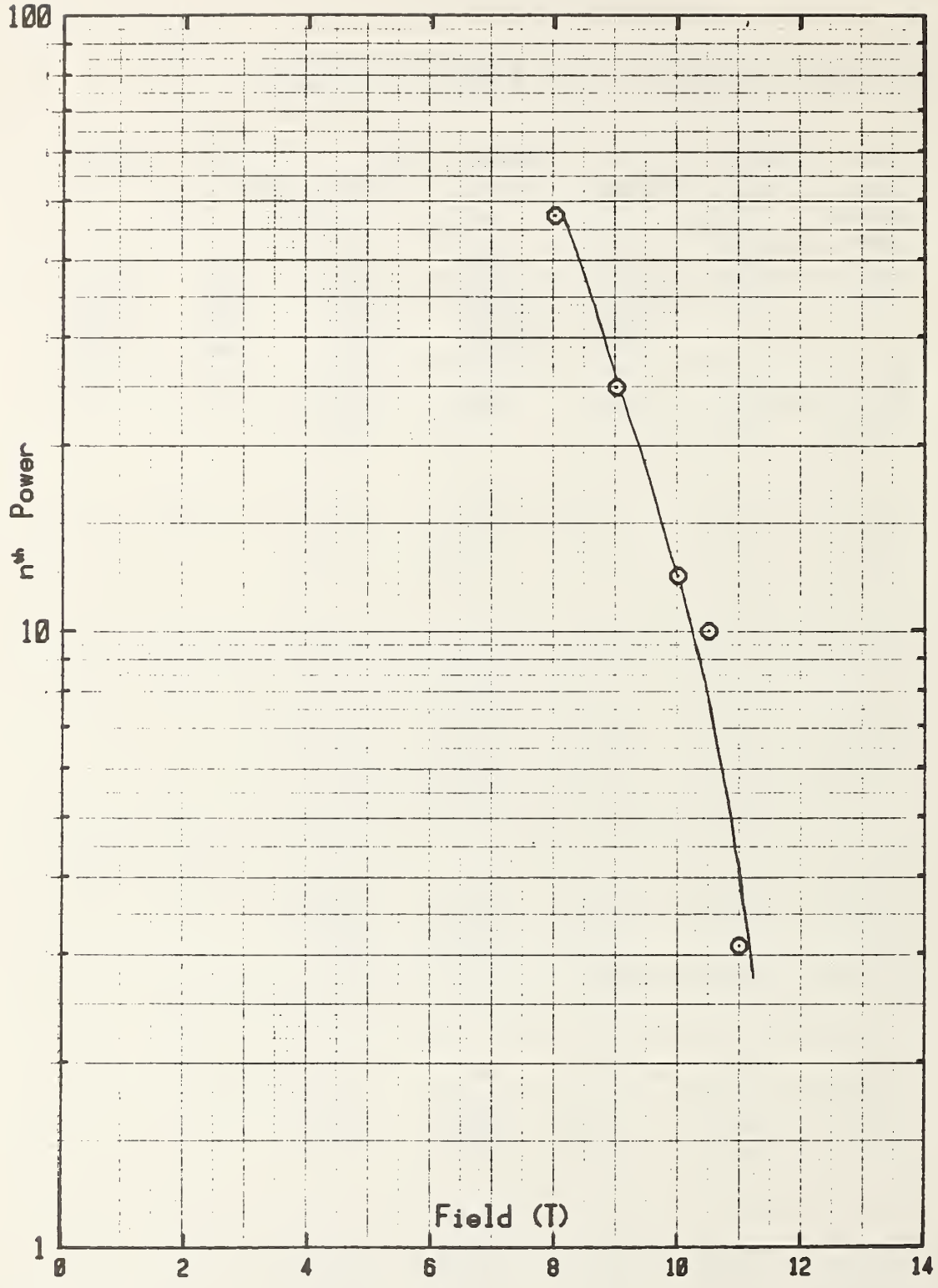

Fig. 14. Magnetic field dependence of the exponent n measured for NbTi Sample #5212 at high fields.

Table 8. High-field dependence of the exponent n on magnetic field, measured for NbTi Sample #5212 at zero load in the short-sample high-field test apparatus.

n evaluated at 0.000 % strain	
Field (T)	nth power
8.000	47.09
9.000	24.75
10.000	12.23
10.500	9.95
11.000	3.08

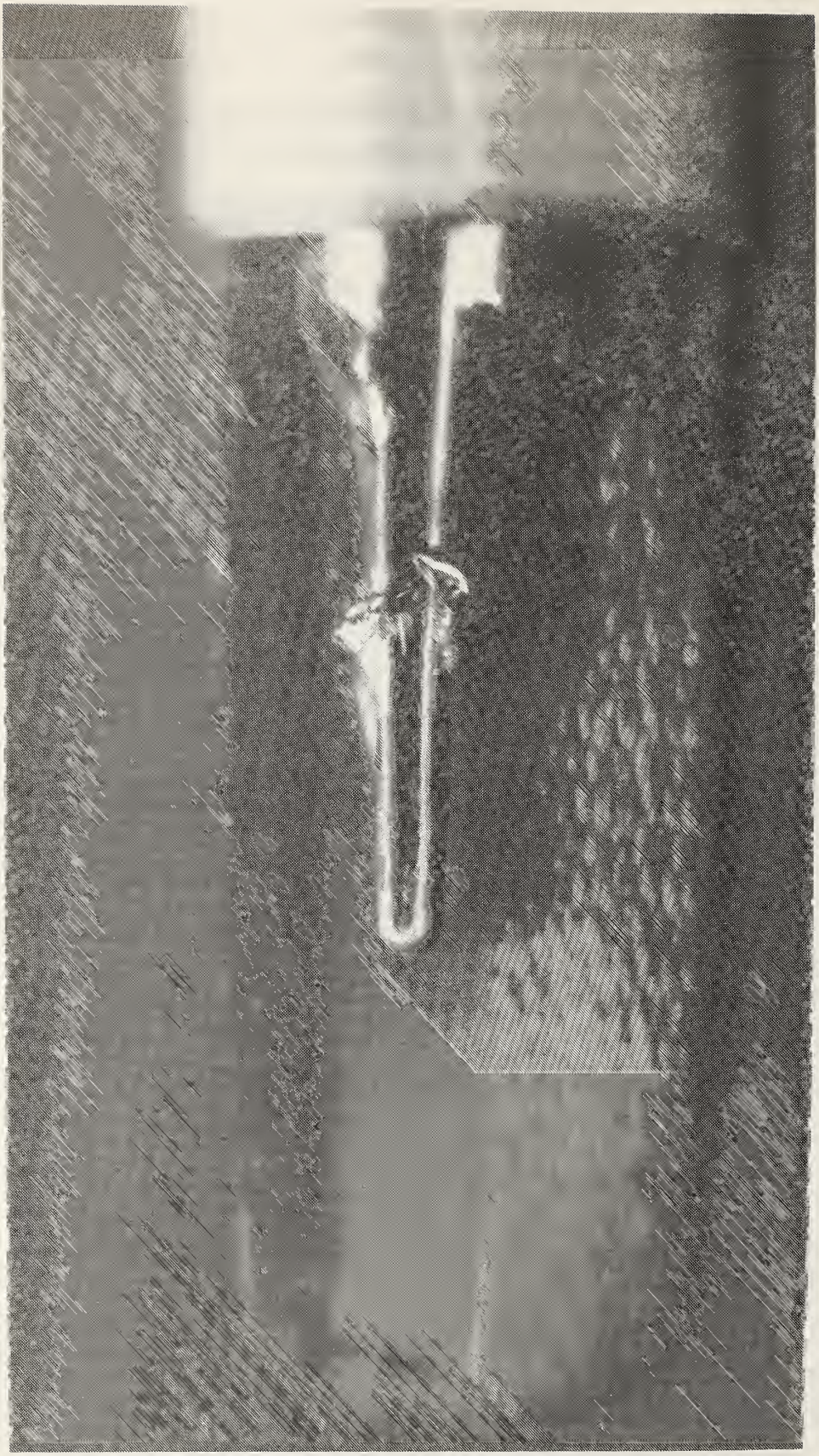

Fig. 15. Severe hair pin bend test.

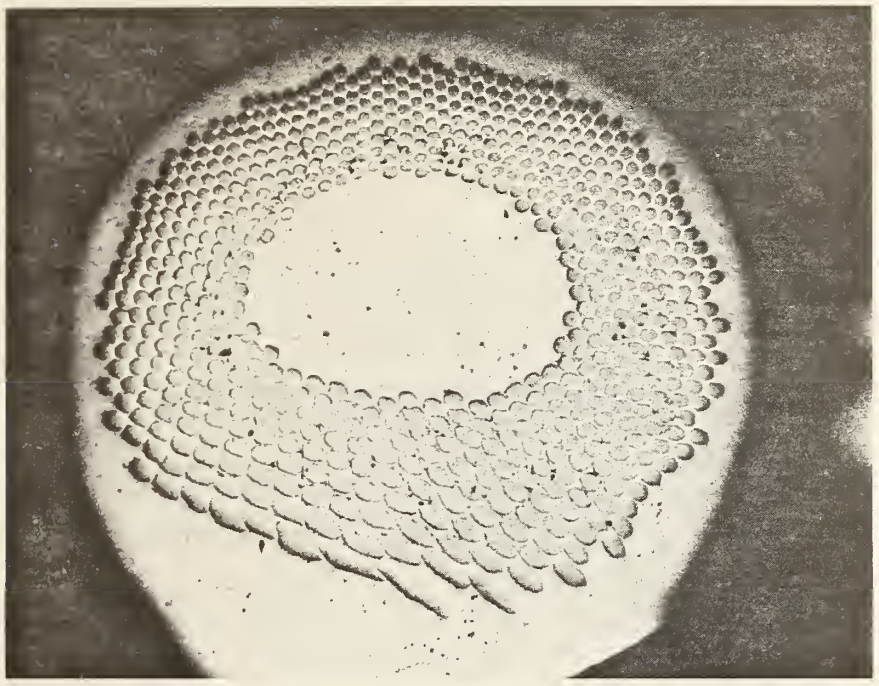

125X

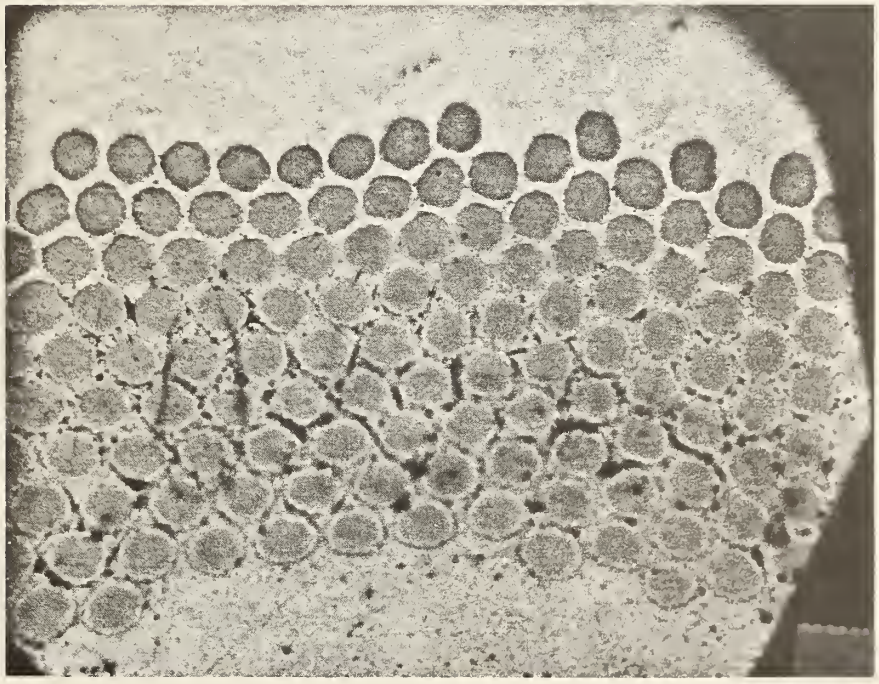

400X

Fig. 16. Cross section view of the bend section of the sample used in the severe hair pin bend test. The apparantly elongated filaments in the upper section of the picture are an artifact due to the cross section not being cut exactly at the middle of the bend section.

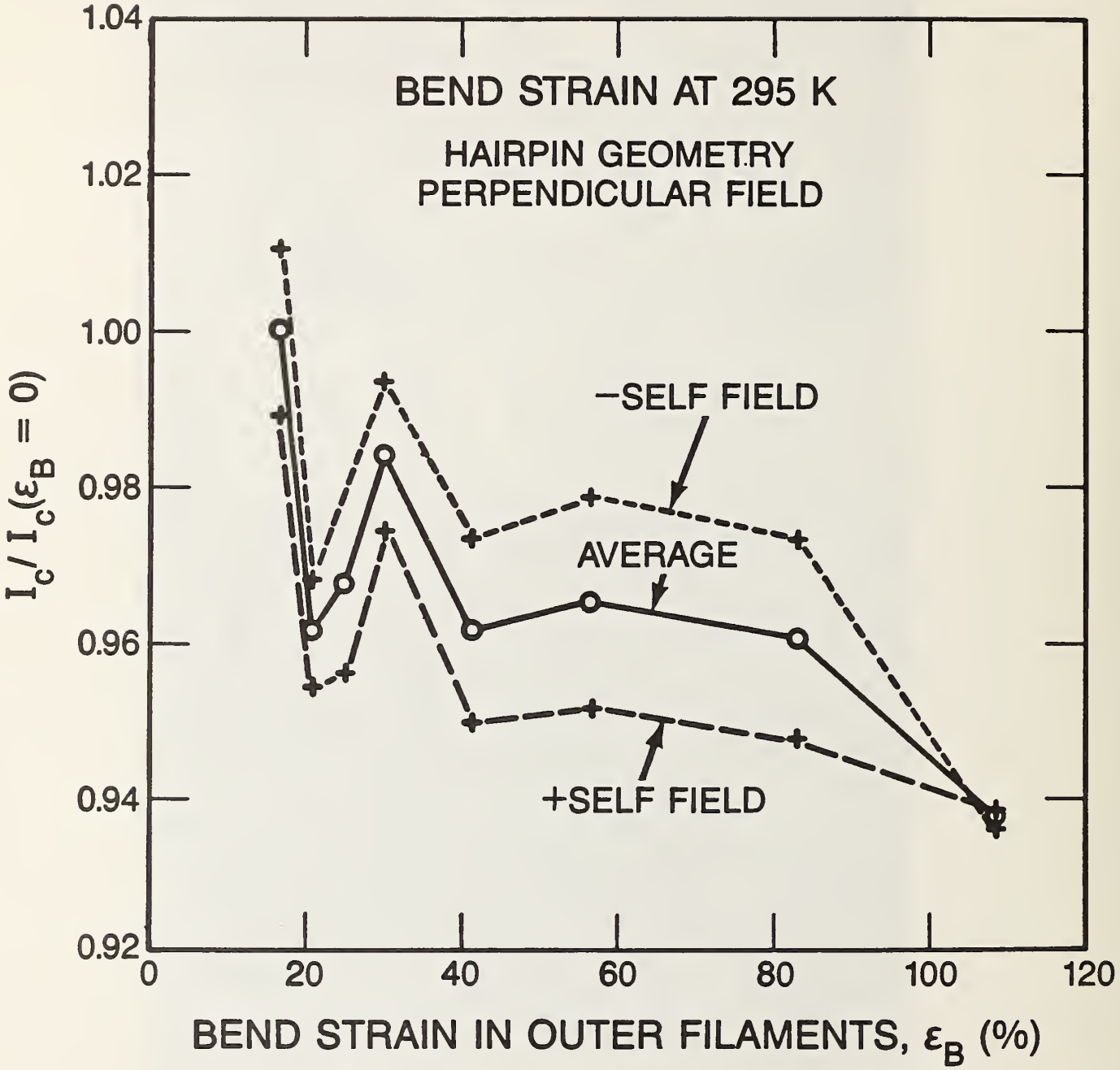

Fig. 17. Effect of room temperature bend strain on the critical current of NbTi Sample #5212 at 8 T. The abscissa is the calculated bending strain in the outermost filaments.

otherwise arise from the large difference in critical current between the legs of the hairpin and the bent section when the hairpin legs are parallel to applied magnetic field.

The sample was subjected to bending strain, starting at about 15% and increasing to a little over 100%. This was done progressively in the same sample by bending it at room temperature, cooling the sample to 4 K, measuring I_c, warming the sample to room temperture, bending the sample into a tighter radius, and repeating the whole process. The critical current was measured at each radius until the radius was reduced to nearly zero. A picture of the sample after being bent to a nearly zero radius is shown in Fig. 15 and a cross sectional view of the sample is shown in Fig. 16.

The I_c results corresponding to a 5μV/cm criterion are shown in Fig. 17. In this figure, the relative critical-current degradation is plotted as a function of bending strain in the outer filaments, ε_B. Critical current was measured for current flowing in both directions in the hairpin sample, one direction where the self field of the sample added to the background field (marked +) and the other where the self field subtracted from the background field (marked -). The average of the two critical-current values is plotted with open circles in Fig. 17.

The magnitude of the degradation at the high bending strains shown in Fig. 17 is small. The effect of room temperature bending strain on the critical current was about 4% at bending strains of over 100%, using a 5μV/cm criterion. All bending was done at room temperature, and there was no stress applied to the sample when it was cooled for the critical current measurement. Further bend tests need to be made, especially to measure the effect at lower electric fields.

CONCLUSION

Summarized below are the main results of these preliminary measurements of the critical-current degradation arising from different types of stress applied to the same NbTi starting material:

1. The magnitude of critical-current degradation from axial tensile stress applied at 4 K is about twice that from transverse compression at 4 K, when the results are compared in terms of stress applied to the NbTi filaments (excluding copper).

2. Both effects are about 98% reversible, indicating that the effects of stress in NbTi will be seen only when the conductor is under stress.

3. The effect appears to be a stress controlled, rather than a strain-controlled phenomenon. Even very high stress

accompanied by severe deformation (from transverse compression or axial tension at 4 K, or from bending strain at room temperature) produced little critical-current degradation ($\leq$ 1%) when the stress was removed. Annealing of NbTi, which reduces stress at constant strain also appears to increase the critical current.

4. The data indicate that a primary origin of the critical-current degradation in NbTi is a stress induced reversible decrease in the upper critical field. This is true for both transverse-compression and axial-tension degradation, as shown by the alrge relative increase in the magnitude of the critical-current degradation from both types of stress as the magnetic field approaches the upper-critical field.

These data are only preliminary. Additonal measurements will be needed to determine whether the effect is predominantly a very low temperature (~4 K) stress phenomenon or also arises from stress applied at higher temperatures. The consistency of the effects among different NbTi superconductors needs to be tested and further J_c-bend data is needed at lower electric fields.

ACKNOWLEDGEMENTS

The author gratefully acknowledges J. C. Brauch, C. A. Thompson, and D. L. Rule for their help with apparatus design and construction as well as data acquisition and reduction. Appreciation is also expressed to R. M. Scanlan, J. M. Royet, and C. Taylor (Lawrence Berkeley Laboratory) for discussions and supplying the samples. L. F. Goodrich and the other members of the Superconductor and Magnetic Measurements Group at NBS contributed a number of helpful discussions to this research. The manuscript was typed by R. A. Shenko and R. B. Goldfarb contributed many useful comments on the text. The high magnetic fields needed for part of this study were obtained using the magnet facilities of the Francis Bitter National Magnet Laboratory.

References

1. J. W. Ekin, F. R. Fickett, and A. F. Clark, "Effect of Stress on the Critical Current of NbTi Multifilamentary Composite Wire," Proc. Int'l. Cryog. Mat. Conf. (Aug. 1975), Adv. Cryog. Eng. 22, 449 (1977).

2. For a review, see J. W. Ekin, "Mechanical Properties and Strain Effects in Superconductors," in Superconducting Materials Science: Metallurgy, Fabrication, and Applications, edited by S. Foner and B. B. Schwartz, Plenum Press, New York, p. 455-510 (1981).

3. The effect of critical-current anisotropy introduced by room-temperature flattening has been studied by Garber, unpublished, and by L. F. Goodrich, W. P. Dube, E. S. Pittman, and A. F. Clark, Adv. Cryog. Eng. 32, 833 (1986).

4. J. W. Ekin, "Superconductors," Chapt. 13 in Materials at Low Temperatures, edited by R. P. Reed and A. F. Clark, American Soc. for Metals, p. 465-513 (1983).

5. J. W. Ekin, "Strain Scaling Law for Flux Pinning in Practical Superconductors, Part I: Basic Relationship and Application to Nb_3Sn Conductors," Cryogenics 20, 611-624 (1980).

III. STUDIES OF NbTi STRANDS EXTRACTED FROM CORELESS RUTHERFORD CABLES

by L. F. Goodrich, E. S. Pittman, and J. W. Ekin

A. SUMMARY

The electromechanical properties of NbTi strands extracted from coreless cables (Rutherford) were studied to clarify the relative effects of strand location and field angle on current degradation that occurs in cables that have been compacted into a keystone shape. Detailed critical-current measurements were made on two samples. One sample was from a cable that was commonly used for cable studies late in 1985 and early 1986. The other sample was from a cable that had been compacted more than usual. Measurements on the second sample were done in order to more clearly identify the degradation features. The two cable samples, which had been fabricated under controlled conditions, were provided by Lawrence Berkeley Laboratory. These are prototype cables for high energy physics applications. Specific factors that are addressed are the nature, location, and amount of degradation. This information is intended to lead to methods for reducing the amount of critical-current degradation in cable manufacture.

The critical-current measurements on both cables showed that the same region of the cable had the lowest critical current for the limiting case in a dipole magnet. The orientation of current and magnetic field that is the limiting case for a dipole magnet is with the magnetic field nearly parallel to the wide face of the cable and current orientation. The weak link of the cable strand occurred at the thin edge. For a typical cable, this portion, which only represents 5% of the total length of the cable, contributed about 55% of the total voltage. For the more degraded cable, this same 5% of the total length contributed about 95% of the total voltage. Decreasing amounts of I_c degradation were measured in the portion of the strand from, respectively, the corners of the thin edge, the thick edge of the cable, the corners of the thick edge, and the faces of the cable. Cabling can lead to very localized reductions in critical current and any improvements have to focus on the thin edge of the keystone. Conversely, any additional lowering of the thin-edge critical current will be directly reflected in the overall performance of the cable.

B. INTRODUCTION

These measurements of electromechanical properties of NbTi strands extracted from coreless cable were made to clarify the nature of critical-current degradation that occurs in cables that are compacted into a keystone shape. All the measurements reported here were made on two samples, denoted as Sample A (billet 5914, cable SC 305) and Sample B (billet 5212, cable SC 297). Sample A was a strand from a cable that was commonly used for cable studies late in 1985 and early 1986. Sample B was a strand from a cable that was re-rolled through the turkshead (to re-size it) after it had been cabled. This re-roll may have been done in the wrong direction, opposite the original cabling and roll direction. The re-rolled cable Sample B was a worst-case situation that was studied to more clearly identify the degradation features. The comparison of the results of measurements on these two cables indicated significant similarities and differences.

The critical current, I_c, of strands extracted from cables was measured as functions of position along the cable and magnetic field orientation. The two cables, which had been fabricated under controlled conditions, were pro-vided by Lawrence Berkeley Laboratory. These were prototype cables for high energy physics applications. Specific factors that were addressed were the location and field angle dependencies of the critical-current degradation.

Some of the conductor parameters are given in Table 1. Sample A had a Nb diffusion barrier on each of the 6006, 5 μm diameter filaments. Sample B did not have a diffusion barrier. The Sample A billet was double stacked; Sample B was single stack. The starting-wire critical currents (before the cabling process) were determined at 5 T and 4.02 K using a 0.1 μV/cm criterion. The critical-current density was calculated using the NbTi cross-sectional area, which was determined using the copper-to-superconductor volume ratio. The critical-current density at 4.22 K would be about 6% less than the values listed at 4.02 K. The starting wire I_c's were measured in another magnet as another part of this program; thus their values might be shifted by a few percent relative to the measurements on the cable strands. For Sample B, see Table 5 in section II D for starting strand material critical current.

Some of this work was originally presented at the 5th Workshop on NbTi Superconductor (March 25-27, 1986, Menlo Park, CA). Discussions at this workshop are acknowledged, especially with R. M. Scanlan and J. M. Royet (Lawrence Berkeley Laboratory). Information on the cable fabrication and current density using highly homogeneous NbTi alloy can be found in References 1 and 2.

C. EXPERIMENTAL DETAILS

This is a discussion of sample preparation, notation, data acquisition, and data analysis. The samples were from 30 strand cables and started as 0.65 mm diameter round wires with a right hand filament twist of about 0.8 twist/cm. The cable had a left hand lay with a 69 mm pitch and a cable width of 9.7 mm, mid-thickness of 1.17 mm, and a keystone angle of about 1.24°.

The critical current measurements reported here were made using a straight sample geometry and a radial access, split pair magnet. The orientation of the sample was changed by rotating the sample cryostat relative to the background magnet. The zero angle was defined as the orientation with the magnetic field parallel to the wide face of the conductor (see Fig. 1). The critical current was defined as the current at which the electric field strength was 0.1 μV/cm. This corresponds to a voltage of only 20 nV between the taps with the smallest separation. A number of repeated determinations of I_c were made at 0° to give an indication of measurement precision. The precision was about ±1% and the accuracy was about ±2%.

A number of voltage taps were placed along the length of the strand to determine its local electrical properties after it had been deformed by the cabling process. Three regions of the cable were studied: the thin edge, the face (top or bottom), and the thick edge. Each of these regions was divided with voltage taps into three approximately equal-length, adjacent segments. The three segments of each cable edge were denoted as the central flat edge and the two corners. These edge voltage taps had separations of 2 to 2.5 mm (thin edge) and 2.5 to 3 mm (thick edge). The voltage taps along the face of

Table 1. Conductor Parameters

Sample	Billet No	Cable No	# Filaments	Filament Diameter	Cu/sc	Starting Wire I_c(5 T) at 0.1 μV/cm and 4.0 K	Starting Wire J_c(5 T) J_c using NbTi area
A	5914	SC305	6,006	5 μm	1.64	320A	2500 A/mm^2
B	5212	SC297	648	16 μm	1.77	347A	2900 A/mm^2

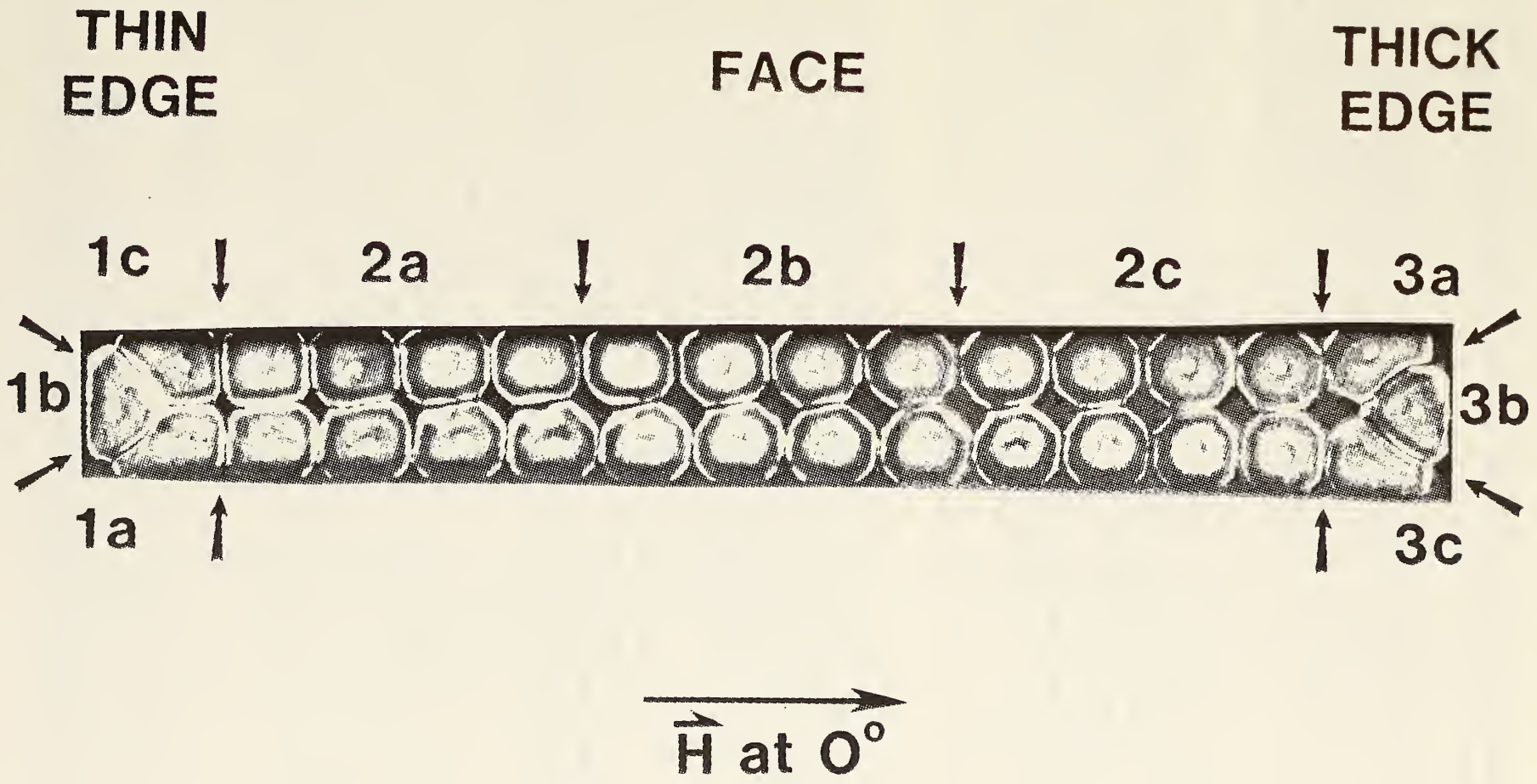

Figure 1. Photograph of Sample A cable cross section with voltage taps and magnetic field angle identified.

the cable had separations of about 9 mm and they did not include any of the cable corner regions.

The voltage tap notation used in this report was a combination of numbers and letters to denote the various portions of the cable strand (see Fig. 1). The numbers 1, 2, and 3 refer, respectively, to the three regions of the cable, starting with the thin edge (1), then the face (2), and finally the thick edge (3). Within each of these regions, the three segments were denoted with the letters a, b, and c. Thus, as shown in Fig. 1, the sequence along the strand was 1a, 1b, 1c, 2a, 2b, 2c, 3a, 3b, and 3c.

Voltage taps on the sample were made using three flat quads (miniature four-conductor flat cable) of #32 gauge wires. Within each quad, three adjacent segments could be measured with a minimum of induced voltage. The end taps of adjacent quads were common to allow complete coverage of the sample. The quads of voltage taps were soldered to twisted pairs near the bottom of the sample cryostat and immersed in liquid helium during data acquisition. The twisted pairs were continuous from the bottom of the cryostat to the voltmeter input cables to avoid thermally reduced voltages. The junctions at room temperature between the voltage tap leads and the nanovoltmeter input leads were maintained isothermal by putting small bags of lead shot under and on top of the junction.

The sample holder was a 1/2" diameter 316 stainless steel rod with a groove machined along its length that was wider than the cable. The walls of this groove were insulated with a thin layer of epoxy formed with a TFE impressioner. After the voltage taps were soldered to the sample, a second layer of epoxy was used to hold the sample in the rod. The ends of the sample extended past the end of the rod and were used for the current contacts.

The field-angle rotations were done slightly above atmospheric pressure (about 4.02 K). Measurements were made at 5 and 8 T. Some data at 0 and 90° were taken at other magnetic fields from 4 to 9 T. Additional data were taken at a higher temperature (about 4.24 K) for magnetic fields from 4 to 9 T. This allowed comparisons with other measurements and this was used to determine the temperature dependence of different segments of the strand.

Three voltage signals and current-versus-time were simultaneously acquired on a digital processing and storage oscilloscope. The acquisition time for each set of curves was about 51 seconds. The current waveform consisted of an initial zero current baseline, a fast current ramp up, a slow ramp toward I_c, and then (if the sample did not quench) a slow ramp down, followed by a fast ramp down and a final zero-current baseline. If the sample quenched before the current ramp was reversed, the rest of the waveform was at zero current after the quench detector had reset the current supply. For most of the measurements the current was increased until the sample quenched. This was done in order to get as high a current and voltage as possible, since some portions of the strand had a higher I_c than others and the sample could quench before very much voltage could be developed on some voltage taps. The raw waveforms were stored for later analysis.

During data analysis, the effects of voltage offsets, changes in thermoelectric voltage, inductive voltage, and current transfer voltage were determined and the waveforms corrected. The voltage offsets and changes in

thermoelectric voltage were determined using the initial and final zero current baselines of the waveforms. The thermoelectric voltage correction was made assuming a constant drift with time. This correction was generally only a few nV/cm. The inductive voltage (voltage proportional to dI/dt) and current-transfer voltages were determined using the fast and slow ramp portions of the waveforms well below the critical current. The current-transfer voltage may or may not be intrinsic to the wire since only a 64 mm length of the sample was in full magnetic field. There is a further discussion of current tranfer later in this report. Generally the amount of current transfer voltage was quite small.

It was useful to consider what the effective critical current of one strand pitch length would be. The effective critical current was defined as the critical current determined by adding up the voltage contributions of each strand segment, taking into account that the portions along the face need to be counted twice for one pitch length. This total voltage was then converted to an effective electric field by dividing by one pitch length. This was useful because it related more directly to measurements made on the whole cable where several pitch lengths were included between the voltage taps.

D. RESULTS

The data presented here are preliminary in that they may not represent averages of a number of specimens. There is no reason to believe, however, that these two specimens were not typical. Independent measurements on the cables [3] indicated that Sample A was degraded by about 9% and had a field anisotropy of about 11% and Sample B was degraded by 22% and had an anisotropy of -11%. See Reference 4 for definitions of degradation and anisotropy. These results are consistent with those presented here. The additional data presented here on the nature, location, and amount of degradation is intended to lead to methods for reducing the degradation.

Photographs of the two cable samples with voltage tap pairs indicated are shown in Figs. 1 and 2. The voltage taps along a strand are represented here on the cable cross section. Along its length, the individual strand goes through all positions shown in the cable cross section. The tap notation was defined in the Experimental section. Notice the strand cross section for each position and the tap notation.

In the first run of Sample B, the thin edge had the lowest critical current, and this region was limiting the current. For the second run a short section of the thin edge was shunted with a 0.7 cm length of another cable strand. This allowed the current to get slightly higher and enabled testing of the other regions of the strand before the sample quenched. The data presented for Sample B are a combination of these two runs, not-shunted and shunted.

Position dependence

The critical current as a function of position along the strand at 0° and 90° field angle is given in Figs 3 and 4 for Sample A. The critical current values varied by as much as 27% from the highest at 0° and 11% at 90°. At 0° the central flat portion of the thin edge had the lowest I_c. The central flat

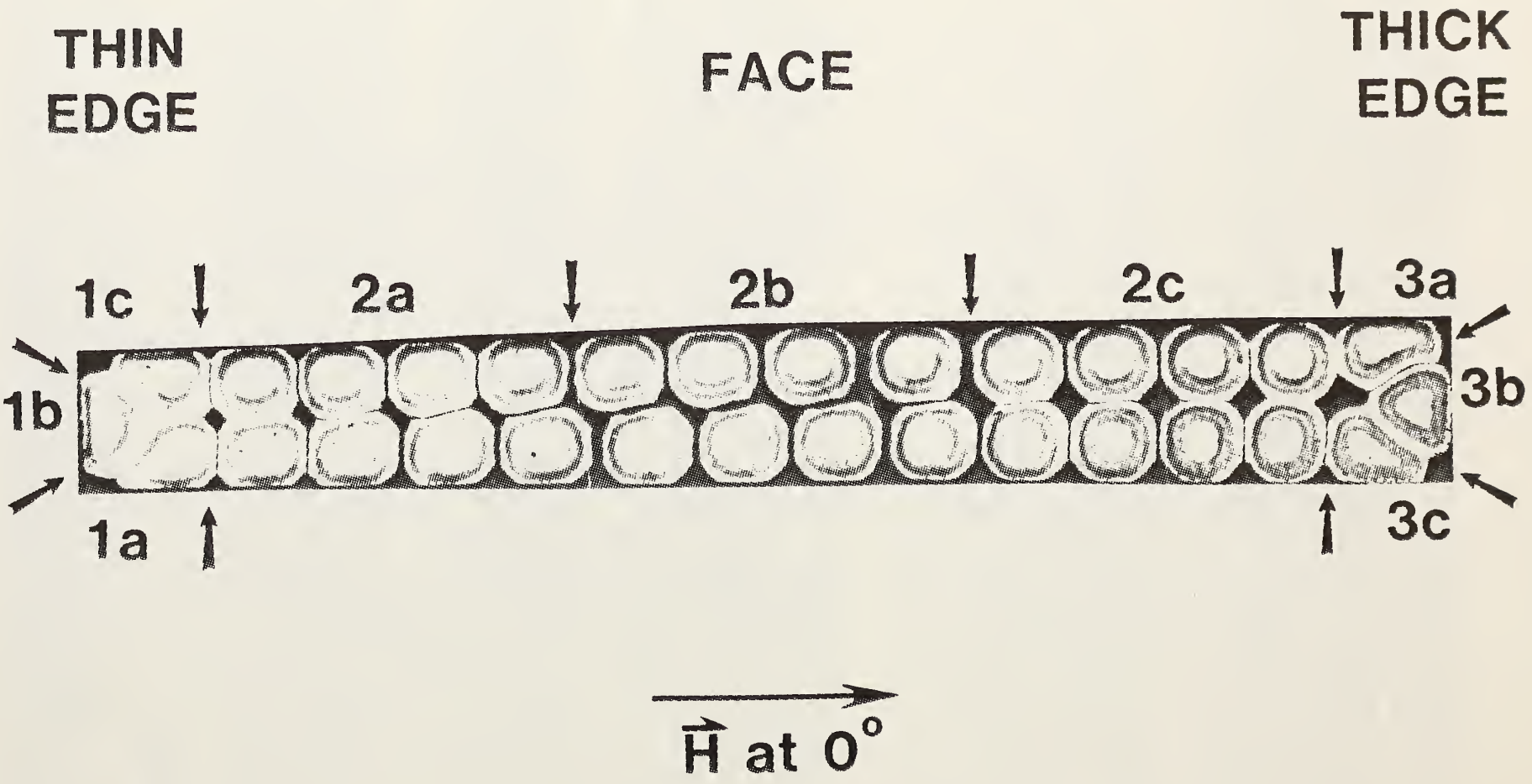

Figure 2. Photograph of Sample B cable cross section with voltage taps and magnetic field angle identified.

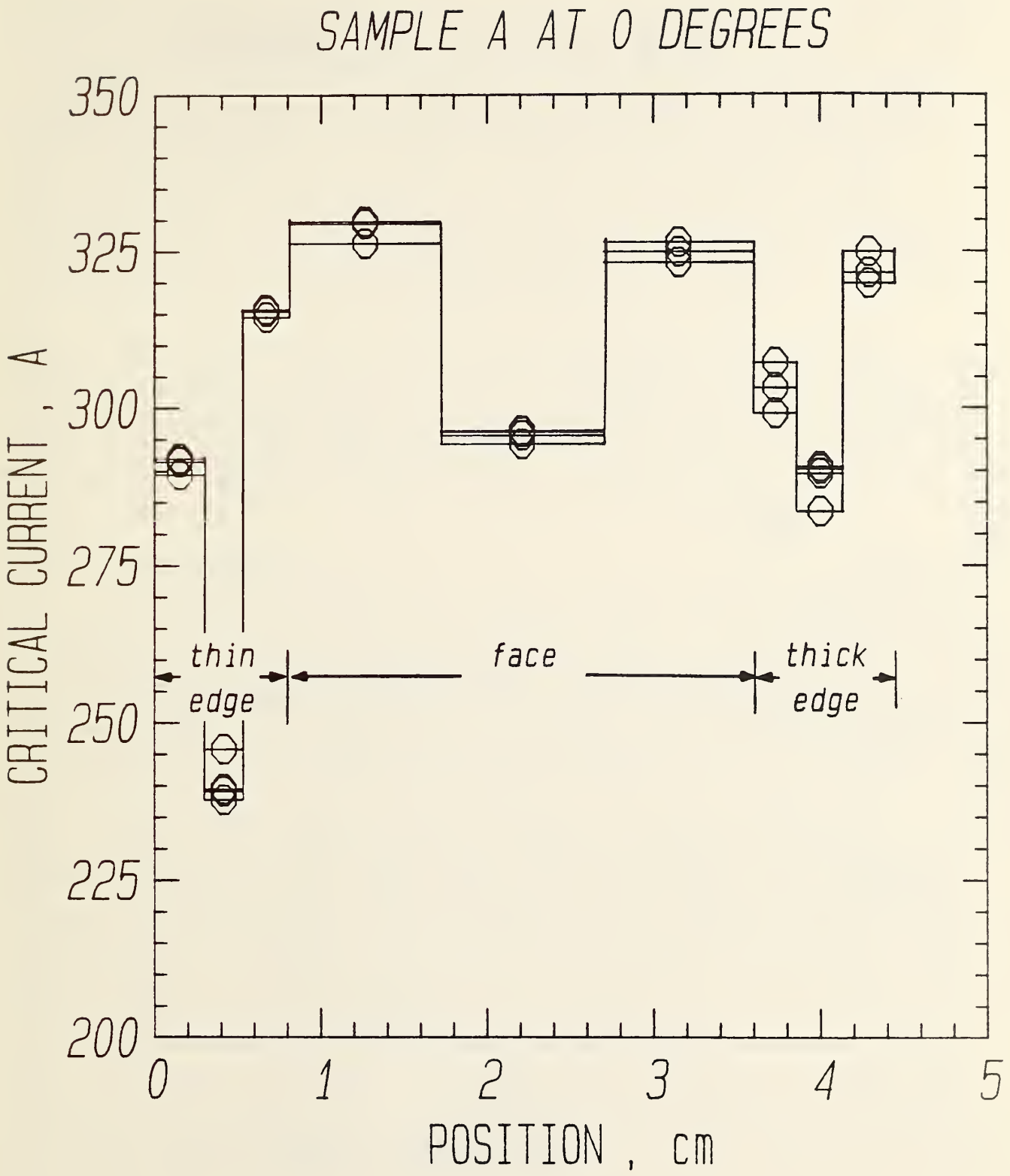

Figure 3. Sample A, critical current versus position at 0°.

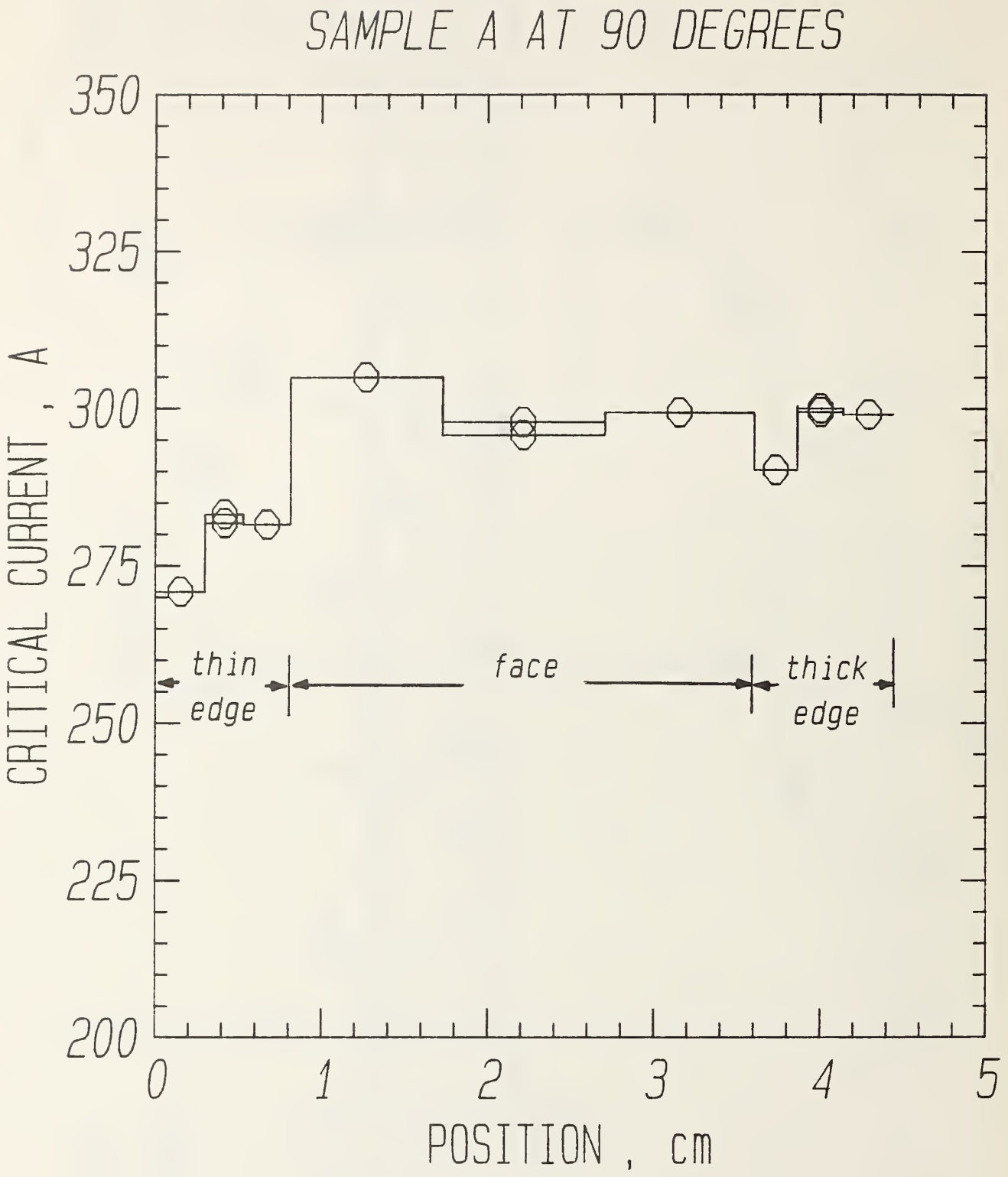

Figure 4. Sample A, critical current versus position at 90°.

portion of the thick edge was less degraded. The corners of both edges had a higher I_c and had some asymmetry in the same cable lay direction. This may be due to mass flow away from the cable edge during the cable fabrication. The difference between 0 and 90° is due to the effect of the conductor aspect ratio [5] and the fact that the applied magnetic field is not exactly perpendicular to the current for all portions of the strand at all angles. The cable pitch is about 17°, which would increase I_c at 0° by about 8% [6] for the portions across the cable face. At 90° the applied magnetic field is perpendicular to the cable face, but it is not perpendicular to portions of the cable edges. The major deformation direction for the cable edge is 90° from that for the cable face. The edges have their lowest I_c at 0°. The central region of the cable face does not have very much change in I_c between 0 and 90° because the strand is almost round there.

The critical current as a function of position at 0° and 90° for the Sample B is given in Figs 5 and 6. The critical current values varied by as much as 35% from the highest at 0° and 33% at 90°. At 0° the central flat of the thin edge had the lowest I_c, and unlike Sample A, it did not increase very much at 90°. For both samples the difference between the thin and thick edges were similiar, as were the corner values. The central flat of the thin edge is the weak link and would appear to have a degraded I_c rather than a large aspect ratio effect.

Field angle dependence

The biggest difference in I_c's along the strand occurs with the magnetic field at 0° (parallel to the wide face of the cable). This is unfortunately near the orientation that is most critical for a dipole magnet. The orientation at the midplane of the magnet is 90° but the magnetic field is lower there than at the poles. Therefore, the limiting case is expected to be at the poles for both the inner and outer windings. The actual orientation of the cable and magnetic field at the pole is between 0° and 15° (for both windings) but, as shown below, the values at 0 and 15° are about the same.

Critical current as a function of angle for each tap on Sample A is shown in Figs 7, 8, and 9. These I_c's were determined using an electric field strength criterion of 0.1 μV/cm. These curves are smooth to within the precision of the measurement. There is some asymmetry between the positive and negative angles that may be due to which side of the strand the self field and applied field are adding or a bias put in by the cable lay direction. There is some structure in the plots at 45° which represents a cross over or compromise between the 0 and 90° character. The values at 0 and 90° show most of the information and are concentrated on in what follows.

The critical current as a function of angle for each tap on Sample B is shown in Figs 10, 11, and 12. The biggest difference between the two samples is that the I_c of Sample B at the thin edge was lower and did not increase at 90°. The higher values of I_c in these plots have a larger uncertainty because they were at or near the quench current.

Electric field profiles

The electric field profile along Sample A near the quench current is shown in Figs. 13 (at 0°) and 14 (at 90°). The value of maximum E was defined

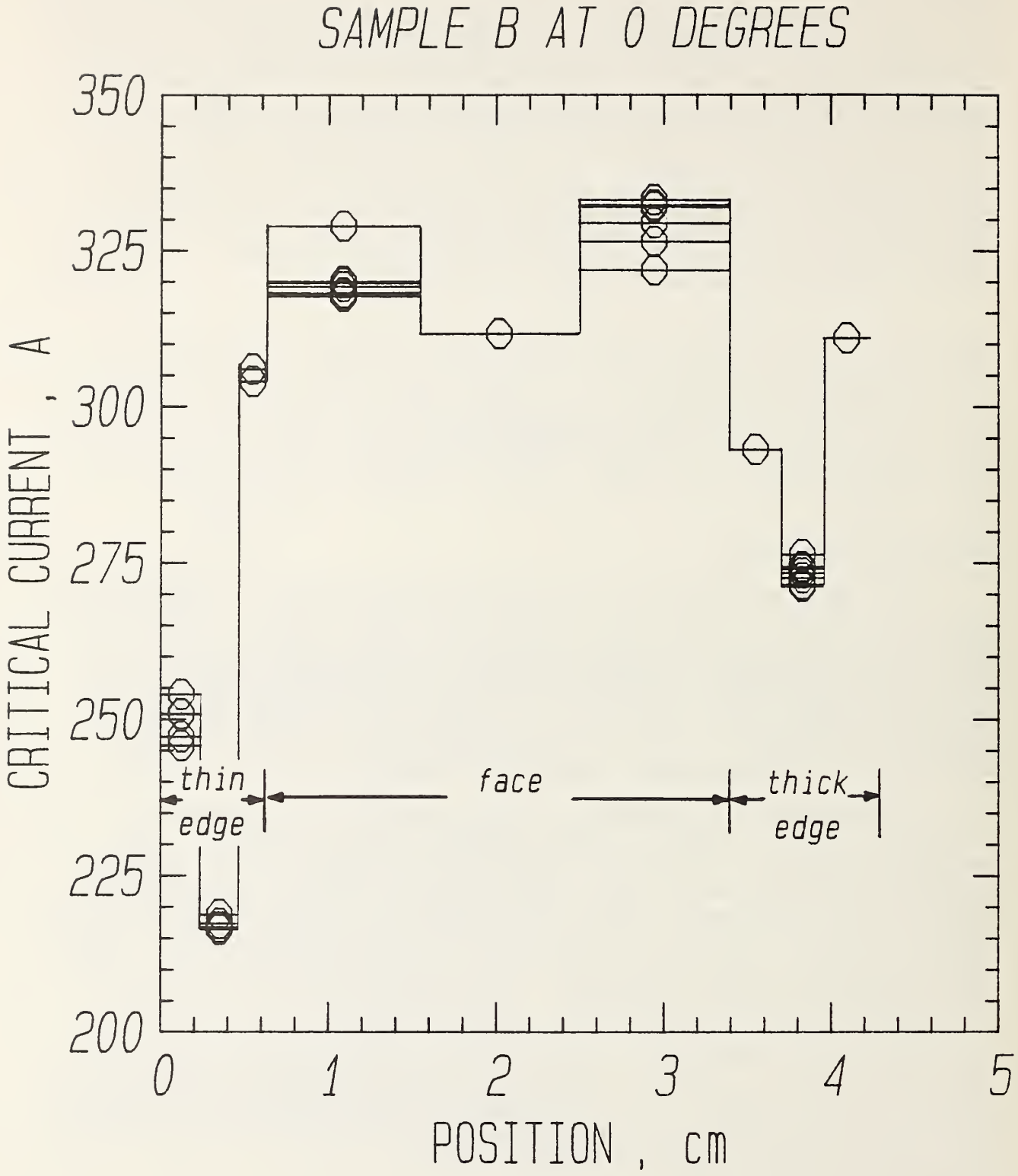

Figure 5. Sample B, critical current versus position at 0°.

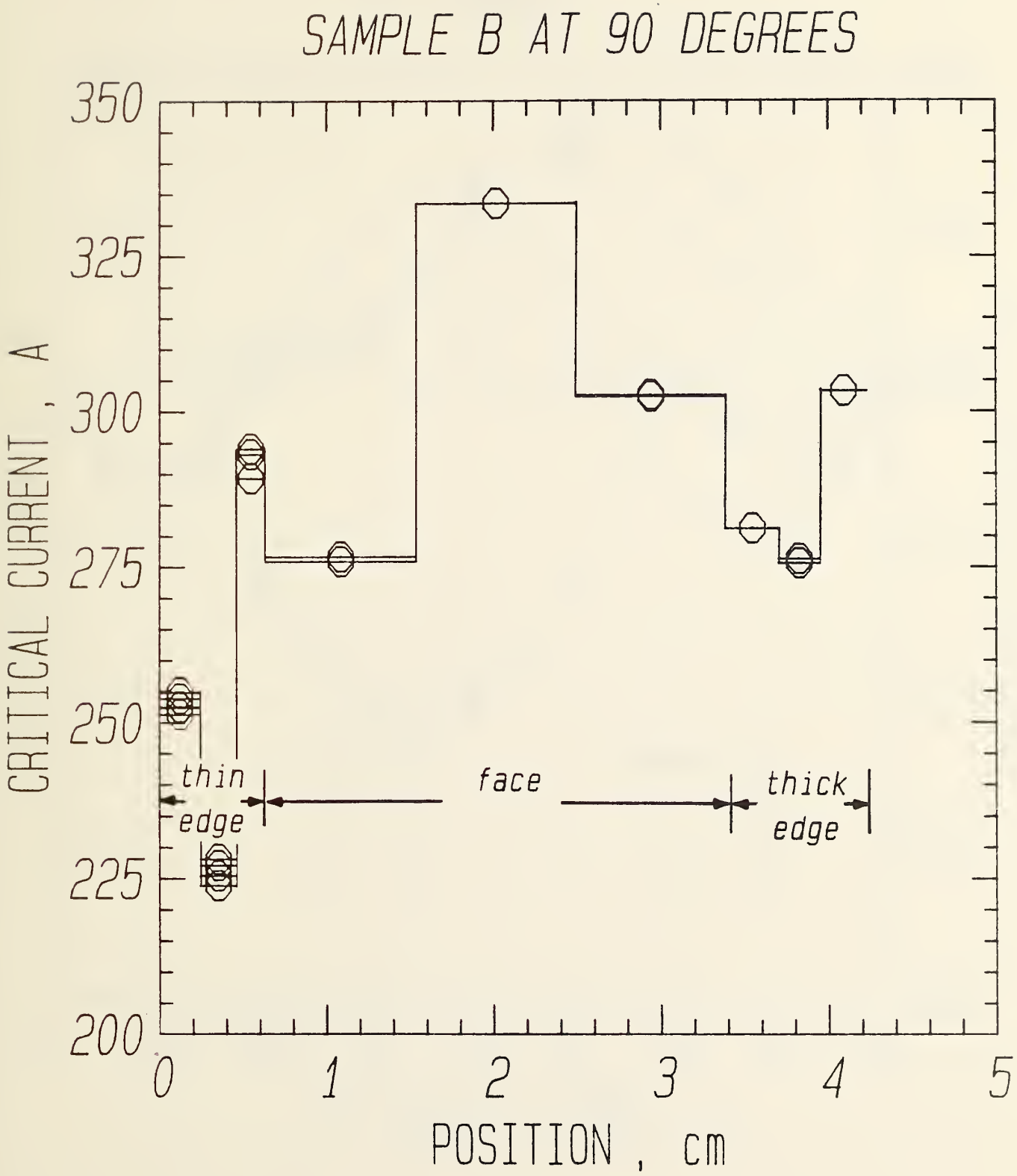

Figure 6. Sample B, critical current versus position at 90°.

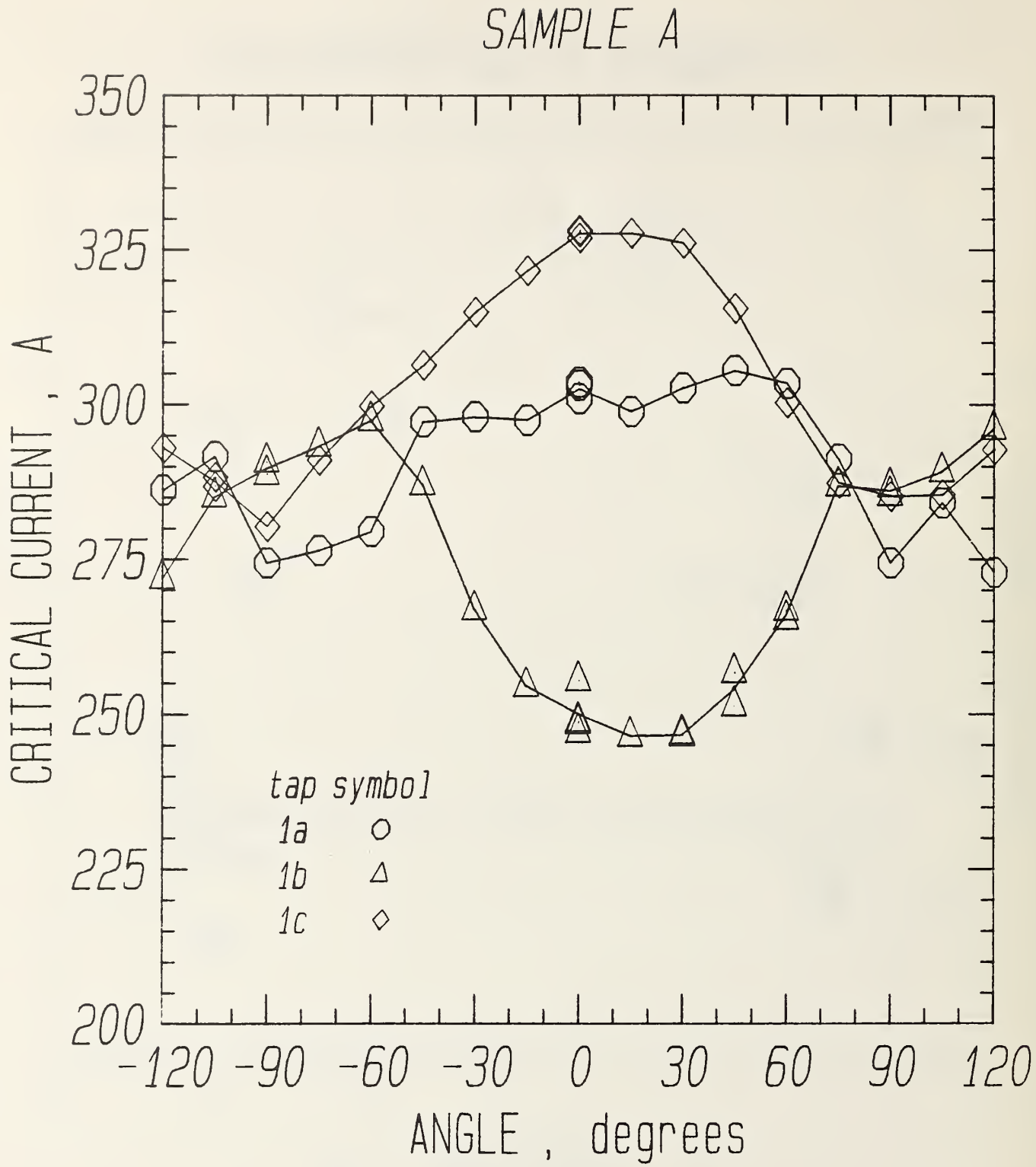

Figure 7. Sample A, critical current versus angle for thin edge taps.

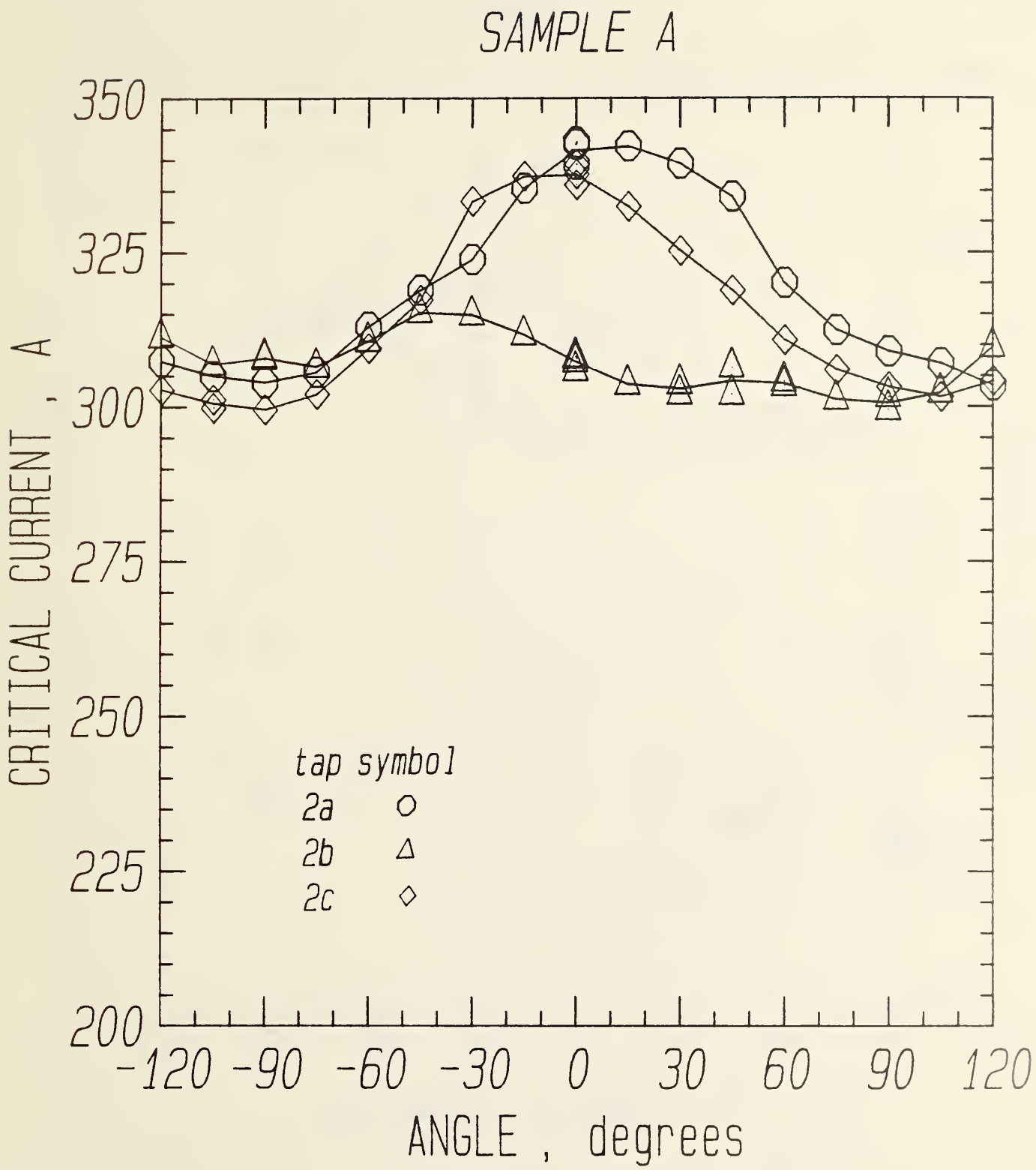

Figure 8. Sample A, critical current versus angle for cable face taps.

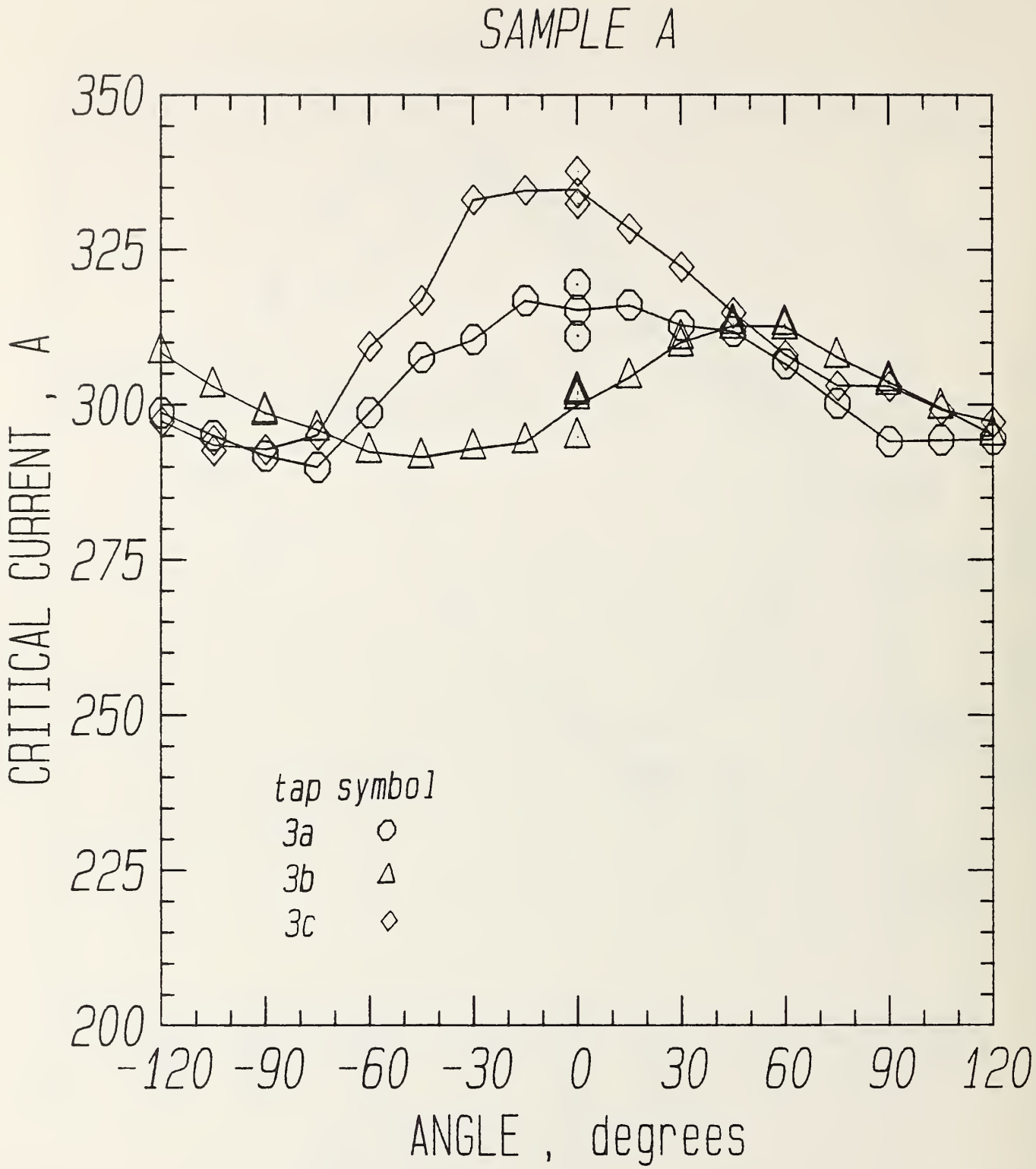

Figure 9. Sample A, critical current versus angle for thick edge taps.

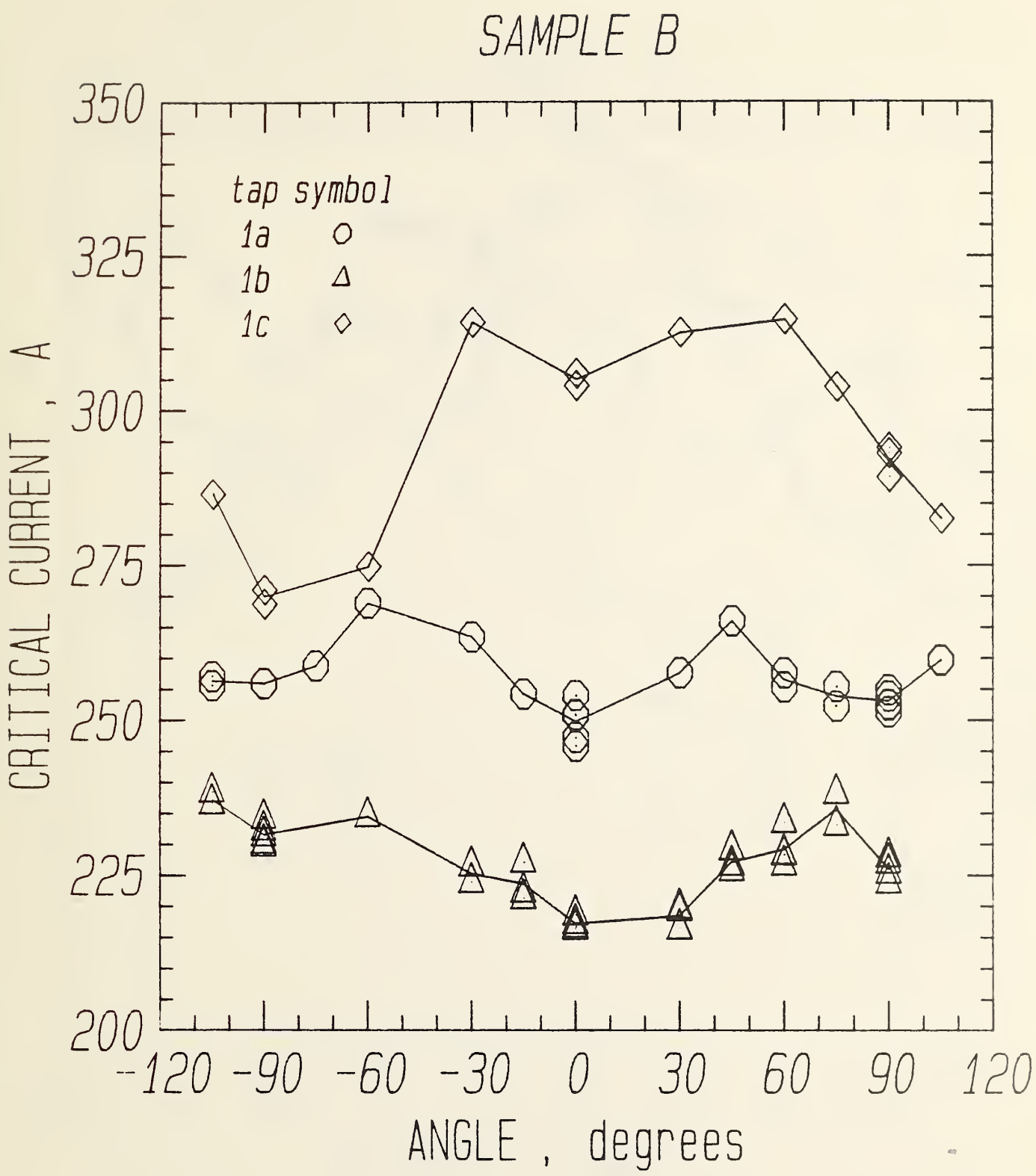

Figure 10. Sample B, critical current versus angle for thin edge taps.

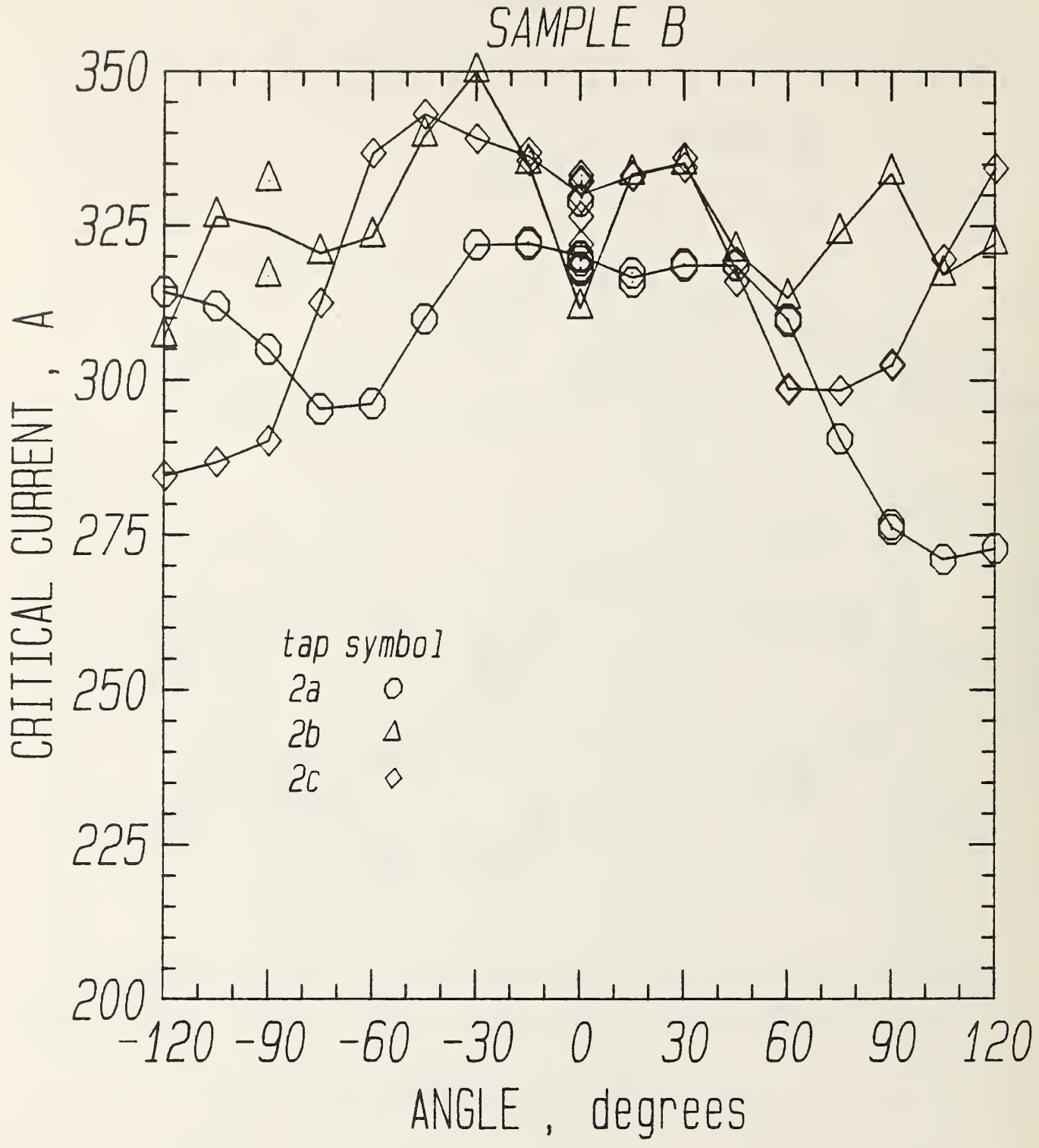

Figure 11. Sample B, critical current versus angle for cable face taps.

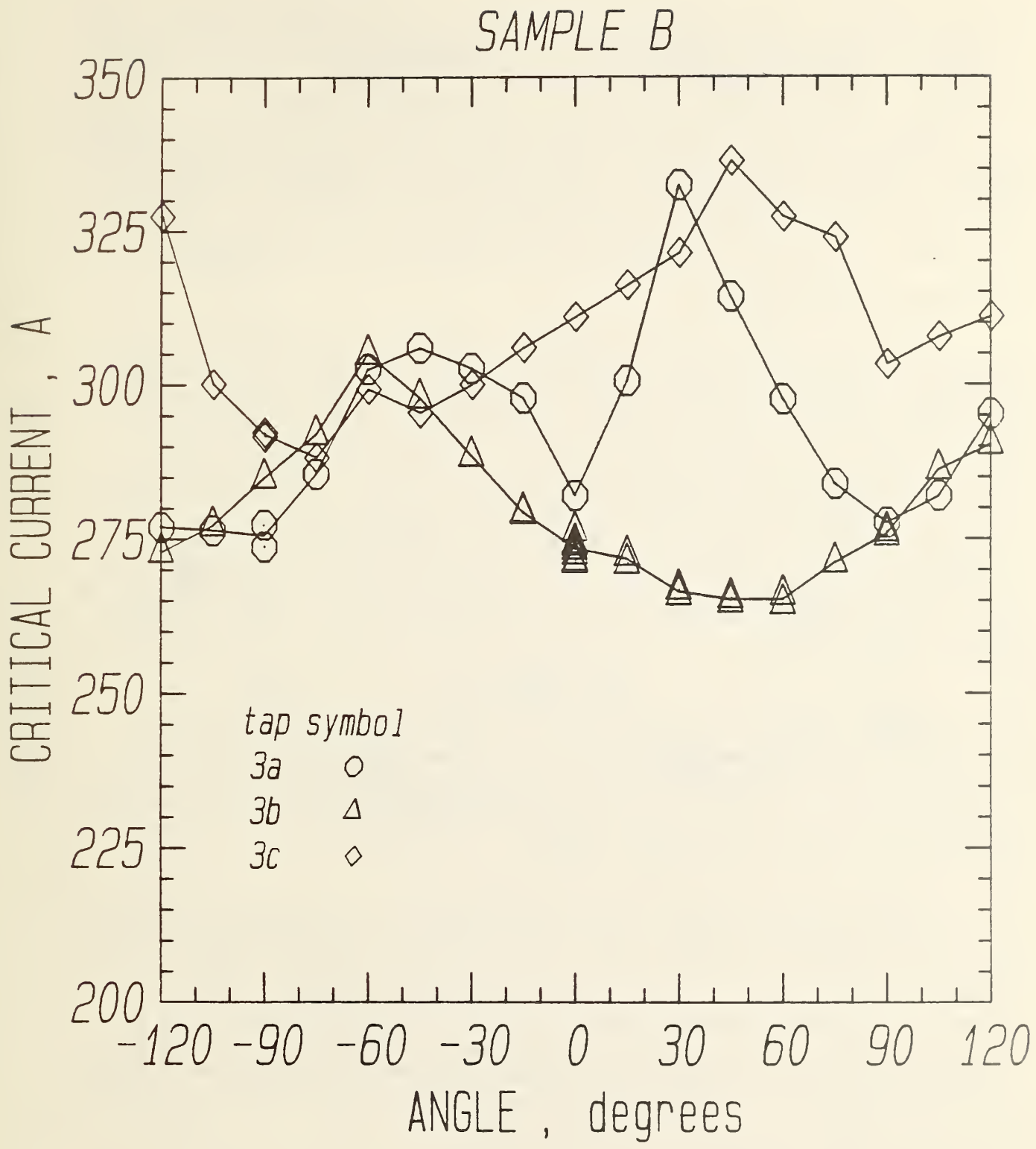

Figure 12. Sample B, critical current versus angle for thick edge taps.

as the electric field a few tenths of a second before thermal runaway started. Slight changes in quench current for the different observations causes large changes in the electric field even in logarithmic space. At 0°, the flat portion of the thin edge is clearly the weak link and the asymmetry of the corners is still present. The profile at 90° is more uniform.

The electric field profile along Sample B just before quench is shown in Figs. 15 (at 0°) and 16 (at 90°). The profile for this sample is much more nonuniform than for Sample A. The center of the thin edge is more clearly the weak link. The points with values of E below 0.01 μV/cm in Fig. 15 were assigned a value of 0.01 μV/cm in order to keep the plot scale relevant.

Effective critical current

A relevant question at this point is: What is the effective critical current of these strands as a function of angle? One possibility is the current at which the average (see the Experimental section) electric field strength is equal to some criterion. The effective critical current and quench current for Sample A are plotted as a function of angle in Fig. 17. The effective critical current at various electric field criteria had an angular dependence very similar to the quench current. This was not expected considering that the quench current should be strongly dominated by the degraded section (or weak link) of the strand. This was not the case, which suggests that the average E does give a relevant critical current. The end cooling around the weak link must have been sufficient that the local heating did not have an adverse effect on I_c. The weak link at 0°, tap 1b, contributed about 55% of the total voltage even though it only represented 5% of the total length.

The effective critical currents and quench current for Sample B are plotted as a function of angle in Fig. 18. There are two curves without symbols. The upper was the quench current after a shunt was placed on the thin edge. The lower was the quench current before the shunt was placed on the thin edge. The lowest curve is the effective I_c at 0.1 μV/cm. The weak link at 0°, tap 1b, contributed about 95% of the total voltage even though it represented only 5% of the total length.

Table 2 shows the percentage differences of the I_c's from the starting wire (before cabling) values. The starting wire I_c's are approximate because they were measured as another part of this program in another magnet. Notice that the additional lowering of the weak-link I_c for Sample B resulted in a much lower effective I_c. In fact, the difference in effective I_c's was greater than the difference in weak link I_c's at 0.1 μV/cm. At 0°, I_c of Sample B was an additional 12% lower than that of Sample A but the effective I_c was 20% lower. The difference in I_c's at higher electric fields, however, was more than 12%. This increased effect may show that the local heating had an adverse effect on I_c for Sample B.

Current-transfer voltages

The current-transfer correction as a function of position for Sample A at 0 and 90° respectively are plotted in Figs. 19 and 20. These electric fields correspond to very small voltages. The small negative values for some positions may be a real, but slight, voltage projection phenomenon [7]. This

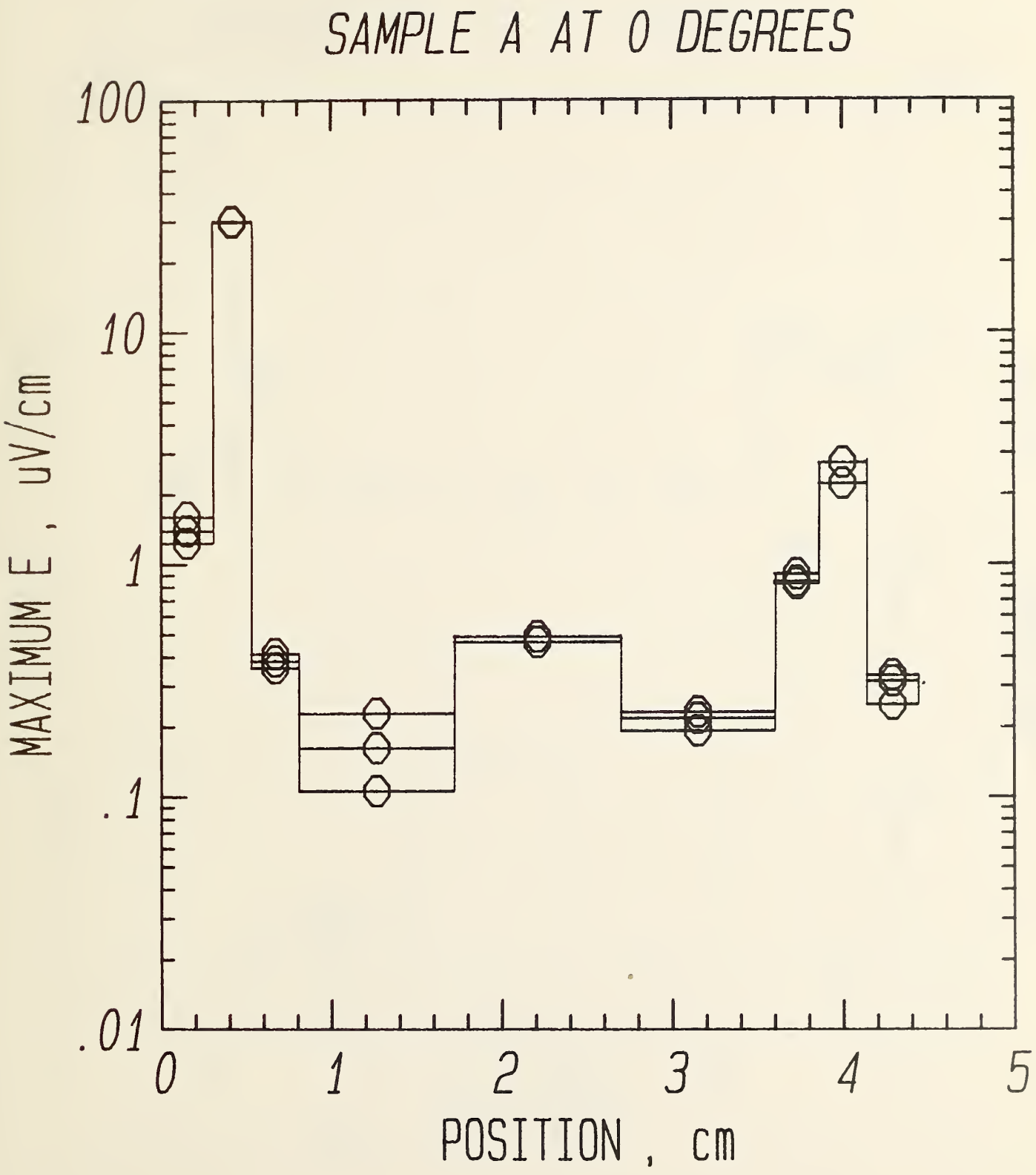

Figure 13. Sample A, maximum electric field versus position at 0°.

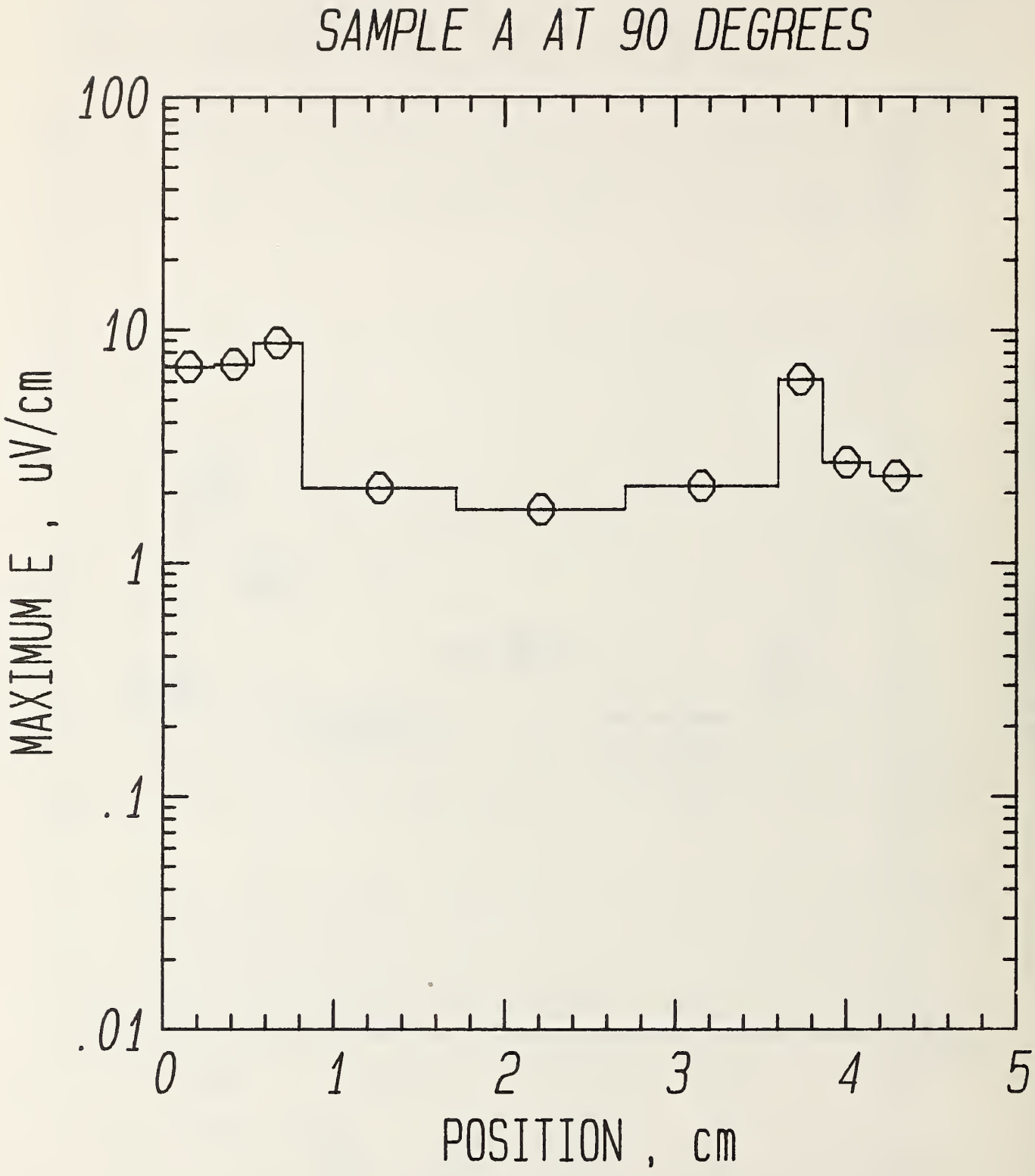

Figure 14. Sample A, maximum electric field versus position at 90°.

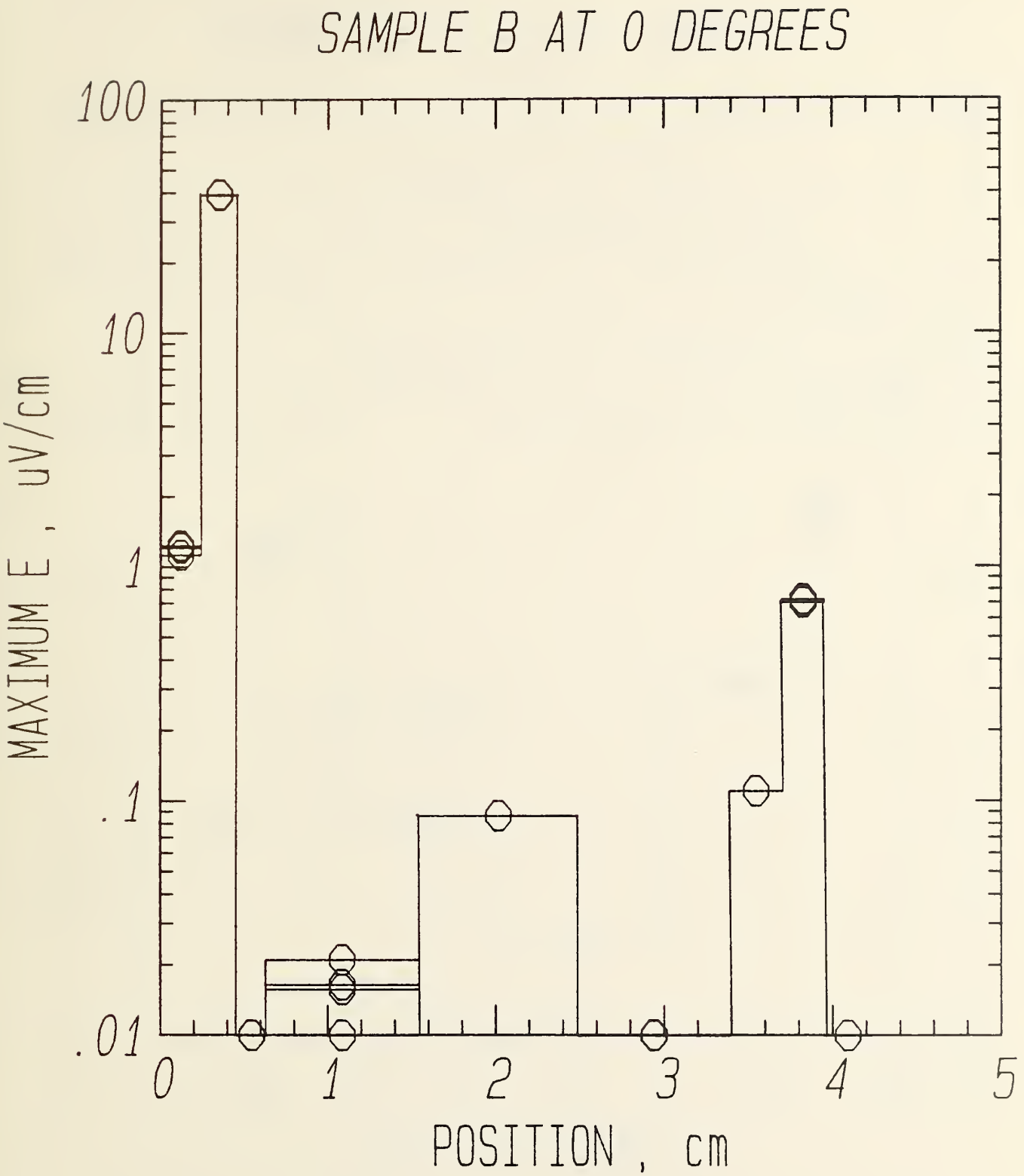

Figure 15. Sample B, maximum electric field versus position at 0°.

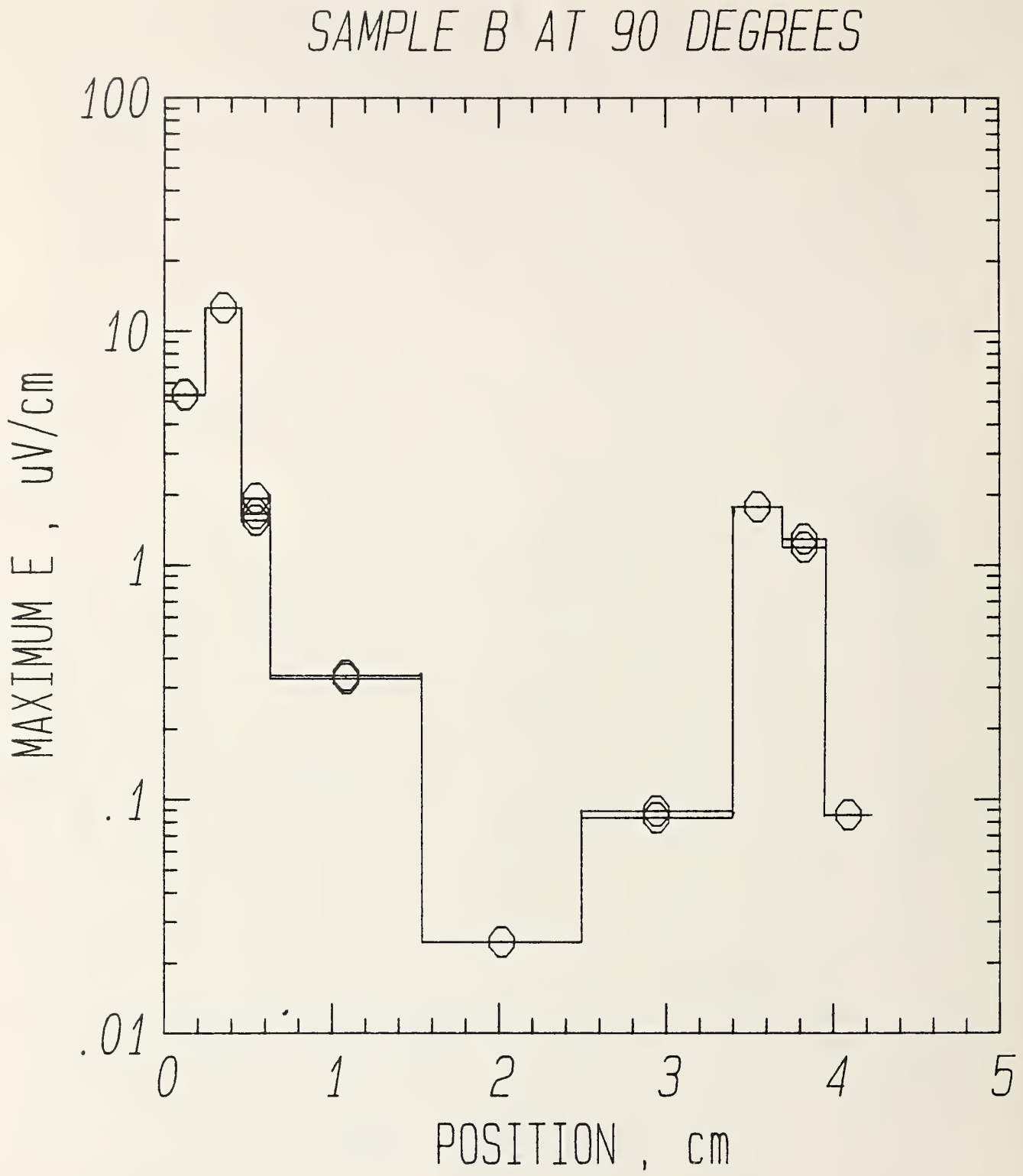

Figure 16. Sample B, maximum electric field versus position at 90°.

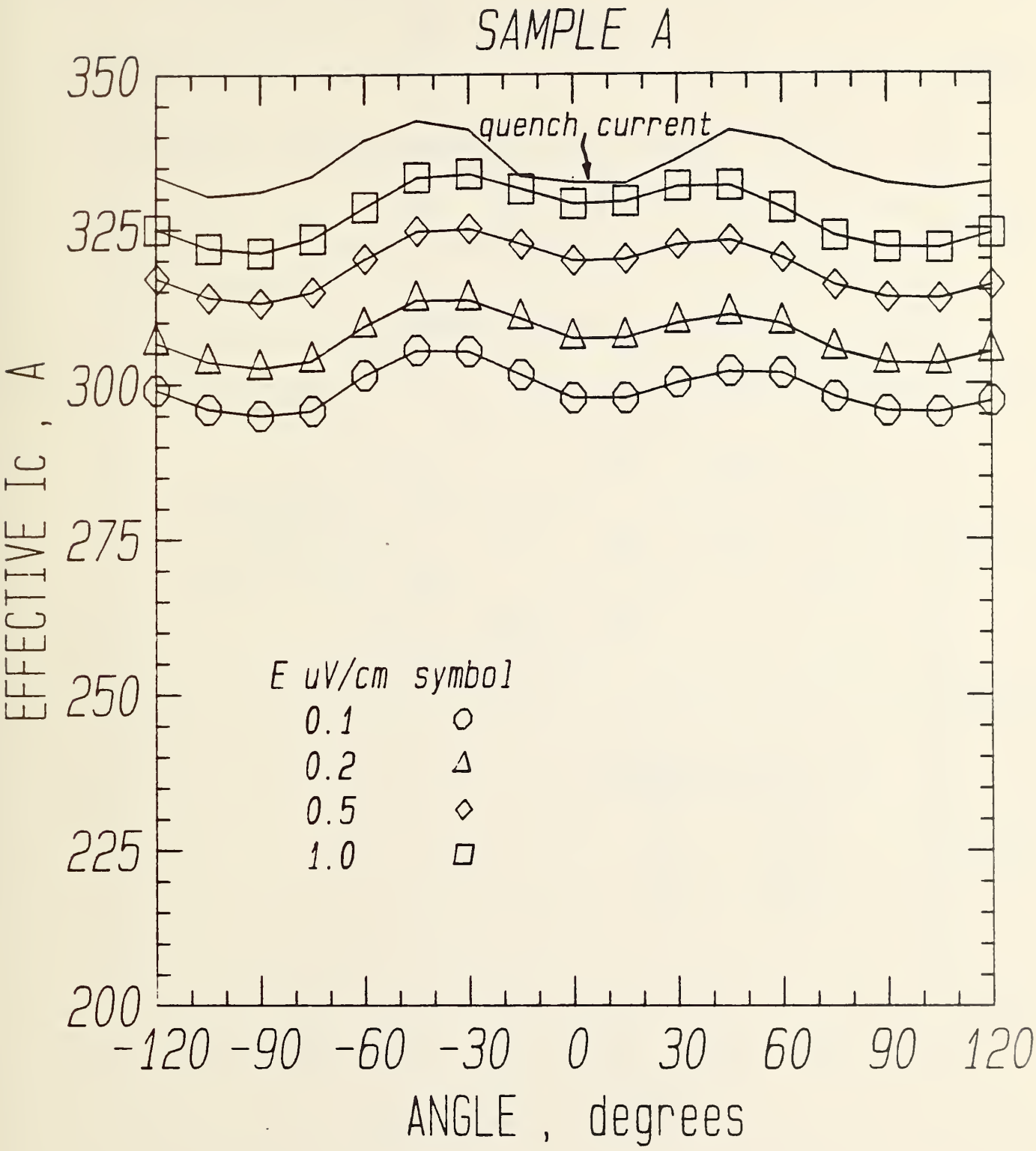

Figure 17. Sample A, effective critical current and quench current versus angle.

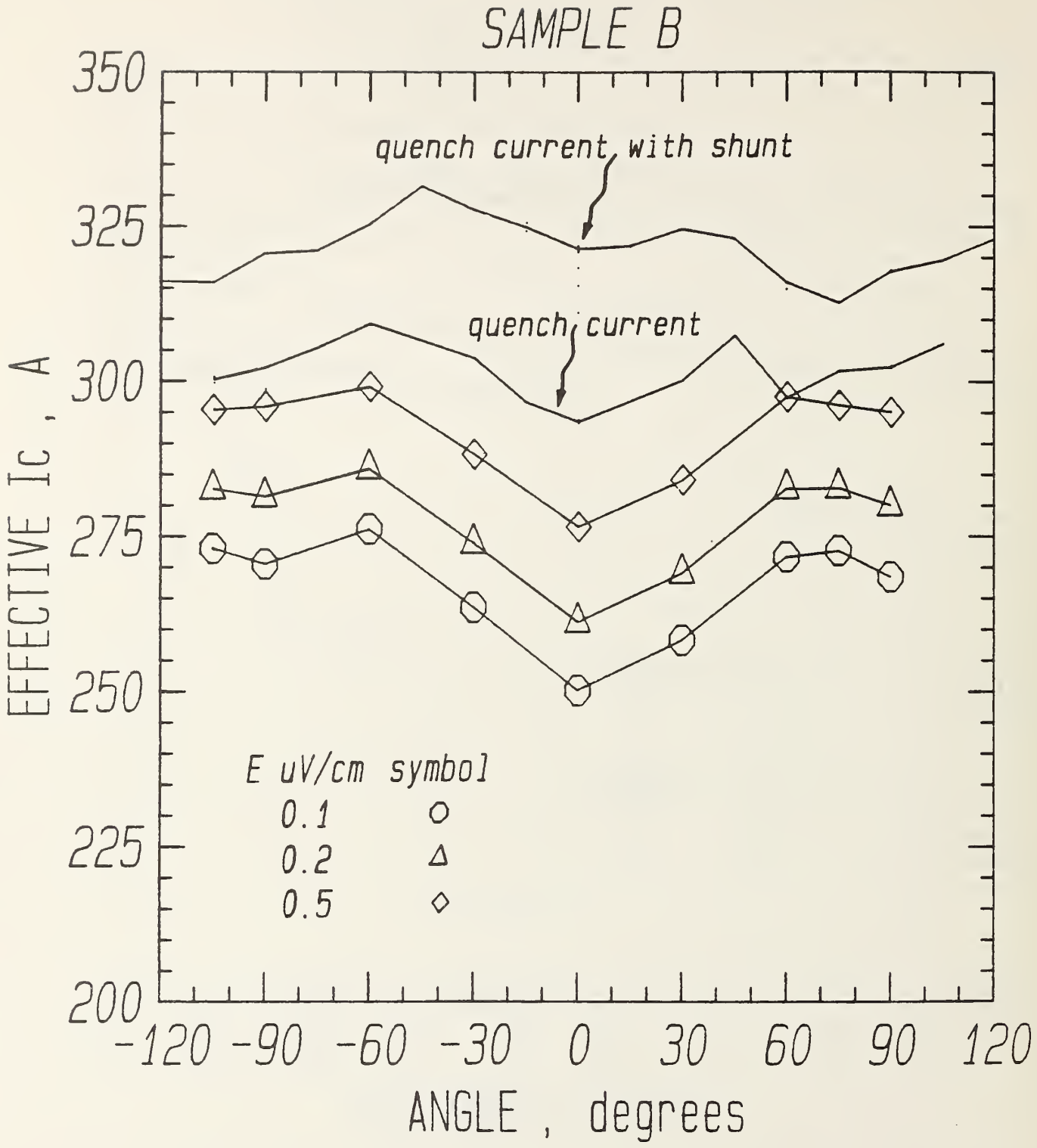

Figure 18. Sample B, effective critical current and quench current versus angle.

Table 2. Percentage differences in I_c from starting wire I_c's at 5 T, 4.0 K, and 0.1 μV/cm

Starting Wire I_c	Sample A 320 A		Sample B 347 A	
Field Angle	0°	90°	0°	90°
highest segment	+ 2.8%	- 4.7%	- 4.6%	- 4.0%
lowest segment	-25.3%	-15.3%	-37.5%	-34.9%
effective I_c	- 6.9%	- 7.5%	-27.7%	-22.8%

amount of current transfer voltage indicates that there is not very much current redistribution taking place at about 70% of I_c. Current redistribution that takes place closer to I_c will show as a lowering of n, the exponent in the empirical relationship $V \alpha I^n$.

The current transfer correction as a function of position for Sample B at 0 and 90°, respectively, are plotted in Figs. 21 and 22. The voltage on the center of the thin edge is significant, at both 0° and 90°. If this is intrinsic to the cable (i.e., occurs at every thin edge), it may start to have implications on the performance of the cable. The difference between 0 and 90° may be due to the relative improvement of I_c for the center of the thin edge at 90°. The fact that it is larger on this strand than on Sample A, measured in the same way, may indicate that it is intrinsic. However, more current-transfer voltage will appear in a short sample geometry. If the implications of this are significant, an experiment can be designed to determine how much is intrinsic.

The shape of the voltage-current curve near I_c can give insight into state of the filaments in a conductor [8]. A figure of merit is the exponent in the empirical relationship $V \alpha I^n$. A plot of the exponent n as a function of angle for each segment of Sample A is shown in Figs. 23, 24, and 25. The net value is 25 to 30, which is typical for cables. The highest values are an artifact of a fit to a limited number of points at low voltage with a high percentage of noise. The dip in the exponent for the center of the cable face around 0° is not now understood.

Other parameters

A plot of the electric field at 330 A as a function of angle for each segment of Sample A is shown in Figs. 26, 27, and 28. These plots display another asymmetry of the corners which was expected. For the corners of each edge, the peaks in the electric fields (lowest I_c) occur on opposite sides of 90°. This is not the mass flow asymmetry discussed above but an aspect ratio effect. It occurs because the net deformation direction for these two corners are shifted on either side of 90° (see the cable cross sections).

The critical temperature for a given magnetic field, T_c^*, is a parameter in the linear approximation of the temperature dependence of I_c. Table 3 shows values of T_c^* that were determined for some angles and segments of both samples at 5 and 8 T. Because of the small tap separations, the uncertainty of these values was about ±0.3 K at 5 T and ±0.1 K at 8 T. These data at 8 T indicate that T_c^* was a little higher for Sample B (larger filaments) and that there may not be much angular and positional dependence.

The results of the I_c data at 8 T for both samples were very similar to those presented at 5 T. The only difference observed was a slight decrease in the range or distribution of critical currents at 8 T. All of the curves had the same general character.

E. DISCUSSION

Understanding the relationship between the mechanical deformation in the cabling process and the electrical performance may lead to improvements in the

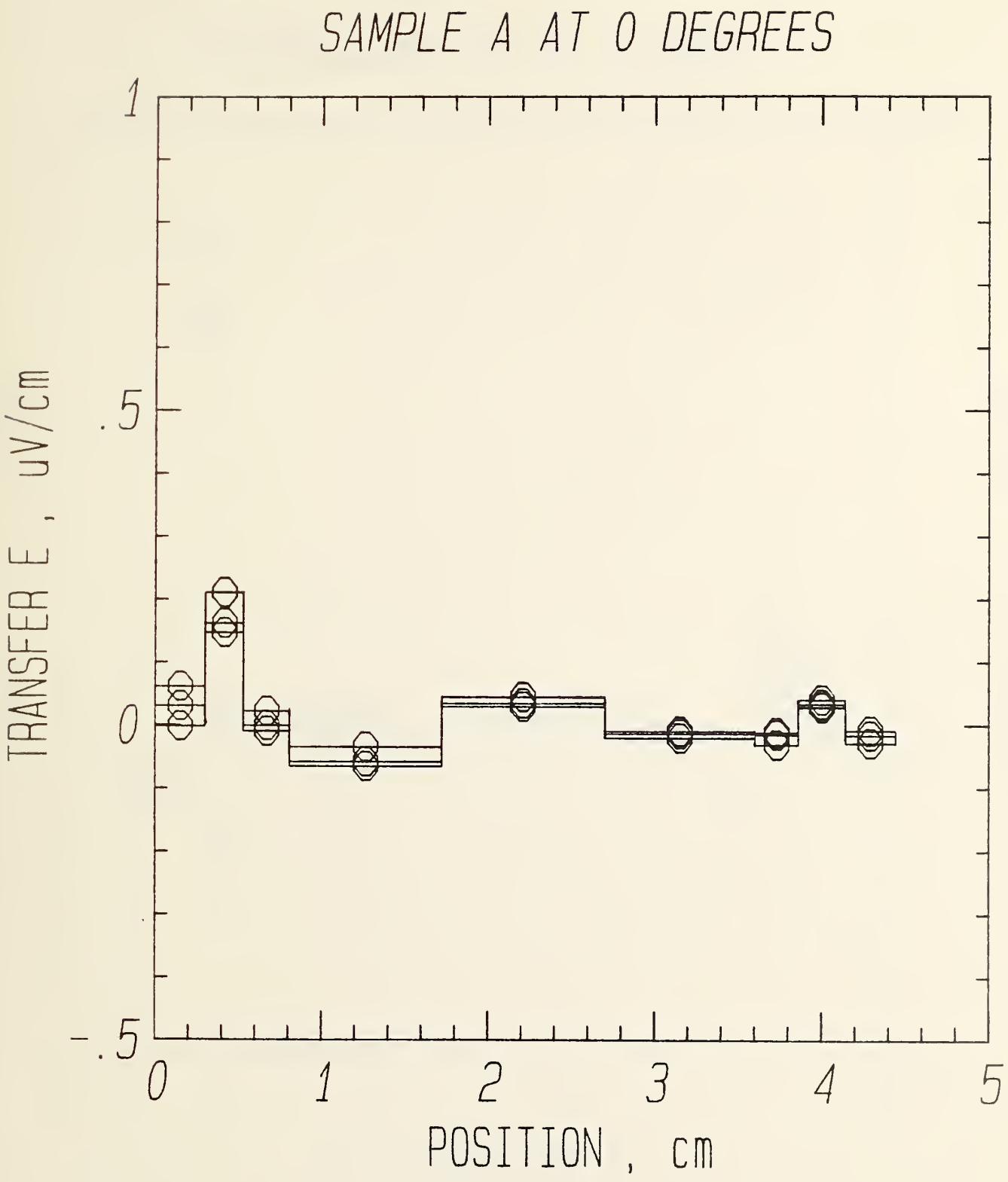

Figure 19. Sample A, transfer electric field versus position at 0°.

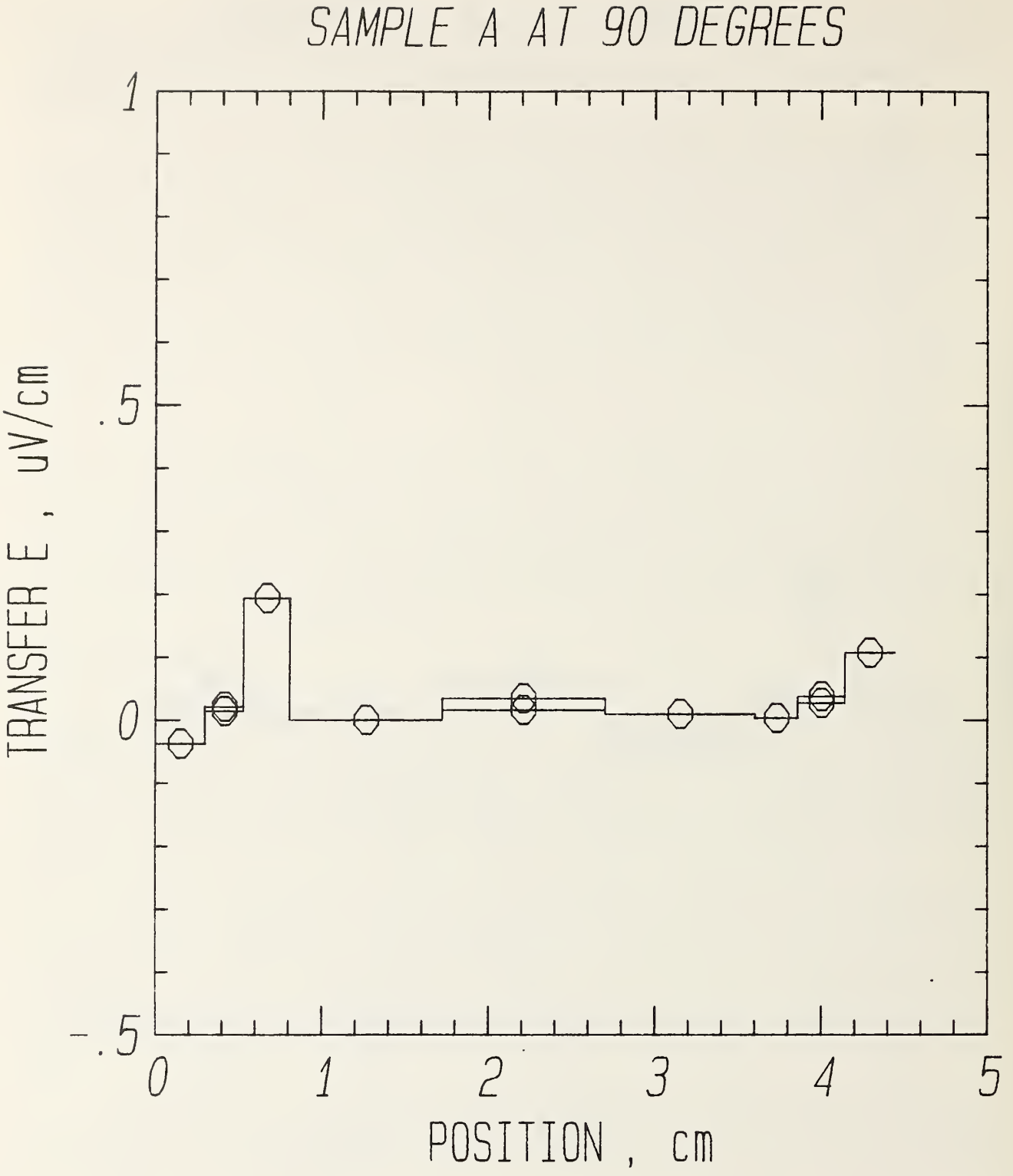

Figure 20. Sample A, transfer electric field versus position at 90°.

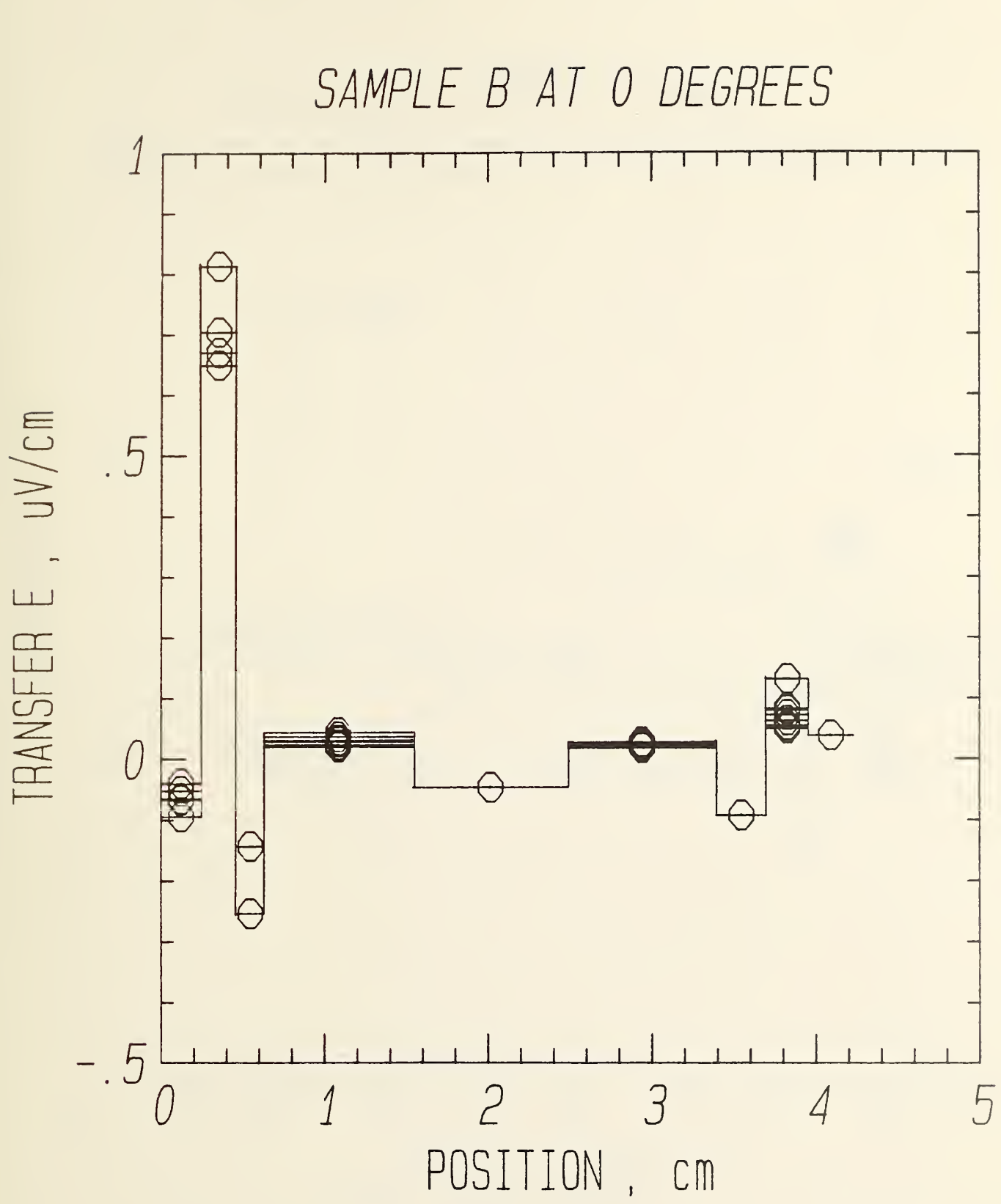

Figure 21. Sample B, transfer electric field versus position at 0°.

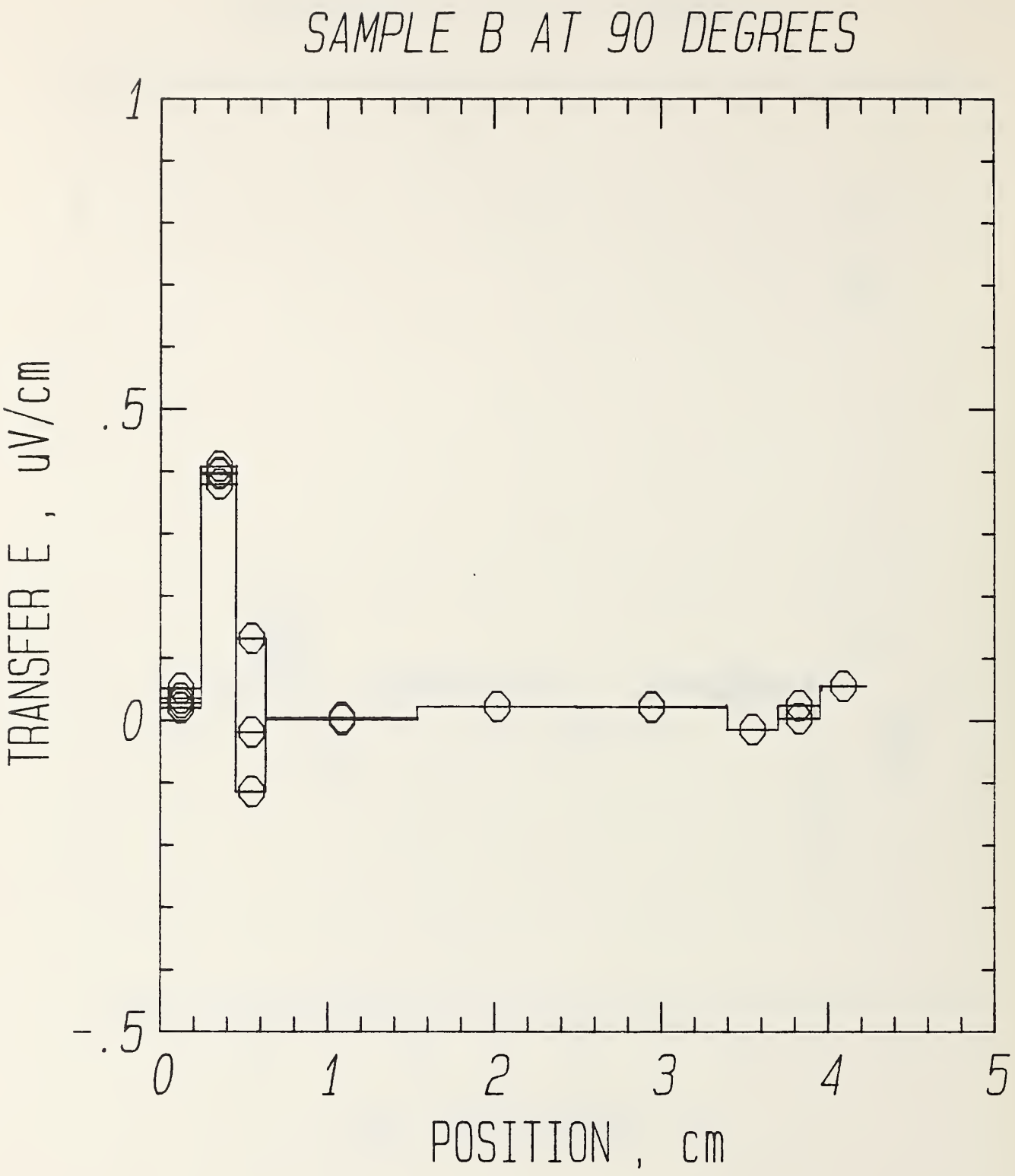

Figure 22. Sample B, transfer electric field versus position at 90°.

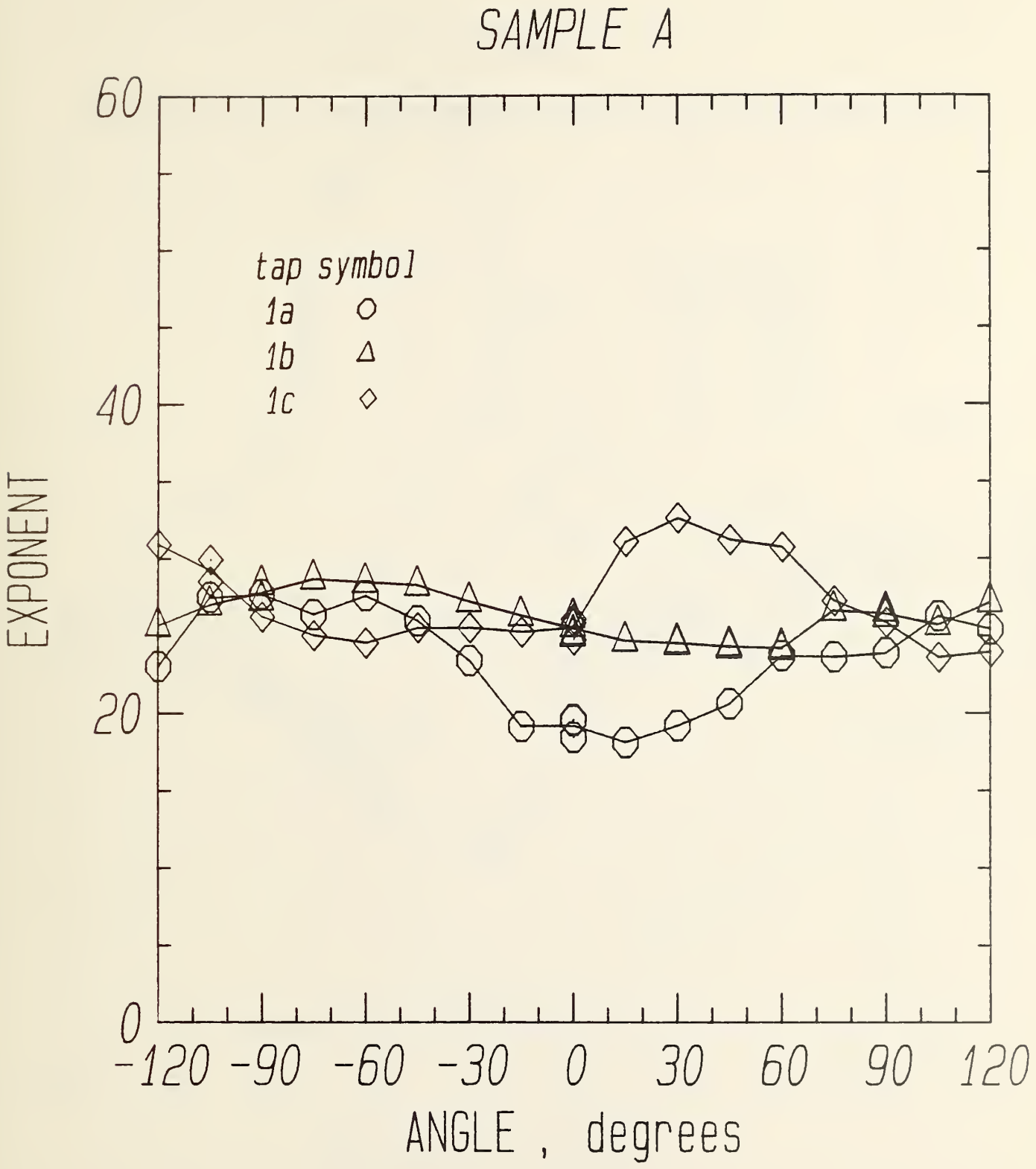

Figure 23. Sample A, exponent versus angle for thin edge taps.

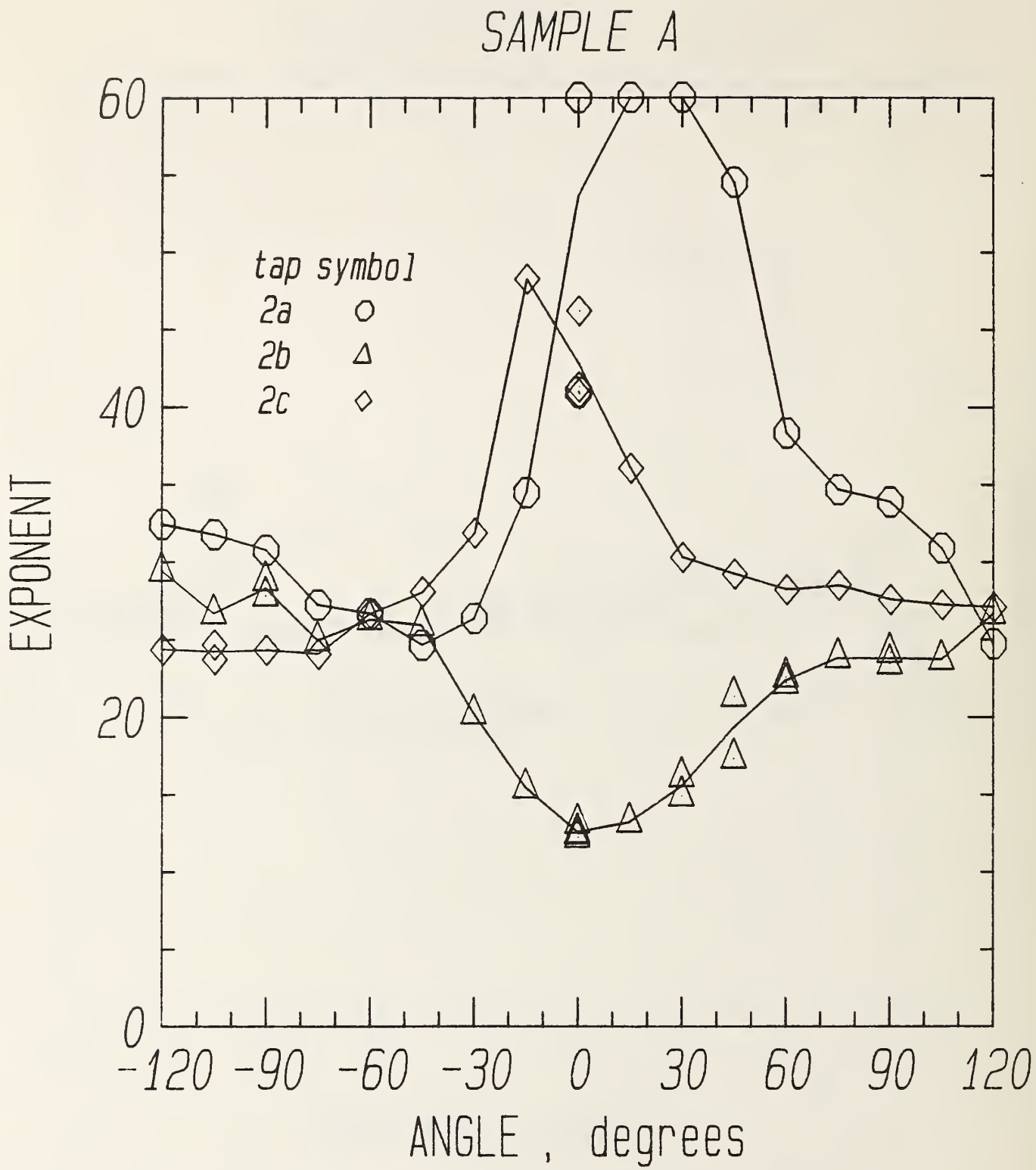

Figure 24. Sample A, exponent versus angle for cable face taps.

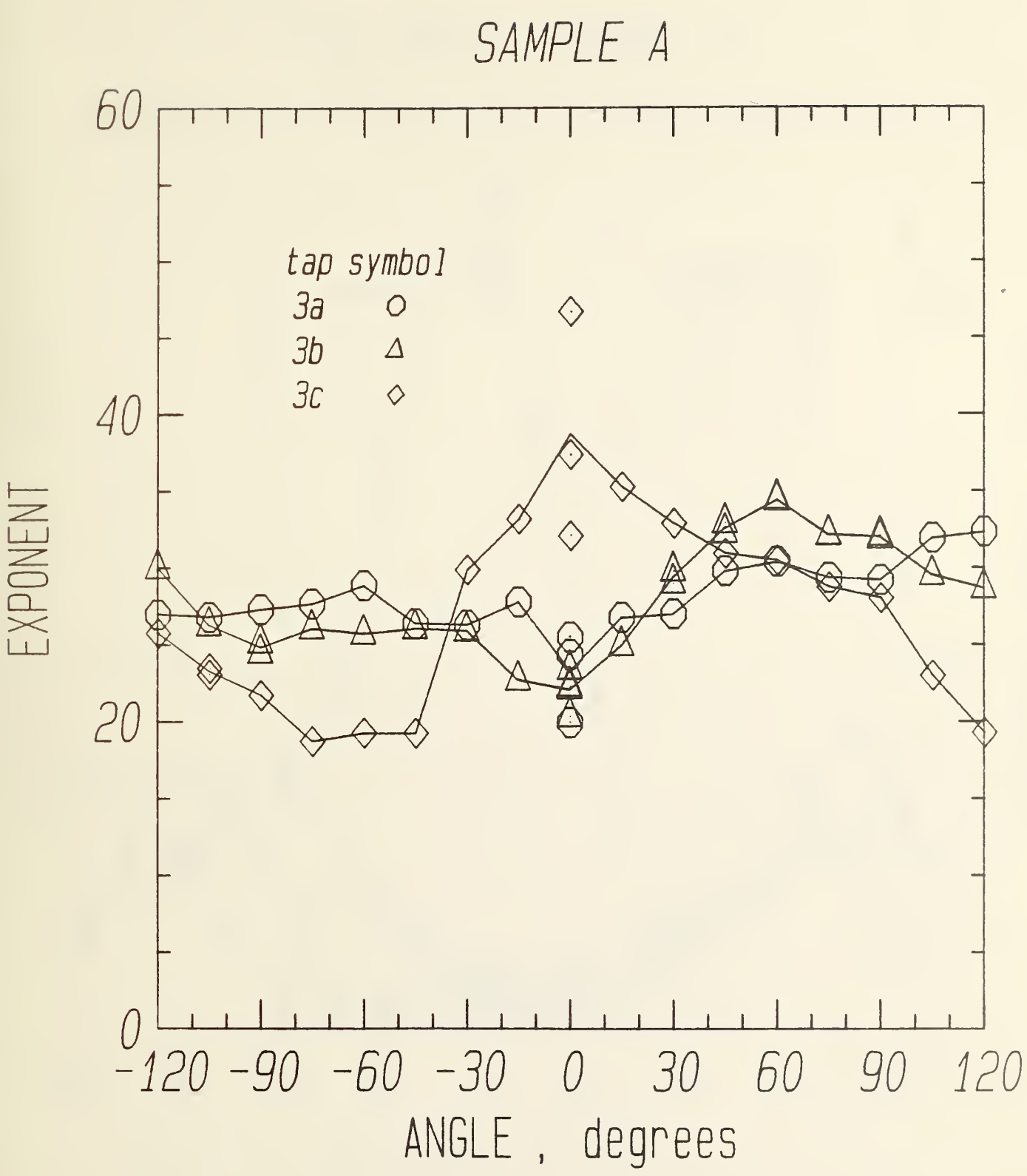

Figure 25. Sample A, exponent versus angle for thick edge taps.

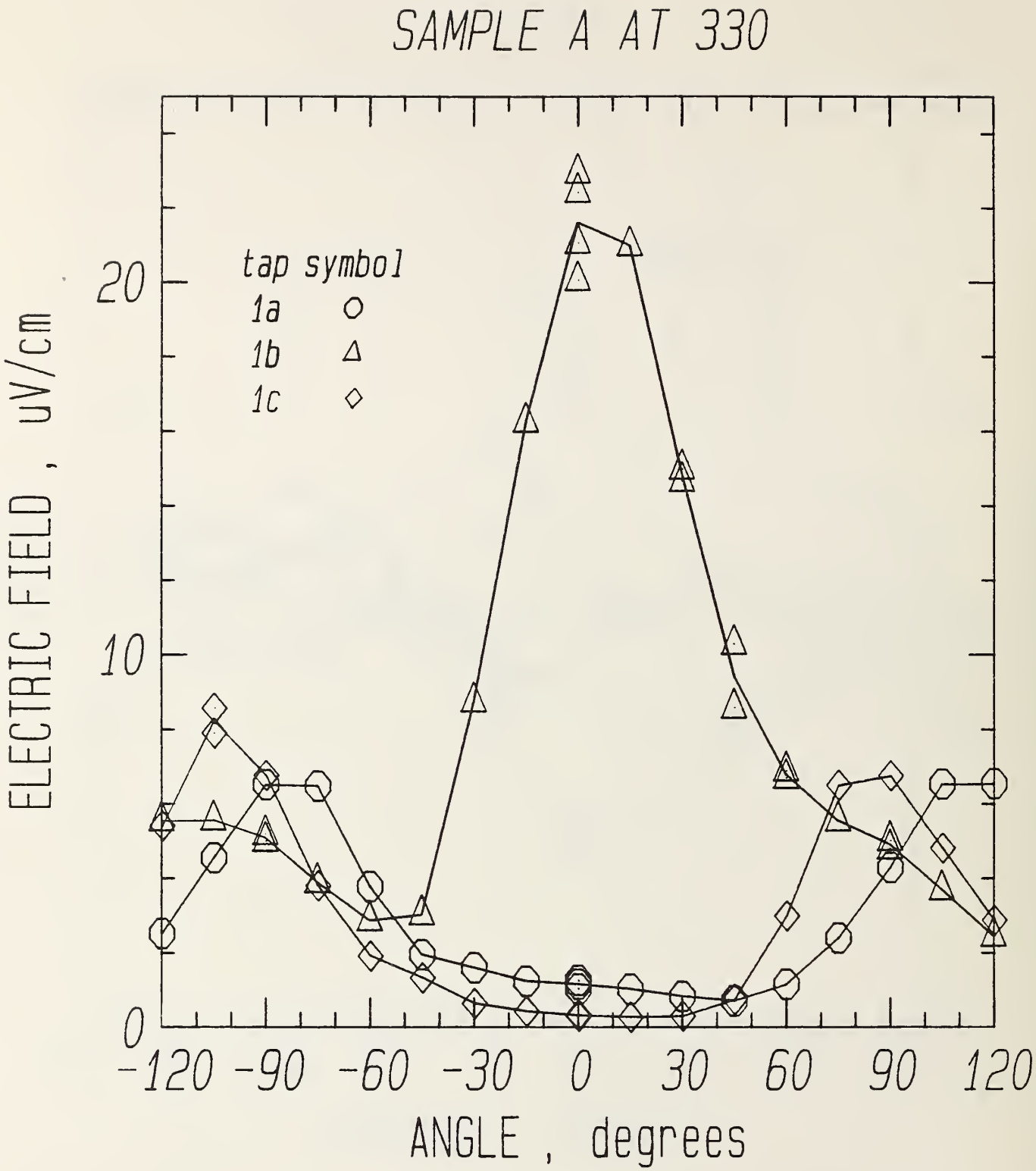

Figure 26. Sample A, electric field at 330A versus angle for thin edge taps.

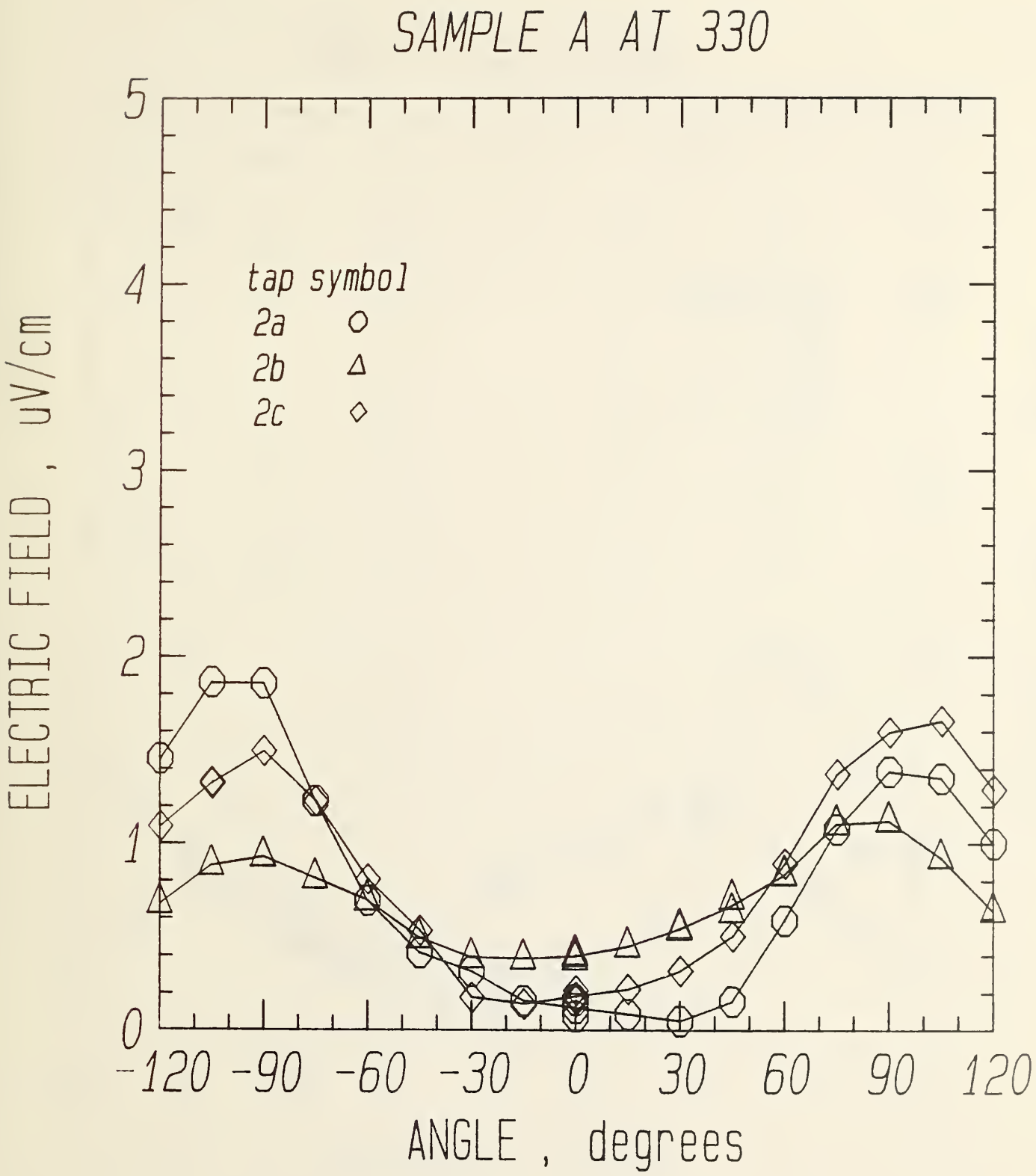

Figure 27. Sample A, electric field at 330A versus angle for cable face taps.

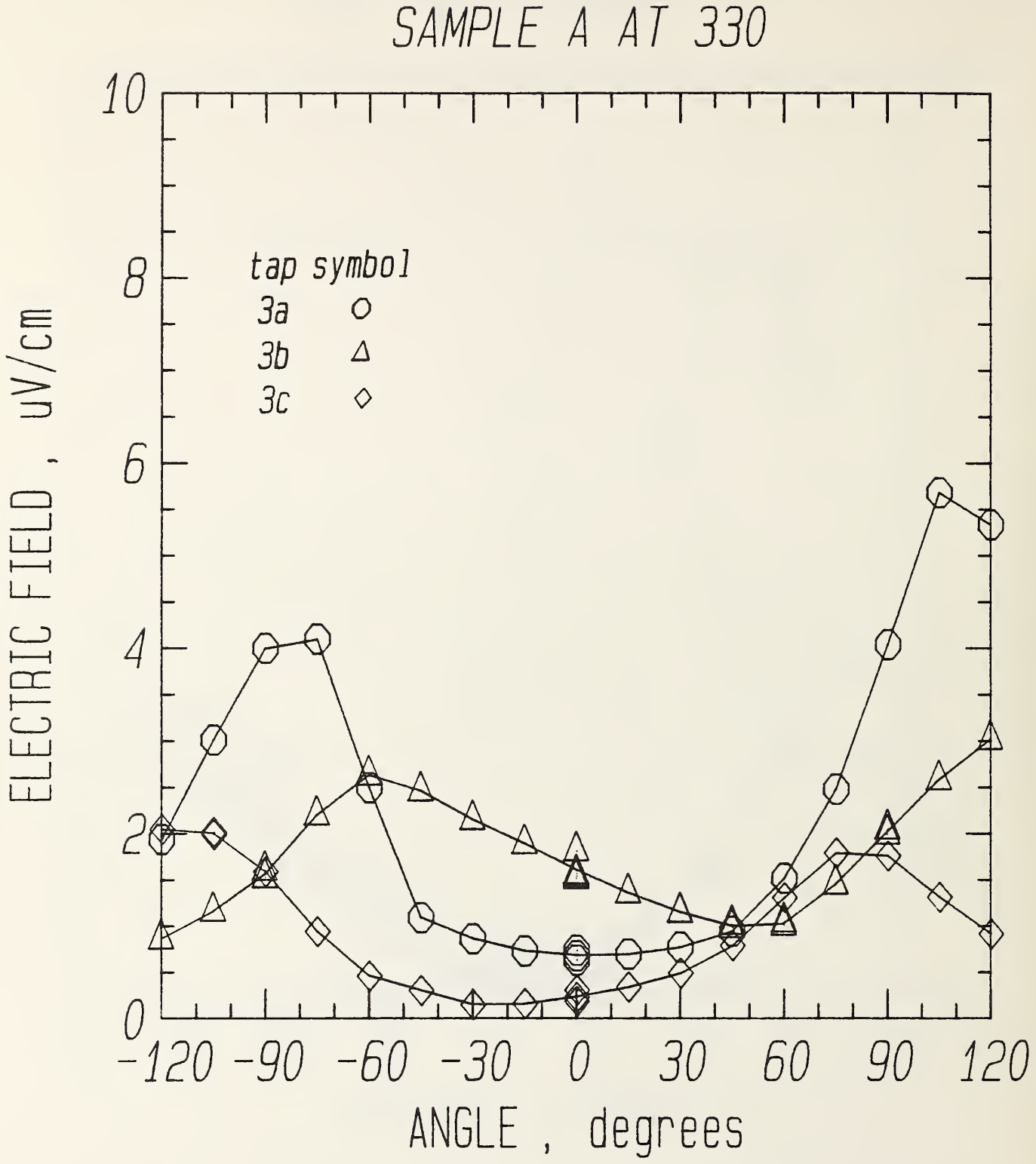

Figure 28. Sample A, electric field at 330A versus angle for thick edge taps.

Table 3. T_c^*, K

	Sample A			Sample B	
5T	Tap	0°	90°	Tap	0°
	1b	7.39	7.78	1a	7.81
	2b	7.57	7.68	1b	7.98
	3b	7.88	7.46	3b	7.68
8T	Tap	0°	90°	Tap	0°
	1b	5.68	5.67	1a	6.00
	2b	5.62	5.58	1b	5.95
	3b	5.66	5.57	3b	5.77

critical current of a cable. Comparisons of these two samples should be tempered by the fact that the starting wires were not the same but were similar enough to support the conclusions drawn from each sample.

Additional current sharing that can take place in the cable will help reduce the effects of local changes in critical current. However, the experiment of shunting Sample B by soldering another strand to it (with no transport current of its own) may indicate that the best case would only be a 7% improvement. On the other hand, any compromise in end cooling could have a significant effect. One proposed [9] change that would compromise stability is use of a Cu-Ni matrix to possibly improve the drawing to finer filaments. This could decrease the strand I_c to that of the local weak link, a significant decrease.

An open question in this work is: What does this imply about cable measurements? The answer may be beyond the scope of the program. The aspect ratio effects are opposite for different parts of the conductor and the thin edge is clearly the weak link. If the local I_c were homogeneous along a strand, the solution would be simpler [4]. The fortunate observation was that the effective I_c criterion corresponds to an average electric field criterion (or resistivity criterion) if end cooling is adequate. In the bifilar, short cable measurements, the critical current may have to be measured in both current directions with the magnetic field perpendicular to the cable face in order to attempt to cancel the asymmetry in the cable edges. This may not be a problem for the better cables because I_c of the thin edge at 90° is not as depressed as for more degraded cables. For a more degraded cable, the peak field on the thin edge may further lower I_c to the point where local heating becomes a problem.

A comparison of these results on extracted strands with independent measurements [3] on the same cable is instructive. The degradation in Sample A measured here was very close to its cable measurements using the same material. Using their notation [4] for degradation, the strand value measured here was 7% (see effective I_c in Table 2), its cable value was 9%. The anisotropy of Sample A was 11% for the cable measurement and 1% for the strand measurement. The difference in anisotropy may have to do with the details of self-field effects and no conclusions are drawn from this difference. The values of degradation in Sample B were also very close to the cable measurement; the strand value was 23%, the cable value was 22%. The Sample B anisotropy was -11% for the cable (I_c at 0° lower than at 90°) and -5% for the strand. Thus, the limiting case for Sample B was 32% less than starting wire according to the cable measurements and 28% according to strand measurements. The agreement between these two measurements was good but further improvements may be possible.

These results have two implications for short-sample critical-current testing of cables for SSC. First, these data indicate that both magnetic-field orientations need to be tested in order to determine the limiting case for the critical current. As shown above, for more degraded cables, the parallel-field case may limit. In the less degraded cables, the perpendicular case limits. The amount of degradation is not known beforehand, so both orientations need to be measured.

Second, the difference between thick and thin edge degradation shown in these data indicates that changing the direction of the test current (for each field orientation) will affect the critical current. This is because the location of the peak magnetic field changes with current direction (see Fig. 3 in [4]). Thus, the peak field location relative to the thin edge should be recorded. The conservative approach in short-sample cable tests would be to make the measurement for both directions of the test current and use the critical current for the worst case. The additional measurements will help increase the understanding of cable degradation.

There might be differences in cable degradation for cables made with a powered turkshead. The cables tested here were made without power to the turkshead. Future tests will be made when samples and time permit.

Other future tests that have been considered are: inner 23 strand cable, cable with strand twist and cable lay in the same direction, and outer cable with 29 strands instead of 30. In the present dipole magnet design, the cable used for the inner windings has 23 strands with a copper-to-superconductor ratio of 1.3/1. A lower ratio may cause more anisotropy in filament deformation and result in a larger aspect ratio effect. A lower ratio may also compromise the end cooling around the locally depressed I_c and could introduce more degradation to the local I_c. Making the outer cable with 29 strands instead of 30 may decrease the amount of degradation that occurs on the cable edges because of less edge compaction. The compaction at the edge will be less due to the lower number of strands and also possibly due to the odd number of strands. The odd number staggers the position on each side of the cable where the strands round the cable edge, thus avoiding having a strand centered on each edge at the same time as the cable passes through the turkshead. There is a possibility that the 29 strand cable may have a higher critical current than the 30 strand cable with the same cross-sectional area because the edge degradation dominates the 30 strand cable. The 29 strand cable would also result in a saving in material. The strand diameter might have to be increased in order to make the cable mechanically stable. This may also further increase the critical current of the cable.

F. CONCLUSIONS

1. Cabling can lead to very localized reduction in critical current within a single strand. The lowest critical current was observed for the central flat part of the thin edge and this segment contributes most of the overall voltage drop.

2. The widest spread in local critical current values along the cable strands occurs with the magnetic field perpendicular to the cable edge. Unfortunately, this is near the orientation that is most critical for a dipole magnet.

3. The cable corners have a critical-current asymmetry in the same cable pitch direction. This may be due to mass flow during the cable fabrication.

4. The relevant critical-current criteria for local measurements may be a spatial average, because of the extreme localization of damage, limited extent of the voltage, and strong end cooling effect which all limit the local tem-

perature rise. Any compromise in sample stability may lower the critical current to that of the weak link.

5. Despite large local variations in critical current, the quench current and effective critical current do not vary much with angle. The effects of the conductor aspect ratio and cable pitch angle are opposite for different segments of the cable strand, causing them to tend to cancel.

6. Any additional lowering of the thin edge critical current is directly reflected in the quench current and effective critical current of the cable strand. For critical-current degradation greater than observed in Sample A, the critical current of the weak link seems to dominate.

ACKNOWLEDGMENTS

The authors extend their thanks to S. L. Bray and W. E. Look for sample holder construction, data analysis, and plotting; R. M. Scanlan and J. M. Royet (Lawrence Berkeley Laboratory) for samples and discussions; R. A. Shenko for typing this report; and to the rest of the Superconductor and Magnetic Measurements Group.

REFERENCES

1. R. Scanlan, J. Royet, and C. E. Taylor, "Superconducting Materials for the SSC" Adv. Cryog. Eng. - Materials, Vol. 32, Plenum Press, New York (1986) in press.

2. D. C. Larbalestier, A. W. West, W. Starch, W. Warnes, P. Lee, W. K. McDonald, P. O'Larey, K. Hemachalam, B. Zeitlin, R. Scanlan, and C. Taylor, "High Critical Current Densities in Industrial Scale Composites Made From High Homogeneity Nb 46.5 Ti", IEEE Trans. on Magnetics, MAG 21, 269, 1985.

3. W. B. Sampson, Brookhaven National Laboratory., Upton, New York, and R. M. Scanlan, Lawrence Berkeley Laboratory, Berkeley, California, private communications (1986).

4. M. Garber and W. B. Sampson, "Critical Current Anisotropy in NbTi cables," IEEE Trans. on Magnetics, MAG 21, 336, 1985.

5. L. F. Goodrich, W. P. Dubé, E. S. Pittman, and A. F. Clark, "The Effect of Aspect Ratio on Critical Current in Multifilamentary Superconductors," Adv. Cryog. Eng. - Materials, Vol. 32, Plenum Press, New York (1986) in press.

6. A. F. Clark, L. F. Goodrich, F. R. Fickett, and J. V. Minervini, "Development of Standards for Superconductors, Interim Report Oct. 80 to Jan. 82", NBSIR 82-1678, National Bureau of Standards, Boulder, Colorado (July 1982).

7. L. F. Goodrich, J. W. Ekin, F. R. Fickett, "Effect of Twist Pitch on Short-Sample V-I Charateristics of Multifilamentary Superconductors," Adv. Cryog. Eng. - Materials, Vol. 28, Plenum Press, New York (1981), p. 571-580.

8. J. W. Ekin, "Superconductor Coil Characterization, Quarterly Progress Report", NBS Report # SR-724-3-82, March 1982. J. W.Ekin, "Superconductor Coil Characterization, Quarterly Progress Report", NBS Report # SR-724-6-82, June 1982.

9. 5th Workshop on NbTi Superconductor, March 25-27, 1986, Menlo Park, CA

IV. EFFECT OF FILAMENT IRREGULARITY ("SAUSAGING") ON ELECTRIC-FIELD VS CURRENT CHARACTERISTICS OF NbTi SUPERCONDUCTORS

by J. W. Ekin

SUMMARY

This article contains two internal reports of the Superconductor and Magnetic Measurements Group of the National Bureau of Standards, issued consecutively in March and June, 1982.[1,2]

Report I contains the first measurements of a correlation between filament irregularity (sometimes called "necking" or "sausaging") and the shape of a superconductor's electric-field vs. current characteristic. Data are presented which show that the greater the extent of irregularity in filament crossectional area the flatter the take-off in the electric field vs. current (E-I) characteristic. The shape of the E-I characteristic is quantified in terms of the resistive transition parameter n, defined by $E \alpha I^n$. Low values of n indicate significant filament irregularity. It is proposed in Report I that the parameter n could be used as a valuable index of filament quality in evaluating different superconductors for practical applications.

A model is also suggested in Report I to explain this effect. The necking depresses the critical current of a filament locally, which forces current to transfer across the normal matrix material into (unnecked) neighboring filaments. The current transfer is intrinsic to the wire and occurs continually along its length wherever the filaments are necked down to a smaller crossectional area. These currents crossing the matrix generate significant voltage at transport current levels well below the critical current, which causes the reduction in the value of n.

Report II presents a quantitative relationship between n and the statistical distribution of filament diameters measured for the NbTi superconductors studied in Report I. The relationship may be useful as a quick method of estimating the extent of sausaging in practical multifilamentary NbTi superconductors from measurements of n.

In the years since these reports were first publicized,[1,3] the correlation of n with filament sausaging and the filament-necking model originally proposed here have been confirmed by further research at several of the U. S. superconductor manfacturers,[4,5] Brookhaven National Lab,[4,6] Fermi Lab,[4] and the University of Wisconsin.[5,7]

The transition parameter n was introduced some time ago by Voelker[8] in another connection relating to filament breakage rather than sausaging. The n value ($n \approx 3$) was significantly lower than the n values reported here; in a sense it represents a logical extension of filament sausaging to the extreme case of

filament breakage. We suspect that filament sausaging may have also contributed to the relatively low n values ($7 \leq n \leq 12$) in some of the "good" multifilamentary samples he measured.

The identities of the superconductors have been relabeled, but otherwise the reports appear in their original form.

I. EFFECT OF SUPERCONDUCTOR FILAMENT IRREGULARITY (Report No. SR-724-13-82)[1]

During critical-current testing of several NbTi conductors, it was noticed that the electric field versus current (E-I) characteristic for one conductor did not show the sharp take off behavior normally observed in other NbTi:copper superconductors we have tested. Instead, the rise in voltage in this conductor started well below the critical current, I_c, showing a gradual rise as I approached I_c rather than a sharp rise right at I_c (see Sample I in Fig. 1). This limits the usefulness of the conductor in magnet applications, since a significant electric field in the conductor below I_c leads to heating and decreased stability. Several tests were consequently undertaken to deter-mine the source of this electric field.

The effect may be quantified by describing the superconductor E-I characteristic in terms of the equation,

$$\frac{E}{E_c} = \left(\frac{I}{I_c}\right)^n ,$$

where I_c is the critical current and E_c is the electric-field criterion at which I_c is determined. The larger the exponent n is, the sharper the E-I takeoff at I_c. Thus, large n is desirable for magnet applications.

In Fig. 2, log E/E_c versus I/I_c is plotted for Sample A as well as another previously tested conductor, sample B, in order to determine comparative values of n. As seen from the curves in Fig. 2, sample B has an n value of about 35, whereas sample A has an n value of only about 18.

One possible source of the low n in Sample I is filament irregularity. If there is sausaging in the filaments, current will transfer out of a filament where it necks down, into a neighboring filament which can carry the extra current. When the current in the neighboring filament encounters a necked region, it too will be forced out of that filament through the matrix material and into another filament (perhaps back into the original filament if its diameter is back to average size or greater). In this manner, filament irregularity forces current transfer through the resistive matrix material continuously, causing significant electric fields along the conductor well below I_c, resulting in a low value of n.

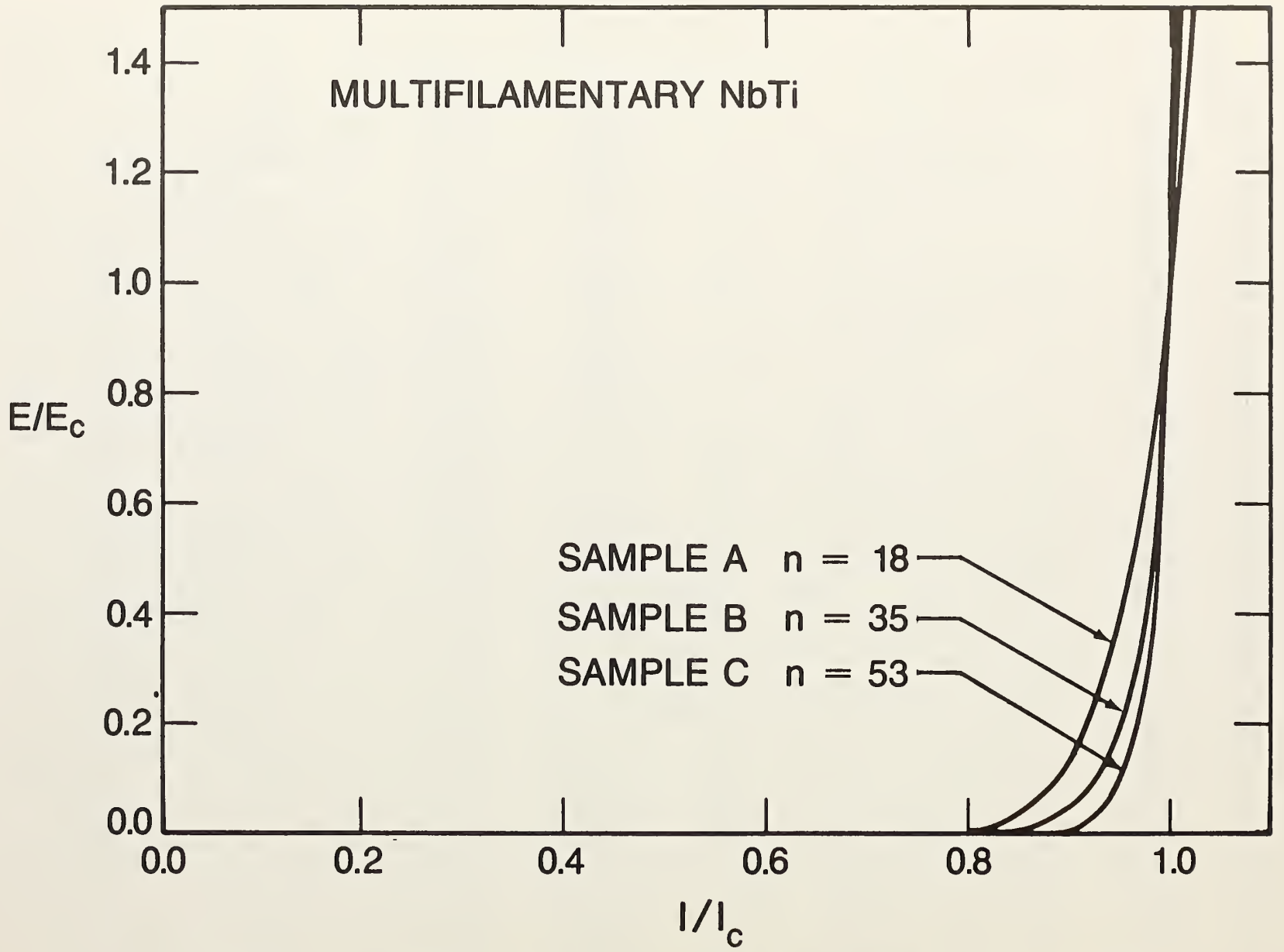

Figure 1. Normalized electric field vs current plots for three multifilamentary NbTi superconductor, showing the more gradual resistive transition in sample A compared with samples B and C.

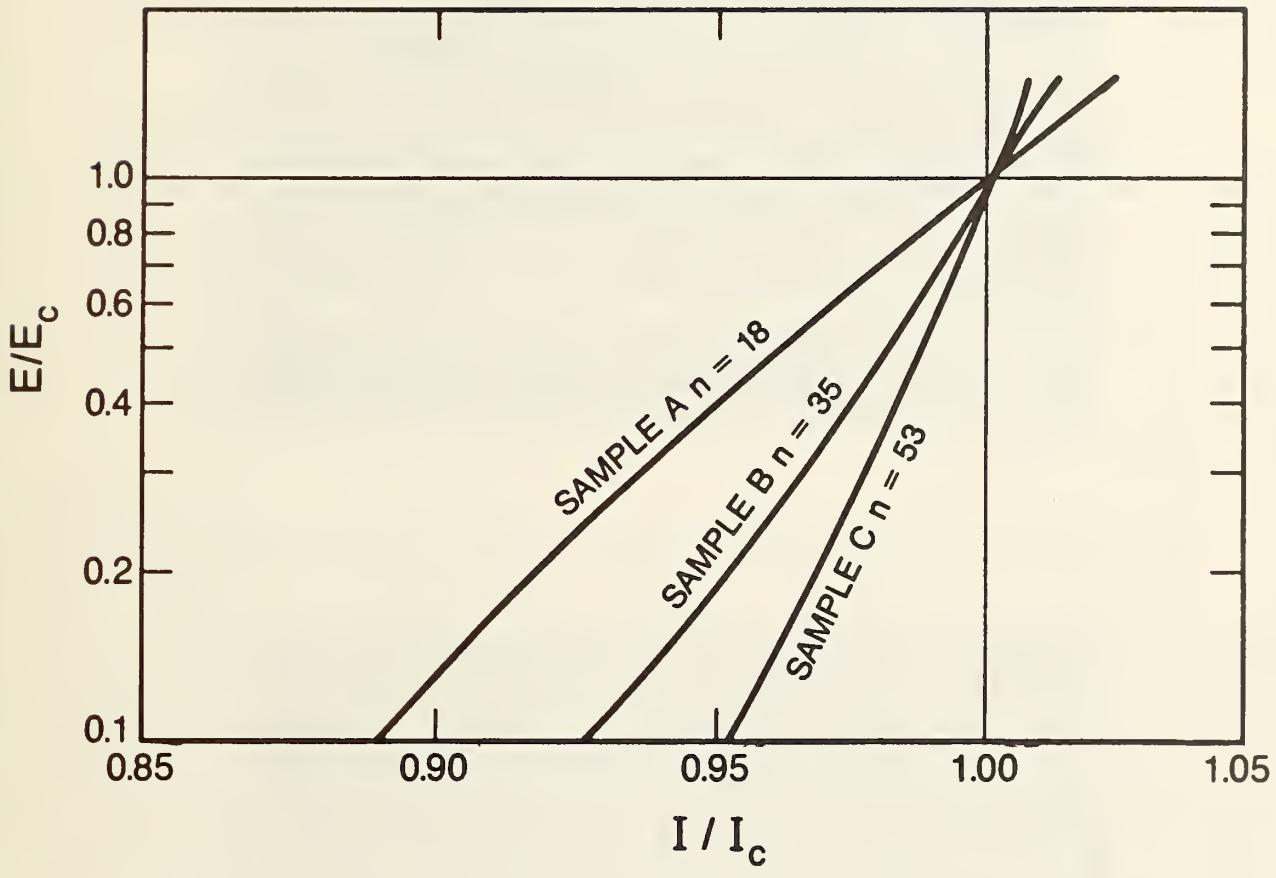

Figure 2. Logarithmic plot of electric field versus current for the curves in Fig. 1, showing the low value of n in sample A compared with samples B and C (n is defined by the relationship $V \alpha I^n$).

To test this hypothesis a series of scanning electron micrographs were made of the filaments in each conductor. The copper matrix of each conductor was chemically removed and the filaments photographed longitudinally along their length. The results are shown in Figs. 3A and 4A. Significantly greater filament irregularities were found in sample A compared with sample B. As shown in Table 1, the average diameter fluctuations ΔD for sample A amounted to about 9 μm, or about 33% of its average filament diameter $\langle D \rangle$. In sample A, on the other hand, ΔD was less than 7 μm, or about 20% of its average filament diameter. The amount of filament irregularity in these conductors thus correlates well with degradation in the value of n characterizing their E-I curves.

To see if this large filament irregularity is a characteristic of conductors containing a large volume fraction of copper, a third conductor, Sample C, was also tested. The conductor contained a large amount of copper similar to sample A but had a somewhat larger filament diameter. As shown in Fig. 5 and Table 1, ΔD for this conductor was only about 6% of its $\langle D \rangle$. The E-I characteristic of this conductor was correspondingly sharper, with a measured n value of 46, which is more than twice that of sample A. Thus, large values of ΔD need not be an inherent characteristic of conductors containing high percentages of copper stabilizer.

In summary, these results show that the degradation in the value of n for these multifilamentary NbTi conductors correlates well with the amount of filament irregularity observed in each and that such irregularities need not be a characteristic of conductors containing a large fraction of copper. The value of n measured for sample A is significantly lower than that measured for other NbTi conductors and these data would suggest it could be substantially improved by reducing the large filament diameter irregularities observed in this conductor. Furthermore, it would seem that the parameter n could be used as a valuable index of filament quality in evaluating different superconductors. Certainly, n should be an extremely useful parameter in characterizing the quality of a superconductor's E-I characteristics, complementing the I_c value usually supplied with commercial conductors.

II. RELATIONSHIP BETWEEN n AND THE STATISTICAL DISTRIBUTION OF FILAMENT SIZES (Report No. SR-724-26-82)[2]

Report I reported that the electric field-versus-current characteristics for sample A did not show the sharp take-off normally found in other NbTi:copper conductor we have tested. The effect was quantified in terms of a parameter n, which for sample A was only about 18, compared with values of n=35 for sample B and n=53 for sample C (another high copper-to-NbTi ratio superconductor). The low value of n was ascribed to irregularities ("sausaging") in the filament diameter of sample A as

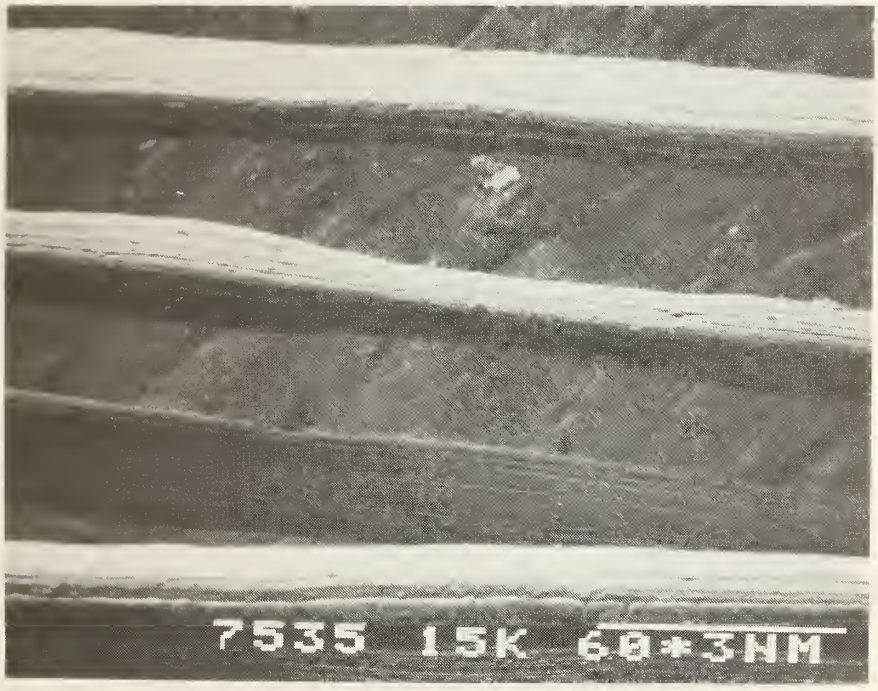

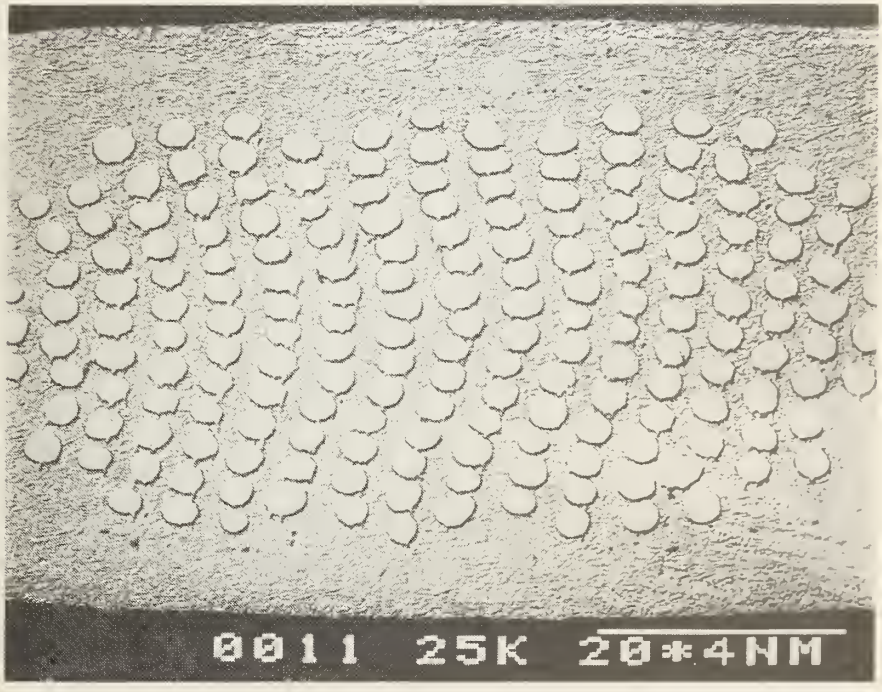

Figure 3. Longitudinal (a) and cross-sectional (b) views of the filaments in Sample A.

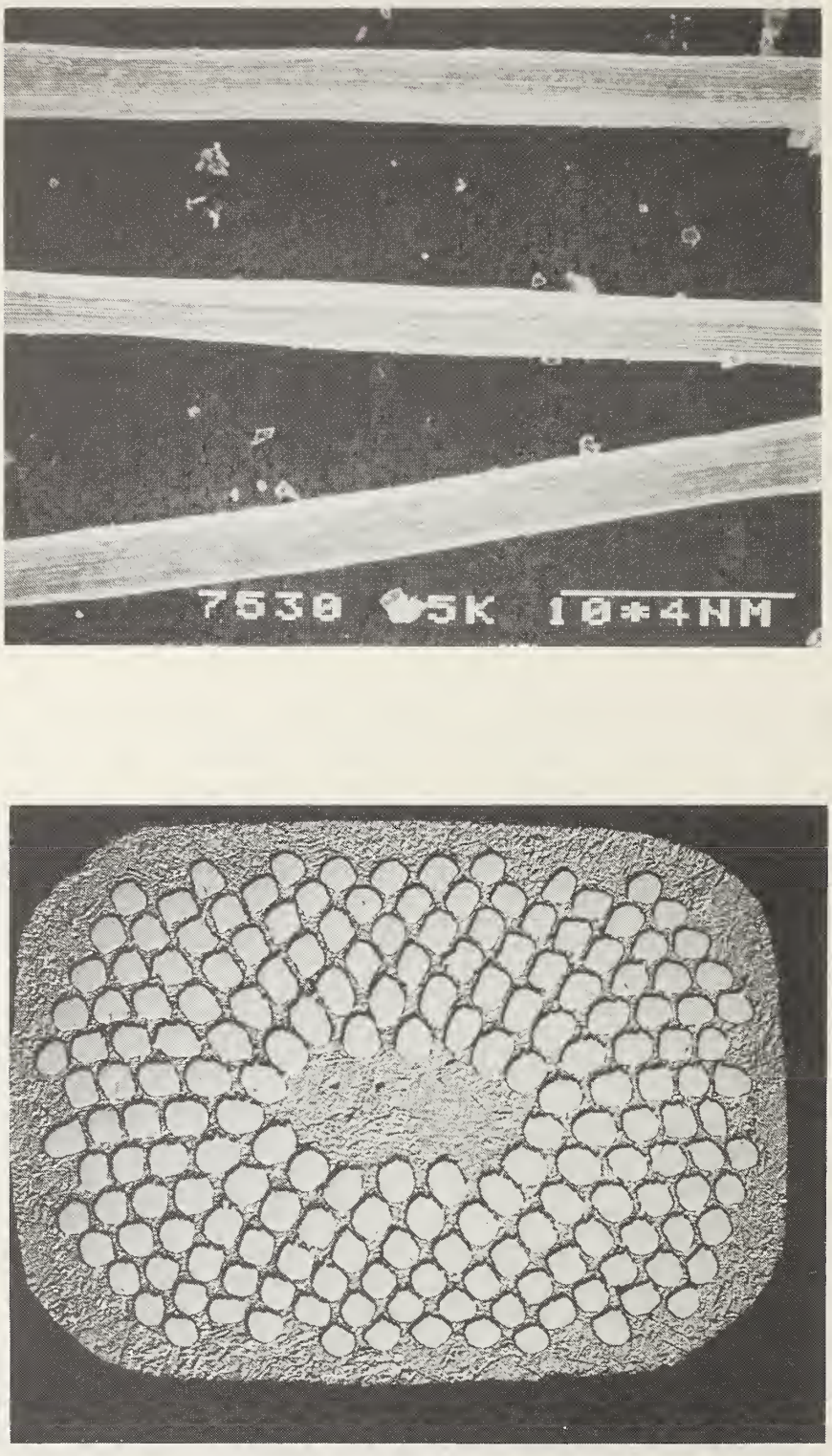

Figure 4. Longitudinal (a) and cross-sectional (b) views of the filaments in Sample B.

SAMPLE C

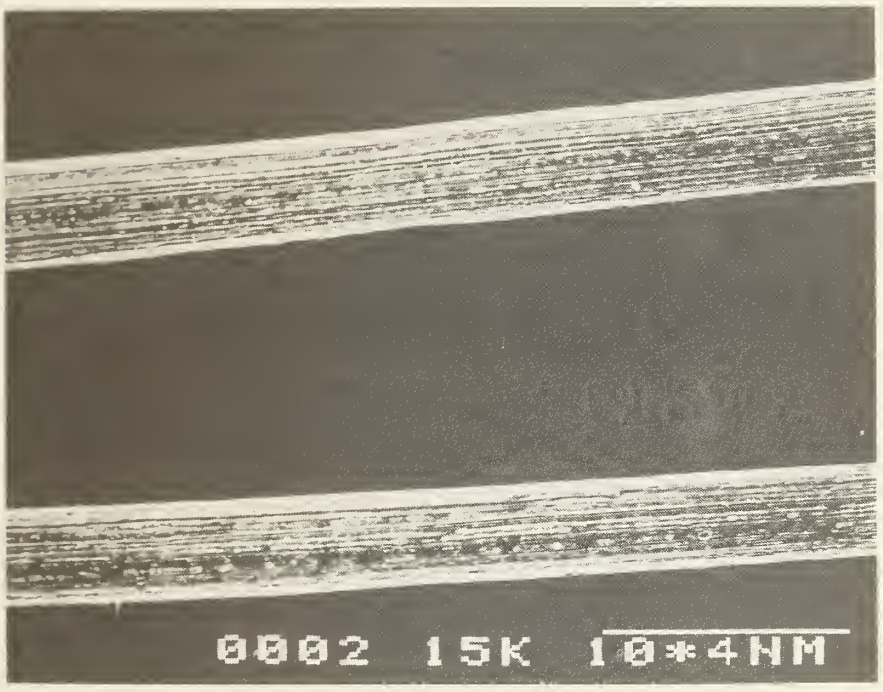

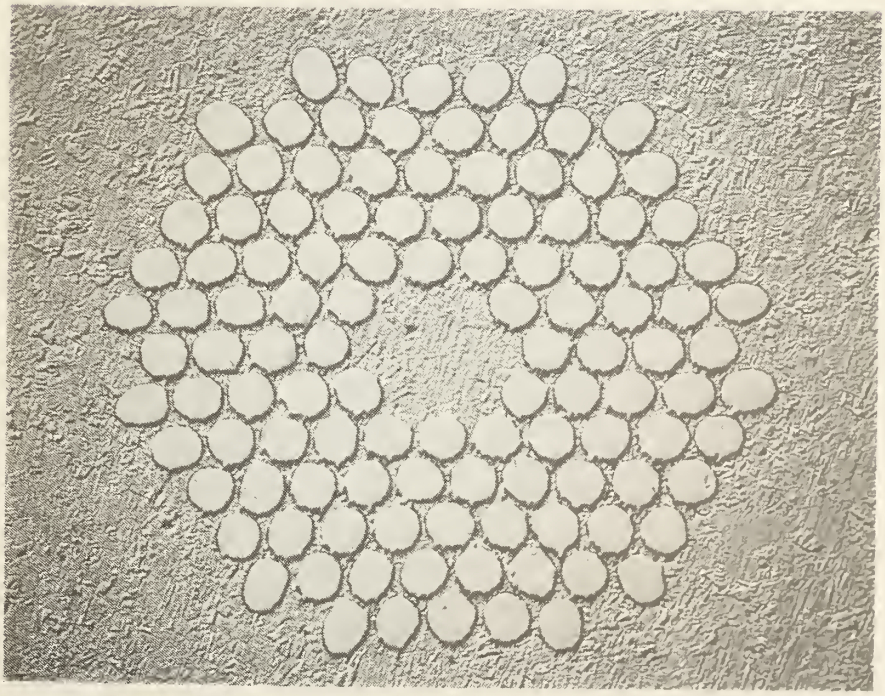

Figure 5. Longitudinal (a) and cross-sectional (b) views of the filaments in Sample C.

observed in SEM longitudinal micrographs of isolated filaments. In order to quantify these preliminary observations, a series of SEM micrographs of the complete cross section of the conductor have been obtained (shown in Figs. 3B-5B). From many measurements of the individual filament diameter in these micrographs, a statistical distribution of the filament diameters in each conductor has been obtained. Figure 6 shows the distribution of filament diameters D about the average filament diameter of each ring of filaments <D>. The spread in the distribution for sample A is much broader than for samples B or C, confirming the earlier qualitative treatment given the filament irregularities. The half width of the filament diameter distribution correlates very nicely with the variations in the parameter n. This evidence is consistent with the current-transfer hypothesis advanced in the previous quarterly report as the explanation for the relatively large electric field appearing in sample A at currents below the critical current.

From SEM micrographs in Fig. 3-5 note the presence of the large center island of copper in conductor Samples B and C, compared with the lack of this feature in Sample A. It is believed this center copper island is a significant factor in minimizing the filament irregularity problem (particularly in conductors having a high copper-to-superconductor volume ratio).

Note added in proof:

The n values reported above were nearly independent of magnetic field from 3 T to 7 T; over this field range they varied by less than about 5%. A graph of the standard deviation of the filament diameter distributions shown in Fig. 6 is plotted as a function of n in Fig. 7. The approximate relationship shown in Fig. 7 may be useful for quickly estimating the extent of filament irregularity in practical multifilamentary NbTi superconductors from measurements of n.

ACKNOWLEDGMENTS

The author extends his appreciation to E. S. Pittman and D. Rule for their assistance in reducing the filament-diameter distribution data, and to L. F. Goodrich for several helpful discussions. The initial work was sponsored by the Naval Ship Research and Development Center. Further data reduction and the publication of these reports were supported by the U. S. Department of Energy, Division of High Energy Physics under Interagency Agreement No. DE-A105-85ER40240.

References

1) J. W. Ekin, Superconducting Coil Characterization, Quarterly Progress Report No. SR-724-13-82, March 1982, unpublished.

2) J. W. Ekin, Superconducting Coil Characterization, Quarterly Progress Report No. SR-724-26-82, June 1982, unpublished.

3) First Workshop on NbTi Superconductor, University of Wisconsin, Madison, WI, July 1983.

4) Second Workshop on NbTi Superconductor, University of Wisconsin, Madison, WI, July 1984.

5) Third Workshop on NbTi Superconductor, Lawrence Berkeley Laboratory, Berkeley, CA, January 1985.

6) M. Garber, M. Suenaga, W. B. Sampson, R. L. Sabatini, Adv. in Cryo. Eng. 32 (1986) (to be published).

7) W. H. Warnes and D. C. Larbalestier, p. 156 in Proc. Int'l. Symp. on Flux Pinning and Electromagnetic Properties in Superconductors, Matsukuma Press (1986).

8) F. Voelker, Particle Accelerators 1, 205 (1970).

Table 1. Filament Diameter Variations for Three NbTi Conductors

Conductor	Size (mm)	No. Fil.	Twist Pitch (cm)	Cu:NbTi	Avg. Fil. Diam. <D> (μm)	$\frac{D_{max}}{D_{min}}$	ΔD (μm)	Deformation length [<D>)	n
Sample A	0.51 x 1.02	187	1.8	4.77	27	1.33	8.9	4	18
Sample B	0.56 x 0.71	180	1.3	1.8	33	1.20	6.5	8	35
Sample C	1.00 diam.	114	2.5	5.5	37	1.06	2.2	6	53

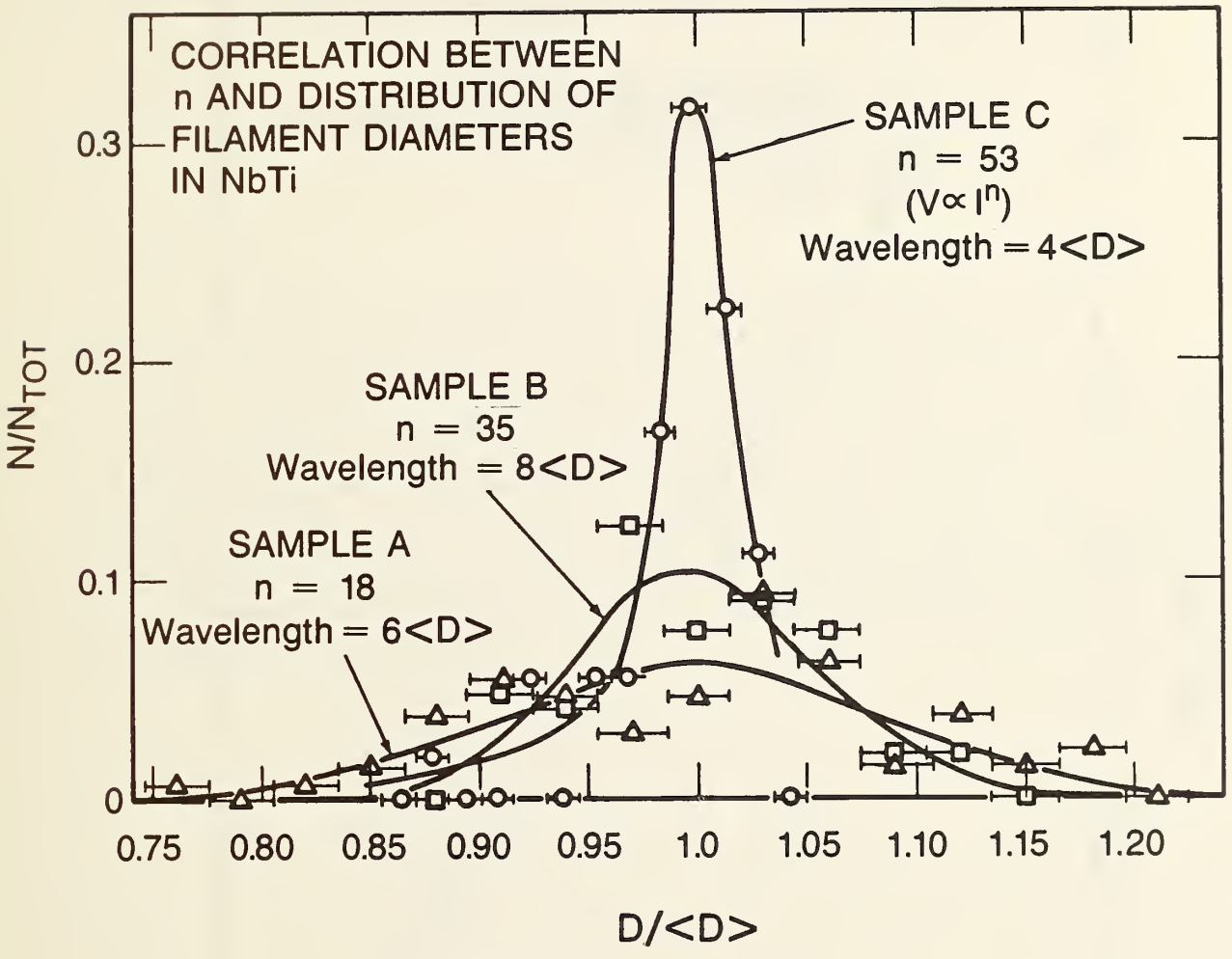

Figure 6. Distribution of filament diameters in samples A, B, and C. Horizontal bars indicate the sampling interval for each histogram. Irregularities in the cross sectional area of each filament mainly determine n, rather than variations in the average filament diameter from filament to filament. In these samples, the average filament diameter varied with radial position in the composite. The radial effect was eliminated from the plotted distribution by determining the variation in diameter of each filament relative to the average diameter of other filaments occupying the same relative radial position in the composite.

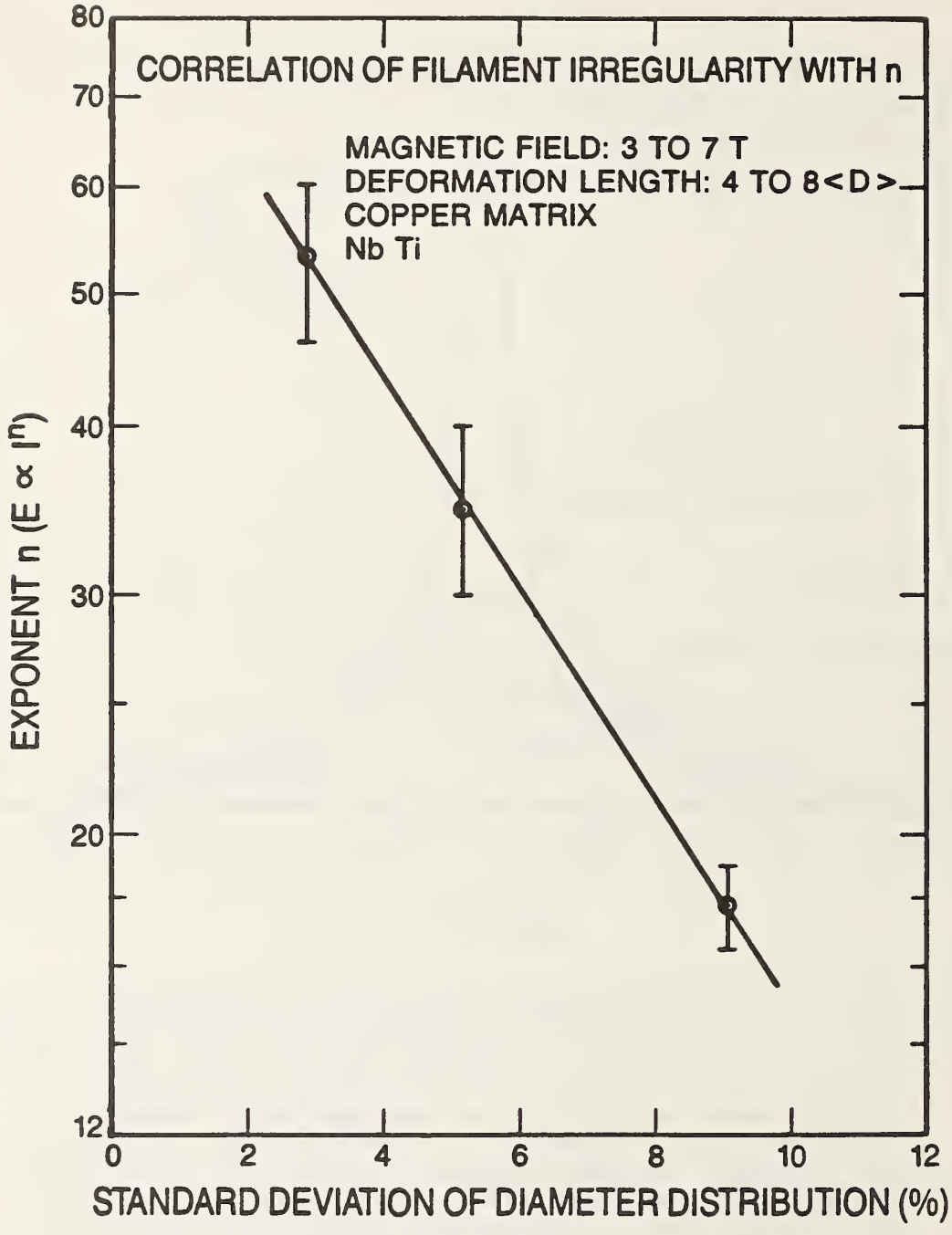

Figure 7. Appróximate relationship between n and the standard deviation of the filament-diameter distribution for several multifilamentary NbTi superconductors.

V APPENDIX - ELECTRON TUNNELING INTO SUPERCONDUCTING FILAMENTS: DEPTH PROFILING THE ENERGY GAP OF NbTi FILAMENTS FROM MAGNET WIRES

by John Moreland, J. W. Ekin, and L. F. Goodrich

(To be published in Adv. in Cryo. Eng. 32, 1986.)

SUMMARY

A new technique for measuring the depth profile of the energy gap in filaments extracted from commercial NbTi conductors was developed. A demonstration of the technique was made on NbTi conductor typical of that manufactured in the early 1970's. It was found that the energy gap in a filament surface layer several micrometers thick was reduced to approximately one third of that in the filament interior. The energy-gap degradation was found to correlate with the presence of very small amounts of copper (3 wt%) in the filament surface layer. Further study of the energy gap in NbTi alloy with controlled amounts of copper contamination are needed to clarify the observation and its implications for the manufacture of fine filament NbTi superconductors.

ELECTRON TUNNELING INTO SUPERCONDUCTING FILAMENTS: DEPTH PROFILING THE ENERGY GAP OF NbTi FILAMENTS FROM MAGNET WIRES.*

John Moreland, J. W. Ekin, and L. F. Goodrich

Electromagnetic Technology Division
National Bureau of Standards
Boulder, Colorado

ABSTRACT

Squeezable electron tunneling (SET) junctions consisting of superconducting NbTi filaments (extracted from magnet wires) and sputtered Nb thin-film counter electrodes were used to determine the energy gap at the surface of the filaments. The current versus voltage curves of junctions immersed in liquid helium at 4 K were measured for a series of filaments taken from the same wire. Each filament had been etched to remove a surface layer of varying thickness so that the energy gap could be determined as a function of depth into the surface of an "average" filament. It was found that some manufacturing processes yield filaments having surface layers with reduced energy gaps of 0.4 meV compared to measured interior bulk values ranging from 1.2 to 1.3 meV.

INTRODUCTION

Multifilamentary-NbTi superconductors are used extensively in the construction of large-scale magnets. This is primarily due to the relative ease of manufacture and the strain insensitivity of the superconducting properties of NbTi filaments. With the proper heat treatment, NbTi alloys precipitate Ti rich inclusions within the material. It is generally accepted that these precipitates act as vortex pinning sites that give rise to the large critical currents observed in NbTi filaments. A good understanding of the alloy metallurgy is therefore vital to developing better high-current superconductors.[1,2] Perhaps equally important are the effects of various steps in manufacturing processes on microscopic intrinsic superconducting parameters. In particular, the magnitude of the superconducting energy gap, Δ, directly affects T_c,[3] H_{c2},[4] and along with alloy metallurgy, determines J_c.[5]

An electron tunneling experiment is an excellent probe of the fundamental parameters that govern the superconducting state, providing a direct measurement of the energy gap. This is because the conductance of a superconducting tunnel junction as a function of applied bias (often

referred to as a tunneling spectrum) is directly related to the density of states of thermal excitations in a superconductor as a function of energy. Recently it has been shown that electron tunneling experiments can be performed using ultrastable electromechanical transducers to space two electrodes about 1 nanometer apart, stable to within a few picometers.[6] In this way the oxide barrier previously required for tunneling measurements has been eliminated, providing an alternative method for obtaining tunneling spectra. The concept of mechanically adjustable barriers is attractive because it is relatively straightforward to make a tunneling contact to any conductor including bulk materials. In particular, we have shown in an earlier paper that a superconducting squeezable-electron tunneling (SET) junction can be constructed between a filament and a thin-film counter electrode in liquid helium at 4 K.[7]

Tunneling electrons probe a superconducting surface to a depth of about one BCS coherence length. It should therefore be possible to delineate the superconducting properties of a material as a function of depth to within submicron distances. Presented here, for example, are results obtained when the SET-junction technique mentioned above was applied to NbTi superconductors. Individual filaments were removed from multifilamentary NbTi superconductors by chemically etching away the surrounding copper stabilizer. The surfaces of many such filaments were then etched different amounts to obtain the "depth profile" of the energy gap of the "average" filament within a given conductor.

APPARATUS

The experimental apparatus used to "squeeze" filament SET junctions is described in earlier papers.[6,7] Essentially the filaments were positioned above a 0.2 μm-thick Nb counter electrode sputtered onto a flexible Si substrate with 1 μm-thick evaporated SiO spacers. An electromagnetic squeezer adjusted the bow in the substrate and thus the distance between the filament and the Nb counter electrode. In this way tunneling barriers a few nanometers thick could be obtained with stability sufficient for tunneling spectroscopy of energy gaps. The squeezer was mounted on a probe designed for rapid measurements at 4 K in a liquid-helium storage Dewar. It was possible to cool, perform a tunneling measurement, and warm within a 30-minute time span.

The I-V curve was monitored over the range from -5 to +5 mV as the junction was mechanically adjusted in liquid helium to obtain a tunneling characteristic. Four-terminal contact was made to the junction. Superconducting counter electrodes were used because they gave rise to distinct structure in the I-V curves that provided a quality check for the tunneling barrier even if the sample electrodes were normal. Also, it was easier to detect small energy gaps for the sample electrodes as shifts in the I-V characteristic using a superconducting counter electrode, compared to shifts of a broad zero-bias inflection in a relatively featureless curve using a normal counter electrode.

Curves of dynamic conductance (dI/dV) versus voltage were measured with a tunneling spectrometer that utilized a feedback circuit to keep a constant modulating voltage (250 μV, 100 Hz) across the junction. This signal was superposed onto the slowly swept dc voltage (± 5 mV, sweep rate = 100 μV/s). The conductance was proportional to the first-harmonic signal measured with a lock-in amplifier. For two superconducting electrodes the sum of the energy gaps, Δ_1 and Δ_2, can be estimated from the location of the peaks in the conductance spectrum of the junction using the formula

$$e\bar{V} = 2\Delta_1 + 2\Delta_2. \qquad (1)$$

$\bar{V}$ is the voltage separating the peaks in the conductance spectrum that occur near the current inflections in the I-V curve and e is the electron charge. This procedure is used instead of measuring $\Delta_1 + \Delta_2$ from an apparent zero bias so that small preamplifier offsets need not be considered in the energy gap measurements.

The energy gap of the Nb thin-film counter electrodes was determined by measuring the tunneling energy gap of a SET junction with two identical thin films and found to be 1.4 meV. One of these calibrated counter electrodes was then transferred to the filament-tunneling apparatus. The contribution from the counter electrode ($2\Delta_{film}$ = 2.8 meV) was subtracted from the sum of the energy gaps to obtain the energy gap of the filaments ($2\Delta_{filament}$). Typically the data lead to measurements precise to within ± 0.1 meV.

Tunneling contacts were nondestructive in that the magnitude of the tunneling energy gap was independent of the resistance for a given junction setting as long as the junction was not shorted. Since a nondestructive tunneling contact was made between the filament and the film and care was taken to avoid moisture condensation between runs, the counter-electrode films could be reused many times.

FILAMENT SAMPLES

Individual NbTi filaments from 20 to 30 μm in diameter (filaments with diameters less than 20 μm were difficult to mount in the apparatus) were removed from multifilamentary-NbTi superconductors by etching away the surrounding Cu matrix in a 50/50 solution of nitric acid and water at room temperature. Subsequent etches to remove varying-thickness surface layers from a single filament were performed in freshly prepared solutions consisting of 4 parts hydrofluoric acid, 36 parts nitric acid, and 60 parts water at room temperature. The etch rate was determined for several filaments etched different amounts using a scanning electron microscope (SEM) to compare adjacent etched and unetched portions of the filaments. The etch rate was constant over the measured etching range from 0 to 10 μm. It had a value of 50 ± 5 nm/s, which was about the same as the etch rate for pure Nb.

Typical SEM micrographs of etched NbTi filaments are shown in figure 1. The filaments in figures 1a, 1b, and 1c were taken from a wire that was made using a conventional manufacturing process that included high temperature extrusion followed by cold working and a final Cu annealing step. This wire was made in the early 1970's and may not be representative of conductors fabricated using current technology. The small nodules a few microns in size on the surface of the unetched filament (Fig. 1a) have been attributed to a Cu-NbTi surface layer that forms during the hot extrusion and subsequently breaks up into debris during cold working.[2,8] After a short etch (20 s) these nodules are removed from the filament surface (Fig. 1b). Further etching serves not only to reduce the filament diameter but also polishes the filament surface, removing striations acquired during the wire-drawing process (Fig. 1c).

Other filaments tested include those extracted from "cold-process" wire previously developed for experiments aimed at understanding mixture and alloy formation and their effect on NbTi superconductors.[8] This wire was not optimized for a high J_c. It was processed without any high-temperature extrusion, was drawn at low temperatures, and was given no heat treatments during processing. SEM micrographs of unetched filaments of this kind were devoid of Cu-NbTi nodules (fig. 1d).

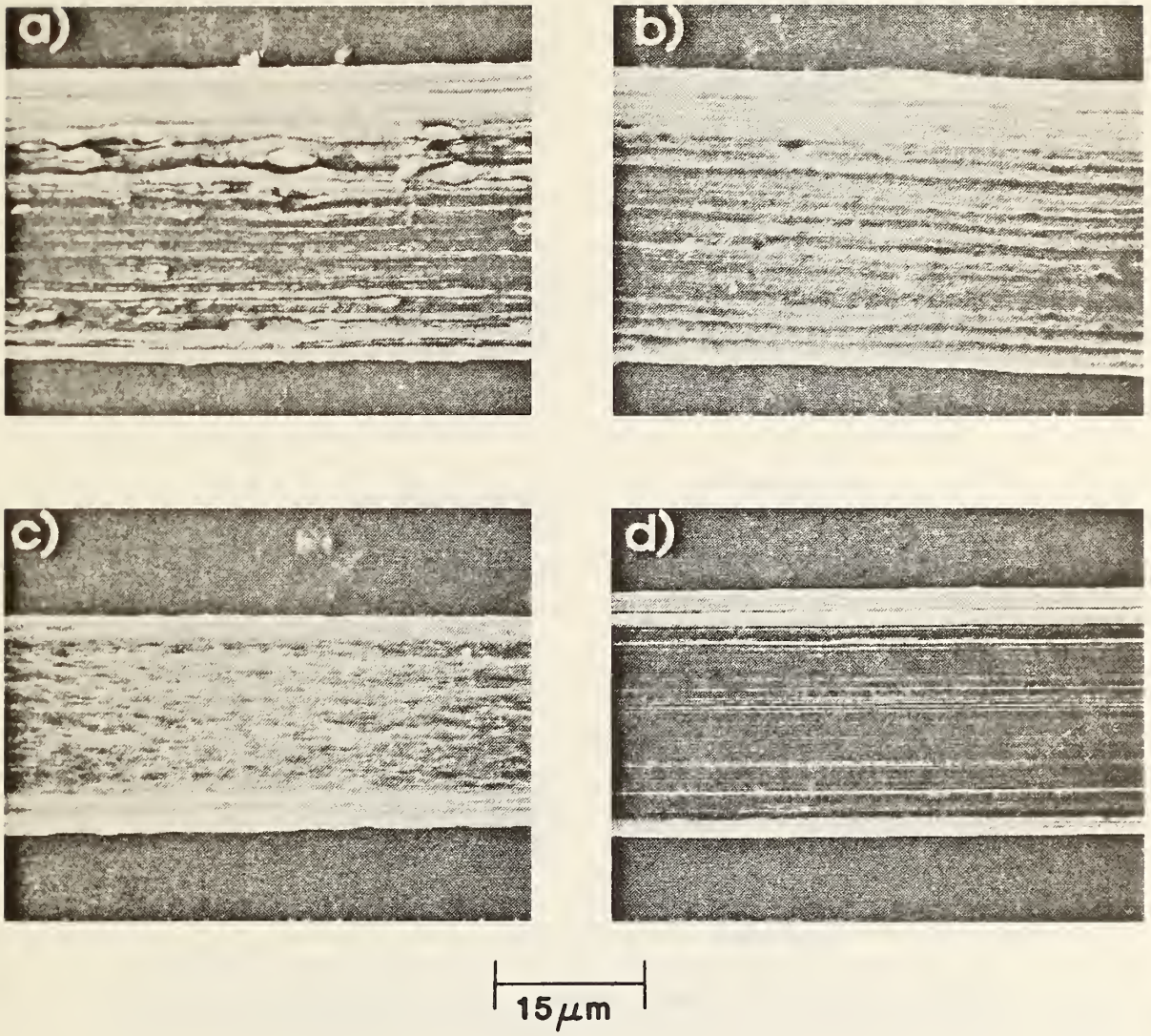

Fig. 1 Electron micrographs of various NbTi filaments.
a) Unetched conventionally processed filament with Cu-NbTi nodules.
b) Conventionally processed filament after 1 μm etch.
c) Conventionally processed filament after 6 μm etch.
d) Unetched "cold-process" developmental filament.

DEPTH-PROFILE RESULTS

Figure 2 shows the tunneling spectra (conductance versus voltage) of a series of NbTi-filament SET junctions with Nb thin-film counter electrodes immersed in liquid helium at 4 K. Each filament had been etched for a different time. The etching depths are based on the measured etch rate of 50 nm/s mentioned above. The peaks defining the gap edges in each of the curves in Fig. 2 are used to determine the energy gap of the filaments.

Data derived from curves like those shown in figure 2 are presented in profile format in figure 3. Here we plot the filament energy gaps derived from the conductance curves as a function of estimated etching depth for two different kinds of wire. The dashed lines are included to aid the viewer's eye. Each data point represents a local measurement of the energy gap. The variability of the data taken at a given etch depth may be an indication of the variability between filaments. It may also, however, be due to changes that occur along the surface of a filament.

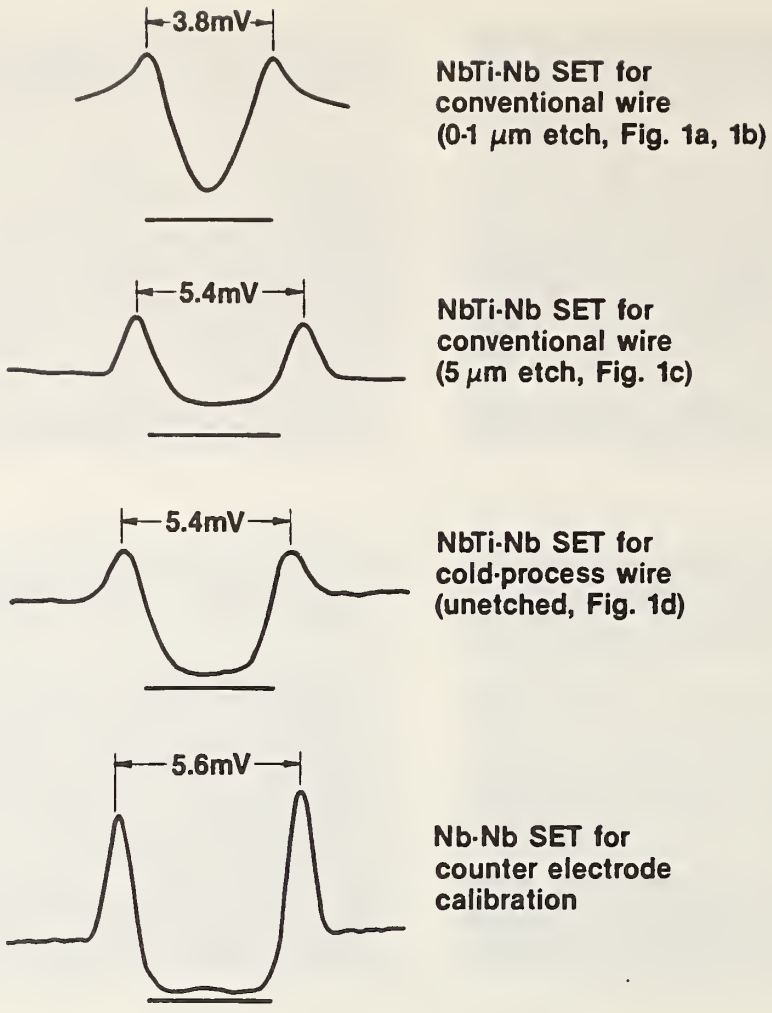

Fig. 2 Tunneling spectra (conductance versus voltage) of various NbTi-filament/Nb-film SET junctions in liquid helium at 4 K.

The results for wire manufactured using the conventional method are shown in figure 3a. In general, eV increases with increasing etching times from a value as low as 3.2 meV to about 5.4 meV, corresponding to filament energy gaps that range from 0.4 meV at the filament surface to 1.3 meV in the filament interior (see equation 1). There appears to be a 3- to 4-μm thick layer at the surface of an unetched filament with a substantially reduced energy gap compared to the highest interior bulk value.

Figure 3b, on the other hand, shows the profile of a wire that had undergone cold drawing without any heat treatments or extrusion, thus avoiding the formation of Cu-NbTi mixtures. The energy gap is relatively constant as a function of depth having a value of about 1.2 to 1.3 meV even at the unetched-filament surface.

Also included in figure 3 are the corresponding energy-dispersive X-ray microanalysis results that show the weight percent Cu as a function of filament etch depth for both types of wire. A discernable difference (dashed line) from the instrumental background signal (solid line) is apparent in Fig. 3c for conventionally processed filaments that had undergone an etch of 4 μm or less. [The dashed line is shown for reference only; the signal to noise ratio is about 2, which does not permit the detailed shape of the Cu profile to be determined.] In contrast, very little Cu above background levels could be detected in the cold-process filaments as shown in figure 3d.

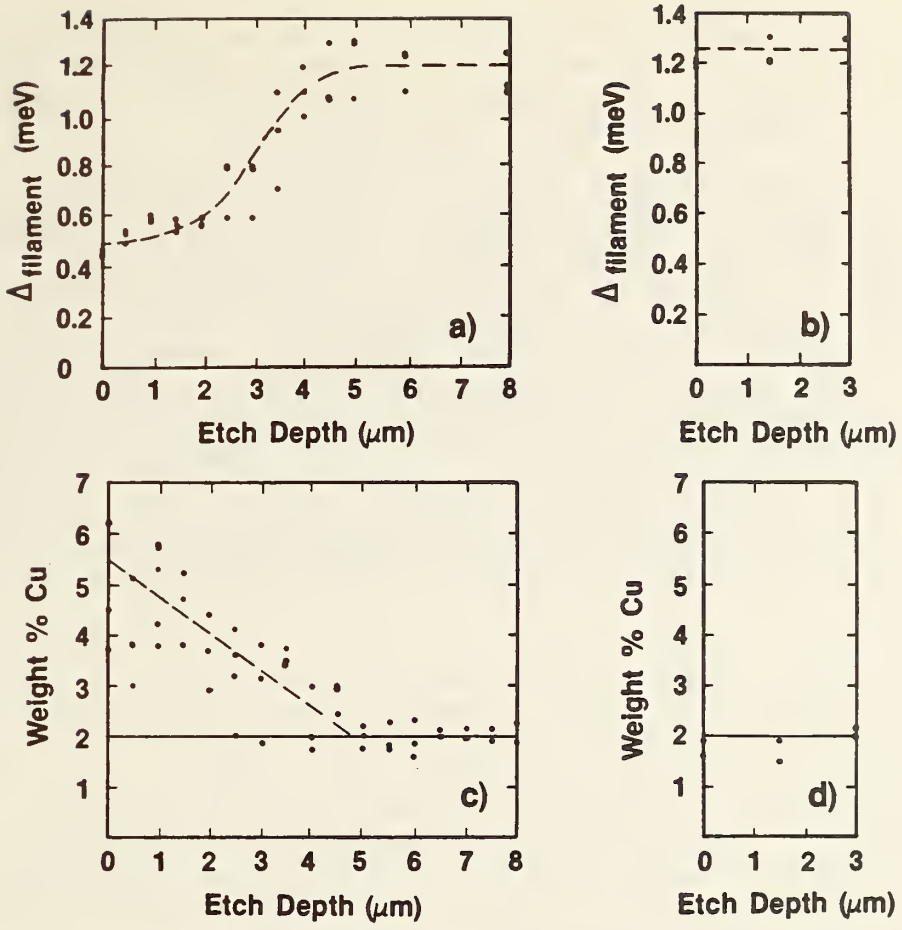

Fig. 3 Depth profiling results for NbTi filaments from magnet wires: $\Delta_{filament}$ as a function of estimated etch depth for an average filament extracted from (a) conventionally processed and (b) developmental cold-processed wires (T = 4 K). Weight percent Cu determined by X-ray microanalysis as a function of estimated etch depth for an average filament extracted from (c) conventionally processed and (d) developmental cold-processed wires. The instrumental Cu background signal was approximately 2%.

The experiment was repeated with both the conventionally-processed and the cold-processed wires etched simultaneously in the same hydrofluoric-nitric-water bath. The same X-ray microanalytic Cu concentration results were obtained as before. This indicates that the difference between the two types of samples was not simply an artifact of surface contamination introduced when the filaments were etched in different baths of the same solution.

Energy-dispersive X-ray microanalysis is a semi-quantitative technique that yields average weight percent of an element over the area illuminated by the SEM beam (in our case about 10 μm^2). Further, the penetration depth of the 25 keV beam used in these studies is about 1 μm. In comparison, tunneling electrons probe only to a depth of about one BCS coherence length (about 10 nm for NbTi) over a very small SET junction area (probably less than 1 μm^2).

CONCLUSION

We have demonstrated a new depth profiling technique for studying the energy gap in practical superconductors. The results show that a NbTi conductor made by conventional manufacturing methods of the early 1970's

had filament surface layers with energy gaps as low as 0.4 meV at 4 K. The low gap region extended 3-5 μm into a 30 μm filament. NbTi wires that had not undergone high-temperature processing showed very little energy-gap reduction at the filament surface (Δ 1.3 meV at 4 K).

The tunneling data combined with the X-ray microanalysis on the conventionally-processed filaments suggests that there is a correlation between the presence of Cu and the observed low energy gaps near the filament surface. The amount of Cu detected is very small, less than about 3 wt % above the instrumentational background signal. It is unlikely that it is simply an artifact of SEM electron penetration through a thin (< 1 μm) high-Cu content intermetallic layer. This is because these small Cu concentrations are measured at etching times well beyond the point where a thin intermetallic layer should have been chemically removed. We conclude, therefore, that a low-concentration Cu diffusion layer is introduced during processing. It is unclear at this time if this layer is particular to the early 1970's conductor which we tested, or whether it occurs more generally. Further studies will be needed to accurately clarify its nature and origin.

Other phenomena, including surface mechanical damage or oxygen contamination introduced during conventional processing may also be important. In addition, the etching process used to remove filament surface layers may affect the outcome of a given profile measurement. The fact that $\Delta_{filament}$ does not decrease for the cold-process wire and increases in the conventionalprocess wire with further etching shows that at least the etch is not detrimental to the energy gap. It may, however, change the Cu concentration from the original diffusion profile. A more conclusive and more quantitative study might therefore include tunneling into bulk alloys purposely contaminated with known amounts of Cu.

Depending on the current flowing through and the magnetic field within the filaments of a magnet wire, the effective area of each filament may be substantially reduced by the presence of a surface layer with a degraded energy gap. Considering that many applications require superconducting magnets to be operated near their critical parameters, the observed energy-gap degradation could have significant effects (especially at high fields near H_{c2}). It is therefore important to isolate the manufacturing steps that lead to the formation of a degraded-superconductor layer.

ACKNOWLEDGMENTS

Partial support was provided by the Department of Energy. Support was also provided to one of us (J.M.) as a National Research Council Postdoctoral Associate. Helpful discussions with R. Scanlan, A. West, D. Larbalestier, M. Suenaga, M. Garber, and P. Purtscher are gratefully acknowledged.

REFERENCES

1. D. C. Larbalestier and A. W. West, New perspectives on flux pinning in niobium-titanium composite superconductors, Acta Metall. 32:1871-1881 (1984).
2. M. Garber, M. Suenaga, W. B. Sampson and R. L. Sabatini, Effect of Cu_4Ti compound formation on the characteristics of NbTi accelerator magnet wire, to be published in IEEE Trans. on Nuclear Science, 1985; D. C. Larbalestier, Li Chengren, W. Starch, and P. J. Lee, "Limitation of critical current density by intermetallic formation in fine filament Nb-Ti superconductors," to be published in IEEE Trans. on Nuclear Science, 1985; see also papers CZ-2 and CZ-3 of this conference proceedings and the references cited therein.

3. J. Bardeen, L. N. Cooper and J. R. Schrieffer, "Theory of Superconductivity", Phys. Rev. 108:1175-1204 (1957).
4. A. A. Abrikosov, On the magnetic properties of superconductors of the second type, Sov. Phys. JETP 5:1442-1452 (1957).
5. R. Hampshire, J. Sutton and M. T. Taylor, Effect of temperature on the critical current density of Nb-44 wt. percent Ti alloy, in: "British Cryogenics Council Conference on Low Temperatures and Electrical Power", Program preprint IIR, Royal Society, London, England (1969), pp. 69-76.
6. J. Moreland and P. K. Hansma, Electromagnetic squeezer for compressing squeezable electron tunneling junctions, Rev. Sci. Instrum. 55:399-403 (1984).
7. J. Moreland and J. W. Ekin, Electron tunneling into superconducting filaments using mechanically adjustable barriers, Appl. Phys. Lett. 47:175-177 (1985).
8. A. W. West, Rensselaer Polytechnic Institute, Troy, New York, private communication.

NBS-114A (REV. 2-8C)

U.S. DEPT. OF COMM. BIBLIOGRAPHIC DATA SHEET (See instructions)	1. PUBLICATION OR REPORT NO. NBSIR 86-3061	2. Performing Organ. Report No.	3. Publication Date December 1986

4. TITLE AND SUBTITLE

Electromechanical Properties of Superconductors for High-Energy Physics Applications

5. AUTHOR(S)

J. W. Ekin, L. F. Goodrich, J. Moreland, E. S. Pittman, and A. F. Clark

6. PERFORMING ORGANIZATION (If joint or other than NBS, see instructions)

NATIONAL BUREAU OF STANDARDS
DEPARTMENT OF COMMERCE
WASHINGTON, D.C. 20234

7. Contract/Grant No.

8. Type of Report & Period Covered

9. SPONSORING ORGANIZATION NAME AND COMPLETE ADDRESS (Street, City, State, ZIP)

Division of High-Energy Physics
U.S. Department of Energy
Washington, DC 20545

10. SUPPLEMENTARY NOTES

☐ Document describes a computer program; SF-185, FIPS Software Summary, is attached.

11. ABSTRACT (A 200-word or less factual summary of most significant information. If document includes a significant bibliography or literature survey, mention it here)

This report covers the first year of a 33-month project to establish a systematic base of experimental data on electromechanical effects in superconducting wire and cables for high-energy-physics magnet applications. The research is focused in four general research areas: electromechanical relationships in NbTi, studies of NbTi strands extracted from cables, sausaging effects in NbTi, and studies of the NbTi energy gap.

12. KEY WORDS (Six to twelve entries; alphabetical order; capitalize only proper names; and separate key words by semicolons)

cables; electromechanical properties; high-energy physics; magnets; NbTi; stress effect; superconductors

13. AVAILABILITY

☒ Unlimited

☐ For Official Distribution. Do Not Release to NTIS

☐ Order From Superintendent of Documents, U.S. Government Printing Office, Washington, D.C. 20402.

☒ Order From National Technical Information Service (NTIS), Springfield, VA. 22161

14. NO. OF PRINTED PAGES

112

15. Price

*U.S. GOVERNMENT PRINTING OFFICE: 1987-0-774-326/65078